Doctoral Dissertation
Doctoral Program in Metrology (XXXIV cycle)

Characterization of magnetic materials at extreme ranges of field, temperature, and permeability

By

Mariano Pentella
******

Supervisor(s):
Prof. Sabrina Grassini, Supervisor
Prof. Pasquale Arpaia, Co-Supervisor
Dr. Marco Buzio, Co-Supervisor

Doctoral Examination Committee:
Dr. Lucio Fiscarelli, Referee, European Organization for Nuclear Research (CERN)
Prof. Rosario Schiano Lo Moriello, Referee, University of Naples "Federico II"
Prof. Guido Perrone, Polytechnic University of Turin
Prof. Alessandro Re, University of Turin
Prof. Egidio De Benedetto, University of Naples "Federico II"

Politecnico di Torino
2022

Declaration

I hereby declare that, the contents and organization of this dissertation constitute my own original work and does not compromise in any way the rights of third parties, including those relating to the security of personal data.

<div align="right">

Mariano Pentella

2022

</div>

"Utopia lies at the horizon.
When I draw nearer by two steps, it retreats two steps.
If I proceed ten steps forward, it swiftly slips ten steps ahead.
No matter how far I go, I can never reach it.
What, then, is the purpose of utopia?
It is to cause us to advance." - Eduardo Galeano

Acknowledgements

Abstract

Materials shall display properties compatible with their target application. In particle accelerators, the trajectory of the particle beam is controlled using magnetic fields. These magnetic fields do not interact only with the beam but also with the surrounding elements of the machine. Some components generate the magnetic field, while others are used for different purposes and passively interact with it. In this context, the magnetic properties of materials are of great relevance, and requirements are specified. Verification of the magnetic properties relies on consolidated standards, which are not all-purpose, implying that complementary methods are necessary to cover all the requirements, and present different limitations.

In high-energy accelerators, such as the Large Hadron Collider at CERN, materials and components work in a harsh environment, under strong magnetic fields, and at a temperature of 1.9 K. In the context of the High Luminosity upgrade of the LHC, new superconducting magnets will be installed, including 11-T dipole magnets and the new quadrupoles to be installed at the sides of the intersection points. Simulations of these magnets showed that the iron yoke is heavily saturated when they are operated at their nominal field, reaching a magnetic flux density of about 3 T around the aperture, and with a significant impact of the yoke magnetic properties in the saturation region. The iron yoke material data at these fields are not available in the literature and therefore, they need to be measured. However, generating magnetic field values to obtain a flux density of 3 T in the iron is the main technical challenge. On the other hand, many other elements shall weakly interact with the field to not modify the field distribution and perturb the beam. The requirements are generally specified at room temperature. Various solutions are available in the literature, each one presenting limitations in terms of specimen size and range of test field. The twofold goal of this dissertation is to tackle these problems by developing two new measurement systems. The first is a superconducting permeameter to characterize soft ferromagnetic steels up to 2.8 T and at 4.2 K. As a case study, the

magnetic characterization of ARMCO® Pure Iron, the iron yoke material of the new LHC superconducting magnets, is presented. The second goal is to propose a measurement method for characterizing feebly magnetic materials with accuracy and resolution comparable with state-of-the-art solutions. The method fully exploits the flux-distortion detection method, works on bulky specimens arbitrarily shaped, and can therefore be used to test specimens or finished parts.

Keywords – Magnetic materials, particle accelerators, superconducting perme-ameter, static-sample magnetometer, vibrating sample magnetometer, stainless steels, radiation shielding, NMR, cryogenic measurement, flux-metric methods.

Contents

III A static-sample magnetometer for characterizing weak magnetic materials 109

List of Figures

List of Tables

List of Publications

Journal publications:

[P1]   Alessandro Parrella, Pasquale Arpaia, Marco Buzio, Annalisa Liccardo, Mariano Pentella, Rosario Principe, and Pedro M Ramos. "Magnetic properties of pure iron for the upgrade of the LHC superconducting dipole and quadrupole magnets". In: *IEEE Transactions on Magnetics* 55.2 (2018), pp. 1–4.

[P2]   Pasquale Arpaia, Marco Buzio, Susana Izquierdo Bermudez, Annalisa Liccardo, Alessandro Parrella, Mariano Pentella, Pedro M Ramos, and Edvard Stubberud. "A superconducting permeameter for characterizing soft magnetic materials at high fields". In: *IEEE Transactions on Instrumentation and Measurement* 69.7 (2019), pp. 4200–4209.

[P3]   Christian Grech, Marco Buzio, Mariano Pentella, and Nicholas Sammut. "Dynamic Ferromagnetic Hysteresis Modelling Using a Preisach-Recurrent Neural Network Model". In: *Materials* 13.11 (2020), p. 2561.

[P4]   Lorenzo Bortot, Matthias Mentink, Carlo Petrone, Jeroen Van Nugteren, Glyn Kirby, Mariano Pentella, Arjan Verweij, and Sebastian Schöps. "Numerical analysis of the screening current-induced magnetic field in the HTS insert dipole magnet Feather-M2. 1-2". In: *Superconductor Science and Technology* 33.12 (2020), p. 125008.

[P5]   Pasquale Arpaia, Marco Buzio, Alessandro Parrella, Mariano Pentella, and Pedro M Ramos. "A Static-Sample Magnetometer for Characterizing Weak Magnetic Materials". In: *IEEE Transactions on Instrumentation and Measurement* 70 (2020), pp. 1–9.

[P6]   Pasquale Arpaia, Philip Nicholas Burrows, Marco Buzio, Chetan Gohil, Mariano Pentella, and Daniel Schulte. "Magnetic characterization of Mumetal® for passive shielding of stray fields down to the nano-Tesla level". In: *Nuclear Instruments and Methods in Physics Research Section A: Accelerators, Spectrometers, Detectors and Associated Equipment* 988 (2021), p. 164904.

[P7]   Lorenzo Bortot, Matthias Mentink, Carlo Petrone, Jeroen van Nugteren, Guy Deferne, Torsten Koettig, Glyn Kirby, Mariano Pentella, Juan Carlos Perez, Francois-Olivier Pincot, Gijs de Rijk, Stephan Russenschuck, Arjan Verweij, and Sebastian Schöps. "High-temperature superconducting screens for magnetic field-error cancellation in accelerator magnets". In: *Superconductor Science and Technology* (2021).

[P8]   Pasquale Arpaia, Marco Buzio, Vincenzo Di Capua, Sabrina Grassini, Marco Parvis, and Mariano Pentella. "Drift-Free Integration in Inductive Magnetic Field Measurements Achieved by Kalman Filtering". In: *Sensors* 2.1 (2021), p. 182.

[P9]   Olaf Dunkel, Melvin Liebsch, Mariano Pentella, Carlo Petrone, and Pierre Alexandre Thonet. "Design, Manufacturing and Measurement of three Permanent Magnet Dipoles for FASER Experiment". In: *IEEE Transactions on Applied Superconductivity - Submitted* ().

Conference proceedings:

[P10]   Jaime R Anglada, Pasquale Arpaia, Marco Buzio, Annalisa Liccardo, Alessandro Parrella, Mariano Pentella, and Pedro M Ramos. "On the importance of magnetic material characterization for the design of particle accelerator magnets". In: *Journal of Physics: Conference Series*. Vol. 1065. 5. IOP Publishing. 2018, p. 052045.

[P11]   Jaime R Anglada, Pasquale Arpaia, Marco Buzio, Mariano Pentella, and Carlo Petrone. "Characterization of Magnetic Steels for the FCC-ee Magnet Prototypes". In: *2020 IEEE International Instrumentation and Measurement Technology Conference (I2MTC)*. IEEE. 2020, pp. 1–6.

[P12] Pasquale Arpaia, Marco Buzio, Ernesto De Matteis, Alessandro Parrella, and Mariano Pentella. "Magnetic properties of a nanocrystalline material for current derivative sensors of magnets protection systems". In: *XXIV IMEKO TC-4 International Symposium and XXII Internation Workshop on ADC/DAC Modeling and Testing (IMEKO TC-4)*. International Measurement Confederation. 2020, pp. 1–5.

List of Abbreviations

IEC	International Electrotechnical Commission
CERN	European Organization for Nuclear Research
MSC	Magnets, Superconductors, and Cryostats
LHC	Large Hadron Collider
HL-LHC	High Luminosity - Large Hadron Collider
LIU	LHC Injectors Upgrade
VSM	Vibrating Sample Magnetometer
RF	RadioFrequency
LEP	Large Electron-Positron Collider
ELENA	Extra-Low ENergy Antiproton Ring
FCC-e$^+$e$^-$	electron-positron - Future Circular Collider
FE	Finite Elements
PS	Proton Synchrotron
PSB	Proton Synchrotron Booster
REX-ISOLDE	Radioactive beam EXperiment - Isotope mass Separator On-Line facility
PETRA	Positron-Electron Tandem-Ring facility
CLIC	Compact LInear Collider
AISI	American Iron and Steel Institute
PM	Permanent Magnet
LINAC	LInear ACcelerator

n-Tof	neutron - Time of Flight
FASER	ForwArd Search ExpeRiment at the LHC
ASTM	American Society for Testing and Materials
SQUID	Superconducting QuantUm Interference Device
ARMCO	American Rolling Milling Company
KEK	National Laboratory for High Energy Physics in Japan
INFN	Instituto Nazionale di Fisica Nucleare
RRR	Residual Resistance Ratio
DAC	Digital-to-Analog Converter
DCCT	DC Transformer
ADC	Analog-to-Digital Converter
FFMM	Flexible Framework for Magnetic Measurements
ISO	International Organization for Standardization
GUM	Guide to the Expression of Uncertainty in Measurement
SSM	Static-Sample Magnetometer
ITER	International Thermonuclear Experimental Reactor
CAD	Computer-Aided Design
NMR	Nuclear Magnetic Resonance
AMR	Anisotropic Magneto-Resistance
GMR	Giant Magneto-Resistance
EDM	Electrical Discharge Machining
FIB	Focused Ion Beam
SEM	Scanning Electron Microscope
WHA	Pure tungsten Heavy Alloy
NSSC	Nippon Steel & Sumikin Stainless Steel Corporation
SPS	Super Proton Synchrotron
SNR	Signal-to-Noise Ratio
DQW	Double Quarter Wave

RFD   RF Dipole

MRI   Magnetic Resonance Imaging

Introduction

Materials are of particular importance in all engineering fields, and they must display properties compatible with their target application. This principle is also true for particle accelerators, complex machines made of various components, each playing a specific role. In particle accelerators, the beam is steered and kept on a nominal trajectory using magnetic fields. The presence of magnetic fields implies that each component interacts with them: some components are used to generate the magnetic field, while others are used for different purposes and passively interact with it. Verification of the magnetic properties is of paramount importance for design scopes and quality control during the production process of these components. Measurement of magnetic properties relies on consolidated standards, such as the International Electrotechnical Commission (IEC) 60404 series, and is performed on specimens having pre-defined shapes, dimensions, expected magnetic behaviors, and operating conditions. These test methods are not all-purpose, which means that complementary test methods are necessary to cover the spectrum of requirements and, in some cases, need to be adapted. Only a few laboratories are available on the market to perform these measurements with the drawback of having long lead times, high costs, and scarce capability to process special requests. For this reason, at European Organization for Nuclear Research (CERN), in the Magnets, Superconductors, and Cryostats (MSC) group, a measurement service for materials' characterization has been set up to process the increasing number of requests from the internal research community. The available equipment within this service consists of different test benches used to characterize the magnetic properties of material specimens having different shapes, dimensions, and different magnetic behaviors to be used in particle accelerator components. Moreover, the technical capability goes beyond the international standards' requirements, and non-standard measurements can also be performed. The work presented in this dissertation has been carried out in this

context for the past three years.

High-energy colliders are realized using superconducting magnet technology to steer highly energetic and intense particle beams. For instance, in the Large Hadron Collider (LHC) operated at CERN [1], the beam energy is 6.5 TeV, and the peak luminosity in the collision point, namely the number of collisions per unit surface and unit time, is 1×10^{34} cm^{-2}s^{-1}. Materials and components are operated in a harsh environment, in superfluid helium at 1.9 K, and under magnetic fields reaching up to 8.6 T in dipole magnets. For the High Luminosity upgrade of the LHC, the High Luminosity - Large Hadron Collider (HL-LHC) [2], the nominal integrated luminosity will be increased by a factor of ten times higher than the LHC design target. The increase of luminosity will require the installation of new, stronger superconducting dipole magnets with a nominal field increased up to 11.2 T, and quadrupole magnets, having a nominal gradient of 132.6 T/m in an aperture of 150 mm.

The magnetic properties of materials depend on the operating conditions, magnetic field, and temperature above all. Simulations of the new LHC magnets showed that the iron yoke is heavily saturated in these magnets, reaching a flux density of about 3 T in the iron region surrounding the aperture [3]. Moreover, as it will be presented in Part. II, the impact of the magnetic properties in the saturation region is more significant on the magnet transfer function, which means that the entire saturation region has to be accurately measured. Usually, measurements are performed using the flux-metric method up to 2 T magnetic flux density and at magnetic fields ranging between 20 and 50 kA/m because these values are of interest to optimize the design of magnets and electrical machines [4, 5]. However, since the field is generated using an excitation coil, generating fields in the order of hundreds of kA/m requires to increase the excitation current, and therefore the cross-section of coils and cables to carry a higher current, or the number of excitation turns, and therefore the coil resistance. The main constraints are the available power supply used to generate the excitation current in both cases and the heat dissipation due to Joule losses. The problem has been tackled in this dissertation by developing a new measurement system, the superconducting permeameter, designed and metrologically characterized to extend the operating range of the available hardware. As a case study, the system was validated by measuring American Rolling Milling Company (ARMCO)® Pure Iron, used for the iron yoke for the HL-LHC magnets.

The upgrade of the LHC does not consist only of new magnets but also of the upgrade of the injector chain, the LHC Injectors Upgrade (LIU) project [6], as well as the

installation of new components, such as new collimators [7], crab cavities [8], and collars. These elements are required ideally to not interact with the field or limit as much as possible the extent of this interaction to not modify the field distribution and perturb the beam [9]. The requirements are specified at room temperature, and the magnetic properties of these materials are verified using a portable instrument, which is not accurate enough and operated at only one field value. The state-of-the-art solution, the Vibrating Sample Magnetometer (VSM) [10], although having permeability accuracy lower than 10^{-5}, presents several limitations. The VSM is limited to specimens having a volume of a few mm^3, and such a small specimen size can introduce two systematics. The first one is that the measurement of a single specimen cannot be considered as representative of the material batch, and therefore multiple specimens need to be tested to compute an average value. The second one derives from the specimen cut from the main material batch, which can significantly impact the properties to be measured if the specimen preparation is not done properly (see Chap. 7). The problem has been tackled in this dissertation by developing a new measurement system, the static-sample magnetometer, using hardware commonly available in magnetic measurement laboratories and working on bulky specimens having whichever shape and dimensions.

The content of this dissertation is divided into three Parts.

Part. I: Background and state of the art, is dedicated to a brief introduction to the magnetic characterization of materials, the materials commonly used in particle accelerator applications, and the state-of-the-art solutions to perform magnetic characterization of materials. In particular:

- **Chapter 1: Magnetic materials and particle accelerators**, introduces what characterizing a material magnetically means, expands the motivations behind the necessity of materials' characterization in particle accelerator applications, and presents the most common materials used in particle accelerator applications.

- **Chapter 2: State of the art**, presents the state-of-the-art solutions used to characterize the magnetic properties of materials.

Part. II: Characterization of magnetic materials at extreme ranges of field and temperature, is dedicated to the characterization of soft ferromagnetic materials at

high field and cryogenic temperature, leading to the development of the superconducting permeameter. The work presented in this Part was carried out in the context of the production of ARMCO® Pure Iron, the material selected as the iron yoke for the new LHC superconducting magnets. In particular:

- **Chapter 3: Context and problem statement**, presents the context and the results of an extensive test campaign carried out for ARMCO®, tested in different conditions, and provides a deeper insight of the motivations leading to the superconducting permeameter development.

- **Chapter 4: Proposal**, illustrates the proposal, shows the design steps of the superconducting permeameter, and presents the metrological characterization of the system.

- **Chapter 5: Experimental results and discussion**, presents two case studies and the experimental results.

Part. III: A static-sample magnetometer for characterizing weak magnetic materials, is dedicated to the characterization of weakly magnetic materials, and the development of the static-sample magnetometer. In particular:

- **Chapter 6: Problem statement and proposal**, presents the problem statement, highlighting the limits of the existing test methods, and illustrates the measurement principle of the static-sample magnetometer, proposed to overcome these limits.

- **Chapter 7: Metrological characterization**, presents the metrological characterization of the static-sample magnetometer, and the description of the uncertainty sources.

- **Chapter 8: Experimental results**, presents three case studies where the characterization of materials having different shapes, dimensions, and expected magnetic properties provide an extensive assessment of the operating range and the limits of the test method.

Part I

Background and state of the art

Chapter 1

Magnetic materials and particle accelerators

In this Part of the dissertation, background elements of magnetic materials, and state-of-the-art methods for their characterization are presented. State-of-the-art characterization methods are presented in Chap. 2. This Chapter focuses on presenting magnetic materials, how they are classified, what are the main alloys and compounds used in particle accelerator applications, and why materials have different requirements in particle accelerators. Moreover, the purpose of magnetic characterization of materials is explained. Part of the content shown in this Chapter was also previously published in [P3, P6, P9, P10, P11].

1.1   Characterization of magnetic materials

Magnetically characterizing a material can have different meanings. As explained in [11], characterizing a material can have two different but not necessarily independent meanings:

- Measuring the intrinsic magnetic properties of a material, dependent on microscopic physical phenomena (*i.e.*, Curie's temperature, saturation point, anisotropy).

- Determination of the magnetic constitutive law, namely the magnetization curve or the hysteresis loop.

In this dissertation, the goal of the characterization is the second point. Hence, the problem can be seen as an identification problem, where a known magnetic field is applied and the material response has to be measured.

From an electromagnetic point of view, the need for a constitutive law arises from the necessity of having Maxwell's equations in closed form. Starting from Maxwell's equations in the matter, expressed in the local form

$$\nabla \times \mathbf{E} = -\frac{\partial \mathbf{B}}{\partial t}$$

$$\nabla \cdot \mathbf{D} = \rho$$

$$\nabla \times \mathbf{H} = \mathbf{J} + \frac{\partial \mathbf{D}}{\partial t}$$

$$\nabla \cdot \mathbf{B} = 0$$

with $\mathbf{E}$ electric field, $\mathbf{D}$ the electric displacement field, $\mathbf{H}$ the magnetic field, $\mathbf{B}$ the magnetic flux density or magnetic induction, ρ the free charge density, and $\mathbf{J}$ the free current density. This set of equations does not have a solution because other two vector equations are missing, describing the behavior of the matter with respect to the externally applied fields: the constitutive laws.

The constitutive laws originate from the so-called bound sources, originating at the atomic level in the matter. More in detail, when an electric field is applied, molecules form electric dipoles $\mathbf{p}$ that align in the direction of the field. At the macroscopic level, a bound charge is produced at the surface of the body, and this can be described by a field $\mathbf{P}$ called polarization, describing the dipole moments per unit volume. Therefore, $\mathbf{D}$ is defined as

$$\mathbf{D} = \varepsilon_0 \mathbf{E} + \mathbf{P} \tag{1.1}$$

where ε_0 is the vacuum electric permittivity.

Similarly, for the magnetic field, Ampère proposed that in the matter, the atoms form magnetic moments, originating from microscopic current loops linked to the angular momentum of the electrons. Another source is electron spins. These current loops determine bound current sources, generating a field $\mathbf{M}$, called magnetization and defined as the magnetic moments per unit volume. Therefore, $\mathbf{H}$ is defined as

$$\mathbf{H} = \frac{\mathbf{B}}{\mu_0} - \mathbf{M} \tag{1.2}$$

where μ_0 is the vacuum magnetic permeability.

Eq. 1.1 and Eq. 1.2 are called constitutive laws, and they describe the response of the bound sources to the externally applied fields. In the general case, $\mathbf{D} = \mathbf{D}(\mathbf{E})$ and $\mathbf{B} = \mathbf{B}(\mathbf{H})$. In the case of linear materials, the relations can be simplified by introducing the relative electric susceptibility χ_e, and the relative magnetic susceptibility χ_m, where

$$\mathbf{P} = \varepsilon_0 \chi_e \mathbf{E}$$
$$\mathbf{M} = \chi_m \mathbf{H}.$$

From the two susceptibilities, one can express the relationship between $\mathbf{E}$ and $\mathbf{D}$, and between $\mathbf{H}$ and $\mathbf{B}$ by defining the electric relative permittivity ε_r and μ_r

$$\varepsilon_r = 1 + \chi_e$$
$$\mu_r = 1 + \chi_m.$$

For magnetic materials characterization, the goal is identifying the magnetic constitutive law

$$\mathbf{B} = \mathbf{B}(\mathbf{H}). \tag{1.3}$$

In many cases, due to symmetry assumptions and assuming that the material is isotropic, the expression is expressed in the scalar form, $B = B(H)$.

1.2 Classification of materials

Materials behaves differently under the application of an external magnetic field. In the following, the main classification of materials is recalled, without providing an

extensive description of the physical phenomena, which goes beyond the purposes of this dissertation.

In Sec. 1.1 it was shown that matter can be seen in a first approximation as formed by magnetic moments originating from the motion of electrons along circular trajectories, forming microscopic current loops. The density of these current loops, how they interact, and how they are organized can change from material to material, leading to different macroscopic behaviors.

1.2.1   Diamagnetic materials

As reported by Blundell in [12], "all materials show some degree of diamagnetism", up to a certain extent because other mechanisms of interaction play a role. Diamagnetism can be described from a classic point of view as induced magnetism on atoms or molecules having no unpaired orbital electron spins, arising from applying a magnetic field inducing magnetic moments generated by small circular current loops. In the absence of a field, there are no magnetic moments. When a field is applied, as a result of Lenz's law, atomic currents are induced, determining magnetic moments that align in the opposite direction of the external field to oppose it. As a result, the susceptibility $\chi_m < 0$, the permeability $\mu_r < 1$, and both are constant with the field and the temperature. The induced magnetic moment m in a single microscopic current loop is:

$$m = -\frac{e^2}{4m_e}r^2\mu_0 H \tag{1.4}$$

with e the charge of the electron, m_e the mass of the electron, r the loop radius. Diamagnetic materials, except superconductors, are generally considered non-magnetic because their interaction with an external field is very weak. Hence, they have low susceptibility values. Tab. 1.1 provides susceptibility values for some diamagnetic materials. It is worth highlighting the much lower susceptibility of gases, owing to their mass densities.

Table 1.1 Susceptibility values of some diamagnetic elements [13, 14].

Material	χ_m
Water	-9×10^{-6}
Copper	-10×10^{-6}
Mercury	-29×10^{-6}
Lead	-18×10^{-6}
Graphite	-18×10^{-6}
Silver	-26×10^{-6}
Helium	-1×10^{-9}
Nitrogen	-5×10^{-9}

1.2.2   Paramagnetic materials

Paramagnetism is a quantum effect arising from pre-existing magnetic moments caused by the presence of unpaired electron orbital spins [12]. In the absence of a magnetic field, these magnetic moments are randomly oriented because their interaction is weak, thus giving a zero net magnetic moment. When an external field is applied, these moments align in the direction of the field, prevailing on the always present diamagnetic contribution. Paramagnetism can be described using a classical approach, leading to Langevin's model for paramagnetism. In this model, the magnetization is described by the relation

$$M = <m> N \left(\coth s - \frac{1}{s} \right) \tag{1.5}$$

where the expression between brackets is called Langevin's function, $\mathscr{L}(s)$, with $<m>$ the average magnetic moment and N the number of moments per unit volume. Moreover,

$$s = \frac{m \mu_0 H}{k_B T}, \tag{1.6}$$

where k_B is the Boltzmann's constant and T is the temperature. A plot of Eq. 1.5 is shown in Fig. 1.1.

In truth, Eq. 1.5 represents only a classical approximation and does not consider that due to quantization, magnetic moments can point only in pre-defined directions. A quantum theory exists, and the general equation is
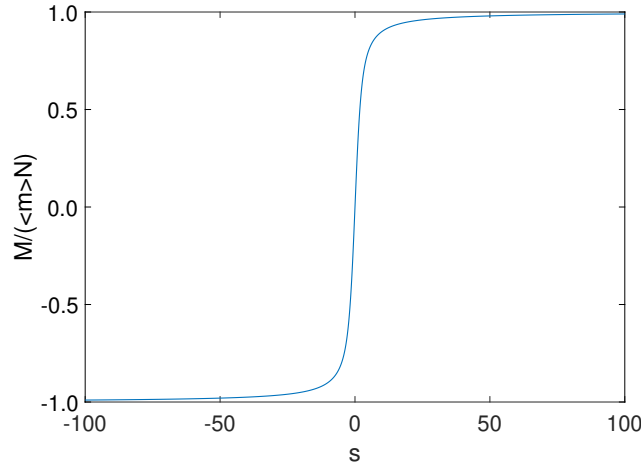
Fig. 1.1 A plot of the Langevin's function, described in Eq.1.5.

$$M = <m> N B_J(q) \qquad (1.7)$$

where $B_J(x)$ is the Brillouin function, having the following expression

$$B_J(q) = \frac{2J+1}{2J} \coth\left(\frac{2J+1}{2J}\right) q - \frac{1}{2J} \coth\frac{q}{2J}, \qquad (1.8)$$

with J angular momentum quantum number. The parameter q has the following expression:

$$q = \frac{g_J \mu_B J \mu_0 H}{k_B T}, \qquad (1.9)$$

where g_J the g-factor and μ_B Bohr's magneton. Eq. 1.5 is the approximation of Eq. 1.7 when $J = \infty$. Further details can be found in [12, 15]. Tab. 1.2 provides susceptibility values for some diamagnetic materials. It is worth to mention the much lower susceptibility of gases, owing to their low mass densities.

1.2.3 Ferromagnetic materials

In Sec. 1.2.2 it was seen that paramagnetic materials exhibit no magnetization in the absence of an applied field because the exchange interactions between magnetic moments are weak, and the pre-existing magnetic moments are randomly aligned,

Table 1.2 Susceptibility values of some paramagnetic elements [13, 14].

Material	χ_m
Aluminum	2.2×10^{-5}
Tungsten	6.8×10^{-5}
Lithium	1.4×10^{-5}
Oxygen (at 1 atm, 290 K)	3.7×10^{-7}

thus providing a zero net magnetization.

Ferromagnetic materials also have pre-existing magnetic moments, similarly to paramagnetic materials. However, the interaction of these magnetic moments is much stronger because the exchange interactions between orbital spins determine long-range order. These determine the presence of macroscopic regions, called Weiss's domains, where neighboring moments are aligned in parallel, separated by the domain's walls, also called Bloch's walls [12, 16, 17]. As a result, these materials present a spontaneous magnetization. Moreover, spin/orbit interactions determine a magnetocrystalline anisotropy, favoring spin orientation along a preferential direction, also called easy magnetization axis [17]. The exchange interaction is weakened by the thermal agitation and disappears above a critical temperature, called Curie's temperature.

Such organization of the magnetic moments determines a constitutive relation exhibiting hysteresis. An example is shown in Fig. 1.2.

In a demagnetized state, the magnetizations of the domains are randomly organized and provide zero net contribution to the field. In the demagnetized state, $H = 0$ and $B = 0$. When a magnetic field is applied, domains start to re-arrange, and their walls move. As explained by Bertotti in [17], domains already oriented in the direction of the field expand and shrink the surrounding domains. This domain walls' motion is reversible at low field, and then it becomes irreversible when the field amplitude is increased. By further increasing the field, all the domains will be oriented in the direction of the field, and the total magnetization will be constant. The material, in this condition, is defined as saturated. When the field is reversed, domains start to rotate in the direction of the field, and domain walls move.

However, the magnetization does not follow the same path because the process is irreversible and causes energy dissipation. It is worth mentioning that when the applied field is removed, $B \neq 0$ and equals B_r, called the *remanent field* or *remanence*, and an extra energy contribution has to be spent by applying an opposing field to
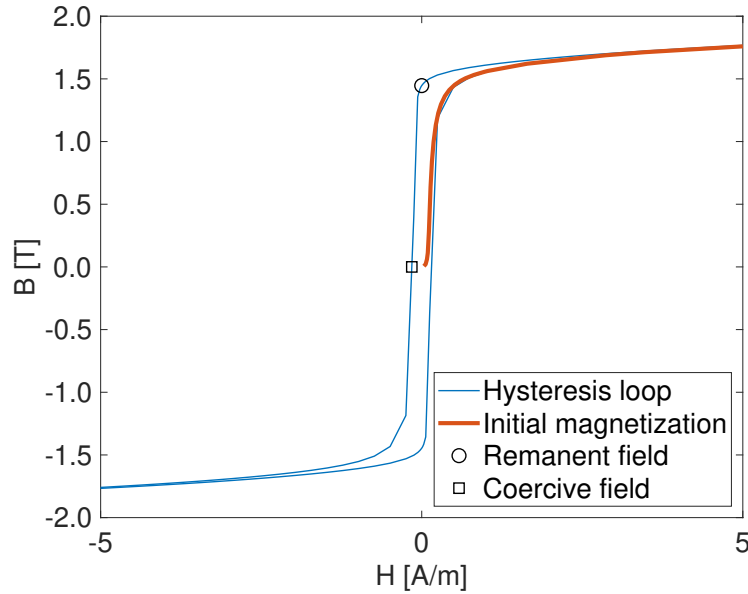
Fig. 1.2 Example of a hysteresis loop (blue). In orange, the initial magnetization curve. The two circles are the remanent field (black) and the coercive field (black).

cancel out the remanence. This field value is called *coercive field* or *coercivity*, H_c. The ascending branch from the demagnetized state is called the initial magnetization curve. Bertotti provides other meanings for the hysteresis loop in [17]. The behavior of the domains can be interpreted as a memory-dependent system since the material behavior depends on past-history magnetizations. Another interpretation is to describe the hysteresis as a lag between input field *H* and material response *B*.

Another quantity of interest for the characterization is the relative permeability, where for ferromagnetic elements, it is to be intended as a secant permeability

$$\mu_r = \frac{B}{\mu_0 H}. \tag{1.10}$$

Finally, the demagnetized state can be obtained thermally by bringing the material above its Curie's point and back, or magnetically, by applying a cyclic magnetic field from the saturation region and gradually decreasing the amplitude.

Analytical expressions can be found in the literature to describe the initial magnetization curve. In this dissertation, the equation proposed by Wlodarski in [18] was used to fit experimental data. Wlodarski describes the magnetization curve as the superposition of two magnetization processes, one reversible and the other one irreversible, reaching the following expression:

$$M(H) = M_a \mathscr{L}\left(\frac{H}{a}\right) + M_b \tanh\left(\frac{|H|}{b}\right)\mathscr{L}\left(\frac{H}{b}\right), \qquad (1.11)$$

where $M_a + M_b = M_s$, the saturation magnetization, and a and b are two parameters that describe how the material approaches saturation. $\mathscr{L}$ is the Langevin function, already presented in Eq. 1.5.

For the hysteresis loop, the situation in terms of mathematical modeling is more complex. Most models describe a rate-independent hysteresis. The most used model in the literature is the Jiles-Atherton model [19, 20], which was modified to take also into account rate-dependent phenomena [21, 22]. Another popular model is the Preisach model of hysteresis, also used for other kinds of hysteresis phenomena, and based on switching operators where suitable weighting functions combine their outputs [17], also modified to describe rate-dependent hysteresis [23, 24]. The recent trend in state of the art is the use of neural networks, alone or combined with Preisach operators, to describe ferromagnetic hysteresis [25, 26, 27]. An example of fit using experimental data using a recurrent neural network can be seen in Fig. 1.3.
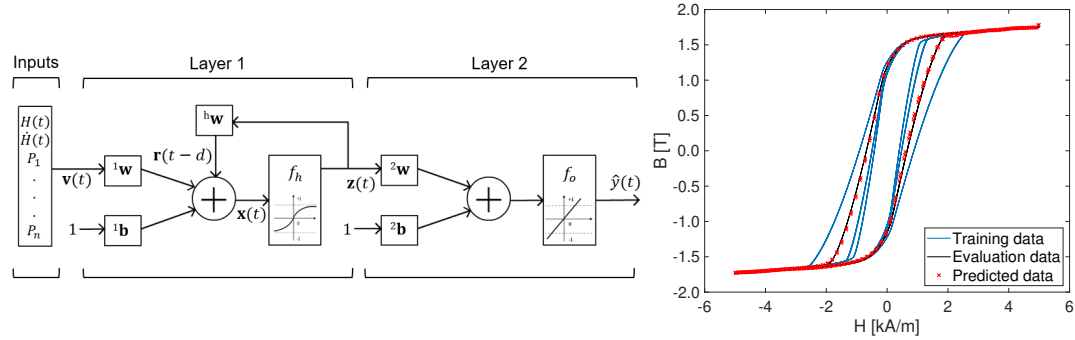
Fig. 1.3 (Left) Architecture of a Preisach-Recurrent Neural Network used to model dynamic ferromagnetic hysteresis; (Right) Comparison between training data set, evaluation data set and prediction. Normalized RMS error 0.58 %.

Ferromagnetic materials can be classified with respect to the coercive field value, which can be seen as an indicator of the easiness of magnetizing and demagnetizing the material. The coercive field determines the material's destination of use. Ferromagnetic materials can be classified as *soft ferromagnetic materials* (low H_c) and *hard ferromagnetic materials* (high H_c) [17]. As a rule of thumb, soft ferromagnetic materials have coercivity comparable with Earth's field, while hard ferromagnetic materials have coercivity much higher than Earth's field.

Soft ferromagnetic materials present peak relative permeabilities greater than 1000. Therefore, they behave as flux multipliers, meaning that a small-amplitude field can determine a much higher material response. This property makes them suitable for a wide variety of applications, such as magnet yoke laminations and magnetic shields. On the other hand, hard ferromagnetic materials, being difficult to be magnetized and demagnetized, are also called permanent magnets, and they are used as static field sources [16, 28]. Fig. 1.4 summarizes ferromagnetic materials in terms of coercive field values correlated with the peak permeability. The correlation between peak permeability and coercive field values is worth noticing because the magnetization process mechanisms are the same (domain walls motion). Different mechanisms impact the coercive field value, from magnetocrystalline anisotropy to the presence of pinning sites, impeding domain wall motion, and grain size. In particular, the grain size was found to contribute to the coercive field value through the following empirical relation [29]

$$\Delta H_c = 4 \times 10^{-2} \phi, \tag{1.12}$$

where ϕ is the number of grains per mm^2. Pinning sites, on the other hand, consist of the presence of randomly distributed non-magnetic inclusions and residual stresses. When the domain wall overcomes the energy barrier of a pinning site during its motion, a jump in the magnetization can be observed, and several jumps can be observed at a macroscopic level when the magnetization is in the coercive field region (Barkhausen's jumps).

1.2.4 Ferrimagnetic and anti-ferromagnetic materials

Ferrimagnetic and anti-ferromagnetic materials are another category of materials where long-range exchange interactions are present, as in ferromagnetic materials. Both categories of materials present magnetic domains, where the separation regions are called Neél's walls. However, the exchange interaction among magnetic moments is such that each moment is aligned in anti-parallel to the neighboring one. In ferrimagnetic materials, the amplitude "parallel" and "anti-parallel" moments are not the same and determine a spontaneous magnetization without an applied field. Both materials present a critical temperature, called Neél's temperature, above which the material becomes paramagnetic. Further information can be found in [12] and [28].
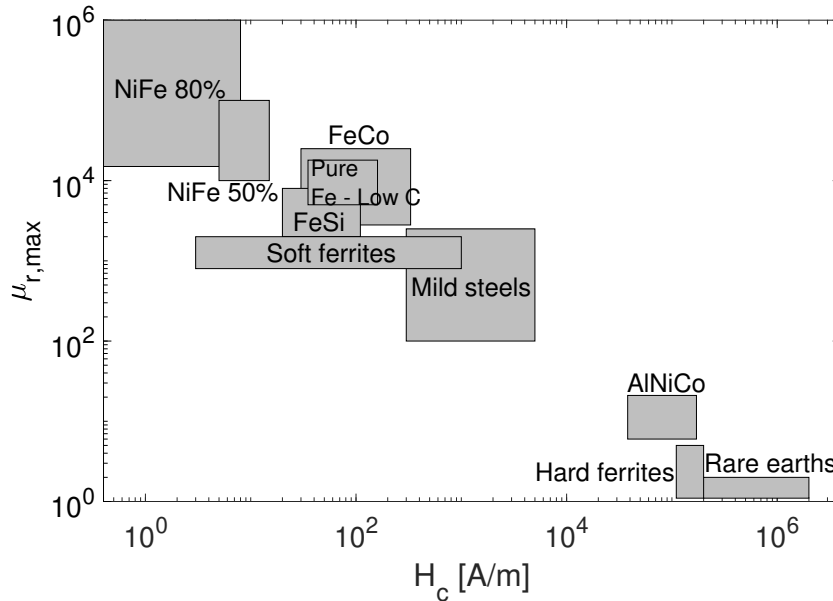
Fig. 1.4 Classification of ferromagnetic materials in terms of coercive field as a function of the peak permeability. Adapted from [16].

1.3 Motivation of magnetic field requirements for materials

As previously mentioned in the Introduction, materials shall have properties compatible with their target applications. In this dissertation, the main focus is particle accelerator applications. In this Section, the need for materials to respect requirements for magnetic fields is explained.

Particle accelerators consist of complex machines made of different components, with the aim of accelerating particle beams, and making them collide against a fixed target, or another beam traveling in the opposite direction (colliders). Whether the particle accelerator is linear or circular, in colliders the aim is to accelerate two particle beams, each one split in bunches and traveling in the opposite direction to make them collide at intersection points, where experiments are built to study the collisions. When two bunches collide, the collision energy is converted into other particles. Historically, the interest has always been to increase the number of collisions and their energy to study rare events. The number of collisions is expressed in terms of luminosity, the number of collisions per unit time, and unit cross-section. Another parameter of interest is the integrated luminosity, the integral

of the luminosity with respect to time.

The most powerful machine ever built so far is the LHC, a 27-km double-ring hadron machine where proton beams are accelerated up to 6.5 Tev [1, 16]. The machine is also periodically used to accelerate lead ions and make them collide at an energy of about 5 Tev for each colliding pair of nucleons.

Particles are driven in accelerators or experiments, using electric and magnetic fields, according to Lorentz's force

$$\mathbf{F} = q(\mathbf{E} + \mathbf{v} \times \mathbf{B}) \tag{1.13}$$

where q is the particle charge, and $\mathbf{v}$ its velocity. The term $q\mathbf{E}$ determines an acceleration of the particle bunches and increases their energy, while the other term $q\mathbf{v} \times \mathbf{B}$ only modifies their trajectory without increasing the energy because $\mathbf{F} \perp \mathbf{v}$ and therefore, the work of the magnetic field is zero. The acceleration is realized employing RadioFrequency (RF) cavities, while the particles' trajectory is modified through magnets.

Without providing an in-depth description of beam dynamics, which would go beyond the scope of this dissertation, magnets have to keep the particle beam on a nominal trajectory. Moreover, beam size needs to be kept under control to maximize the probability of collisions. Since the particle bunches diverge in the transverse plane of the machine [30], the control of the beam size is achieved using the beam optics [31], a complex of elements including magnets and collimators. The main magnets of interest for a synchrotron are:

- Dipole magnets, generating a uniform field in their aperture and used to steer the beam (bending action), thus controlling the motion in the longitudinal direction

- Quadrupole magnets, generating a field proportional to the distance from the magnet center, used to reduce the beam size (focusing action). The quadrupoles are arranged in a so-called FODO cell, where a quadrupole is alternated with another identical quadrupole rotated by 90 °C to provide, respectively, a focusing action in the vertical and horizontal direction of the orbit's transverse plane.

Fig. 1.5 shows a schematic representation of a synchrotron.
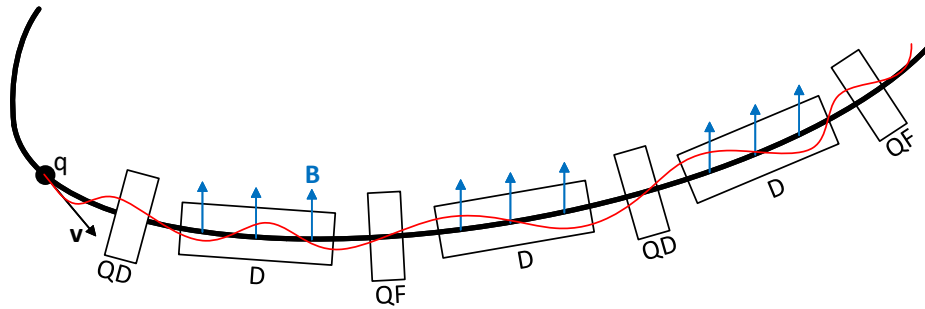
Fig. 1.5 Schematic representation of a circular accelerator. (D) are the dipole magnets, (QF) and (QD), the focusing and de-focusing quadrupoles respectively.

Generating homogeneous magnetic fields is crucial for beam stability [32], and therefore, magnets have to be designed to produce magnetic fields with high field quality. The field quality is expressed by expanding the transverse field in Fourier's series and considering the harmonic coefficients, namely the multipoles [16]. Given the main field component, controlling the field quality means verifying that the higher-order harmonics are kept small within tolerance values assessed with beam stability simulations. The field quality depends on many factors, such as assembly errors, yoke saturation, coil positioning, or pole geometry. For the LHC main bending magnets, the harmonics higher than the third order were required to be in the sub-unit of 10^{-4} range [16]. The field quality is verified during the magnet production process using different measurement methods, such as the wire techniques [33] or the rotating coil magnetometers [34, 35, 36].

Material requirements are specified for the magnets and all the other components installed in the machine that can interact with the magnetic fields. Magnets can be seen as static electrical machines, such as transformers. In most cases, their concept can be reduced to a simplified representation, consisting of three essential elements: an excitation coil, the electrical conductor that carries the excitation current necessary to generate the field, electrical insulation, and a yoke. Depending on the magnet technology, the conductor can either be a conventional conductor, such as copper (normal-conducting magnets), or a superconductor (superconducting and superferric magnets), such as NbTi or Nb_3Sn. For conductors and insulation, generally, there is no need to verify their magnetic properties. Exceptions exist for superconductors, where analysis of their operating limits [37] and the impact of the superconductor magnetization due to persistent currents [16, 38, 39] has to be investigated. As an alternative to coils, permanent magnet blocks arranged in a suitable configuration

can be used [40]. An example is the Halbach array [41], where permanent magnet blocks having magnetization pointing in pre-defined directions are arranged along a circumference. The magnet is then manufactured by assembling multiple circular layers along its length, with the aperture lying on the inner side of the magnet blocks. The yoke is an important element in a magnet for particle accelerators because it provides mechanical rigidity to the magnet assembly and a return path to the flux lines. The yoke is made of soft ferromagnetic material with high peak permeability and a high saturation point, such as low-carbon steels or FeSi alloys, and it is generally laminated to limit eddy currents and improve the dynamic performance. In some cases, where the field to be generated is in the order of tens of mT, alternative solutions can be used to reduce the costs. For the Large Electron-Positron Collider (LEP) magnets, the yoke was diluted with cement mortar, and the steel occupied only the 27 % of volume [42]. For the Extra-Low ENergy Antiproton Ring (ELENA) machine, prototypes having yoke diluted with stainless steel were initially considered [43]. For the electron-positron - Future Circular Collider (FCC-e$^+$e$^-$) magnet prototypes, low-cost structural steel was considered [44]. The spread of the magnetic properties in a magnet series production needs to be limited during the production because magnets are generally powered in series, and magnet-to-magnet reproducibility shall be guaranteed to obtain reproducible magnet behavior [45].

In normal-conducting magnets and superferric magnets, the iron yoke contributes up to 80 % to the total field in the magnet gap due to the flux-multiplier characteristic of soft alloys (iron-dominated magnets), and the magnetic field is defined by the iron pole shape. In superconducting magnets, the layout is different, and the iron yoke surrounds the excitation coil to provide a closure path to the field lines. In these magnets, the yoke contributes only up to 20-30 % to the total field (coil-dominated magnets), and the field quality is mainly dominated by the coil layout. As a result, the impact of the iron yoke is more significant in normal-conducting magnets, while the coil imperfections (assembly errors, persistent currents) have much more impact in superconducting magnets. Fig. 1.6 shows two types of magnets.

The yoke material needs to be magnetically characterized to obtain data for design scopes and accurately simulate the magnet. Moreover, the characterization is also used for quality control during the steel production process because the material properties can significantly change within the same batch. An example of how different yoke materials influence a magnet behavior is shown in Fig. 1.7, where the impact on three different magnetization curves on the gradient of a Q200 normal-
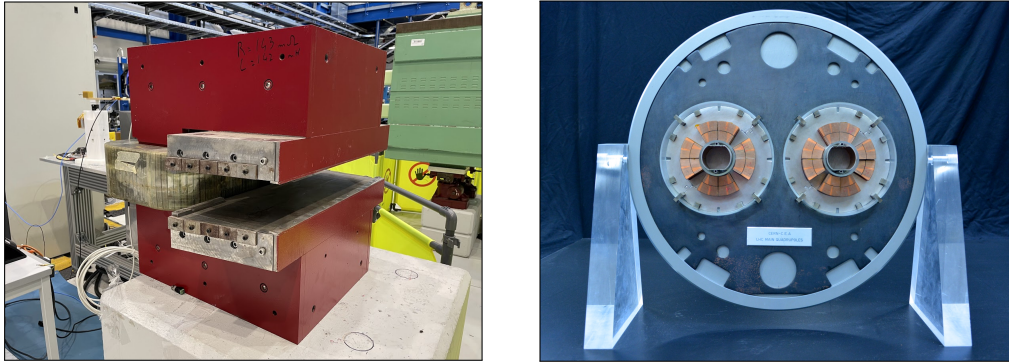
Fig. 1.6 (Left) Example of a C-shaped normal-conducting dipole; (right) slice of an LHC superconducting quadrupole (© 2017-2022 CERN).

conducting quadrupole magnet for the CERN East Area [46] was simulated. The curve included in the Finite Elements (FE) software used for simulations, OPERA 3D [47], being incomplete, determines a significant deviation with respect to the other two magnetization curves.
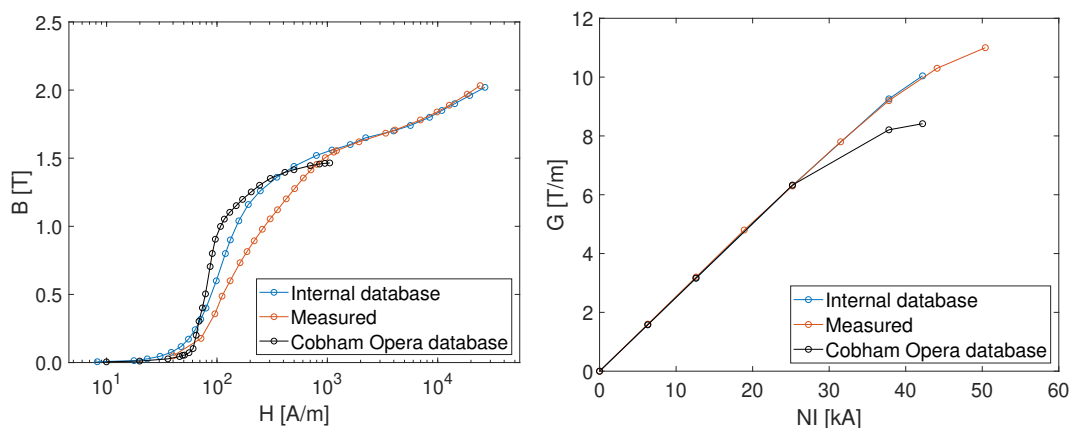
Fig. 1.7 (Left) Initial magnetization curves used to simulate to Q200 quadrupole magnet for the CERN East Area; (right) field gradient values as a function of the total excitation current *NI*, calculated using the magnetization curves on the left.

Other materials are installed in components that do not actively contribute to the field generation but are necessary for the machine operation, such as vacuum chambers where the beam circulates, collars to keep superconducting coils in position and prevent undesired movements, radiation shields, or other support elements. These materials shall be ideally non-magnetic and display the lowest possible magnetic permeability to avoid interactions with the magnetic field and perturb the particle

beam [9]. Ideally, these materials should have a permeability of 1. In practice, a few thousandths of magnetic susceptibility are allowed [48]. Some other materials are used for magnetic shielding, where it is necessary to prevent magnetic fields from reaching sensitive elements of a component. These materials shall have the highest possible magnetic permeability to behave as flux shunts for the external field [49, 50].

In conclusion, the variety of materials used in particle accelerator applications is broad and diverse, and accurate measurements of their magnetic properties are relevant.

1.4   Magnetic materials for particle accelerator applications

1.4.1   Pure iron and low-carbon steels

High-purity iron and low-carbon steels are widely used as yoke materials, owing to their high relative permeability values and saturation point.

High-purity iron is an alloy where the impurities do not exceed a few hundred ppm in concentration [51]. Their saturation magnetization $\mu_0 M_s$ is about 2.15 T. The saturation point is uniform between different pure iron grades, due to the high chemical purity [52], but a wide variety of coercive field values, peak permeabilities, and remanent fields can be observed, depending on the purity and crystallographic properties. Moreover, even though they do not present problems of aging, they are susceptible to cold working, which degrades the magnetic properties and presents poor mechanical properties [53].

When the concentration of impurities exceeds a few hundred ppm, the material is classified as a low-carbon steel. Low-carbon steels are a broader category of materials, where the saturation points and magnetization curves have a wider spread due to the higher impurity content, carbon above all. Moreover, they are sensitive to aging due to cementite precipitations (iron-carbon compound) determining the formation of pinning sites [51, 53]; this might be an issue for magnet long-term stability. Moreover, the wider spread of magnetic properties makes them non-suitable for large series production of magnets if careful control of the magnetic properties during the production process is not carried out. One way to avoid this effect is

shuffling the laminations prior to the magnet assembly [45]. The magnetic properties of low-carbon steels and pure irons can be boosted by annealing the alloy [51]. The annealing consists of a thermal treatment that brings the material at temperatures around 900 ° for a time of 1 h or more, and then slowly cooling it. Low-temperature annealing is stress-relieving because it reduces the coercive field by allowing a better diffusion of the pinning sites [54, 55, 56, 57]. High-temperature annealing, on the other hand, determines grain growth and, therefore, increases the remanent field and further boosts the magnetic properties [58]. As a result, the hysteresis loop becomes more squared, in simplified terms.

The main drawback of pure irons and low-carbon steels is the high electrical conductivity combined with the high permeability values, making these materials non-suitable for AC applications and, more generally, for fast pulsed magnets, where silicon-iron alloys are preferred.

Fig. 1.8 shows a selection of magnetization curves for pure irons and low-carbon steels used in different accelerators and experiments. References for the LHC magnets, the Proton Synchrotron (PS) magnets, and the Radioactive beam EXperiment - Isotope mass Separator On-Line facility (REX-ISOLDE) and Positron-Electron Tandem-Ring facility (PETRA) IV can be found in [16, 29, 59, 60, 61].
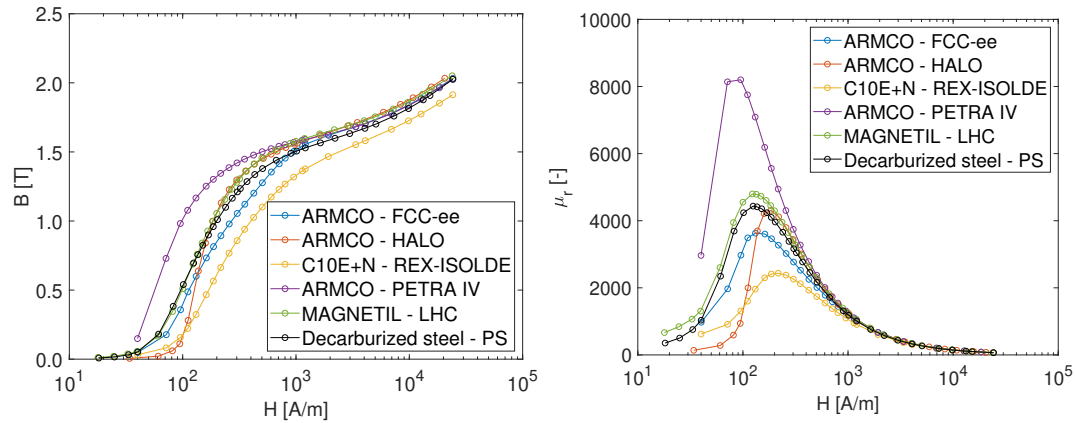
Fig. 1.8 (Left) Initial magnetization curves, and (right) relative permeability values for a selection of pure irons and low-carbon steels used in particle accelerator applications.

1.4.2 Iron-silicon alloys

Iron-silicon alloys also called electrical steels, are one of the most used categories of soft ferromagnetic material, especially in electrical transformers and motors, used at frequencies of 50-60 Hz [53]. In particle accelerator magnets, they are used in fast pulsed-field magnets, such as the Proton Synchrotron Booster (PSB) [62], or kicker magnets installed on beam transfer lines [63].

Iron-silicon alloys are steels where a certain percentage of silicon content, up to a 6 %, is added to decrease the electrical conductivity and boost the dynamic performance; this inevitably sacrifices the saturation magnetization $\mu_0 M_s$, which decreases to 1.3 T when the silicon content is 6 % [64]. Hence, a trade-off between dynamic performance and maximum achievable field level has to be found. On the other hand, the coercive field decreases, and the peak permeability increases, depending on the grain size. Fig. 1.9 shows the magnetization curves and the corresponding permeability values for some silicon steels used in particle accelerator applications. References can be found in [62, 65, 66].
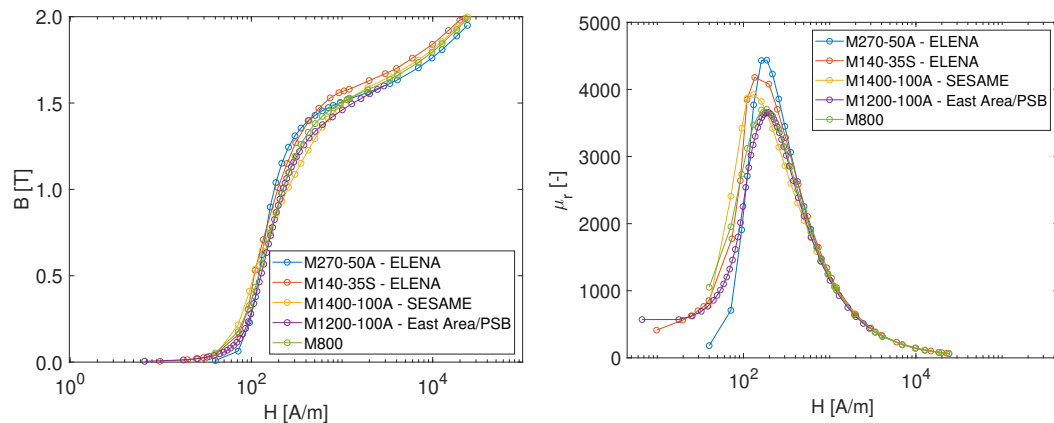
Fig. 1.9 (Left) Initial magnetization curves, and (right) relative permeability values for a selection of iron-silicon alloys used in particle accelerator applications.

Iron-silicon alloys can be classified into non-oriented and grain-oriented steels. Non-oriented steels are isotropic. Grain-oriented steels, on the other hand, are anisotropic and are characterized by the so-called Goss's texture [51], where grain growth along the rolling direction and the lamination surface is privileged; this determines a further boost of the magnetic properties when the field is applied along with the orientation of the grains, with coercive fields that can decrease to 4 A/m and

peak permeability boosted to 50000 [64]. In comparison with non-oriented silicon steels, H_c values are ten times lower and $\mu_{r,max}$ one order of magnitude higher.

1.4.3   Iron-nickel alloys

Iron-nickel alloys are a vast family of magnetic materials, having a large spread of magnetization curves, mainly depending on the nickel content.
Iron-nickel alloys nickel content of about 80 % and with proper annealing process [64], present extremely high peak permeabilities, in the order of hundreds of thousands and low coercive field values, below 1 A/m. They are typically used in magnetic shielding applications through two shielding mechanisms [67]:

- Flux-shunting, where the external field is channeled in the shield, having much higher permeability than the region to be shielded and preventing it from reaching the area to shield

- Eddy-current cancellation, where induced currents in the material by time-varying field produce a field that points in the opposite direction of the source to shield

This class of materials is highly sensitive to cold work, which can degrade the peak permeability up to one order of magnitude. These properties can be restored by performing high-temperature annealing. For the best performance, annealing should be performed in hydrogen at 1120 °C [51]. Fig. 1.10 shows two materials used for magnetic shielding applications. The first one is Mu-metal®, one of the most used NiFe alloys, used as a proposal to shield drift sections of the Compact LInear Collider (CLIC) beamline from stray fields [68]. The second one is an alloy called CRYOPHY, used to magnetically shield crab cavities, employed for beam deflection [69] in the HL-LHC, with the aim of increasing the luminosity. The material was developed for optimized properties at cryogenic temperature.

1.4.4   Stainless steels

Stainless steels are another widely used category of materials, especially in all those applications where good mechanical properties and low permeabilities are required,
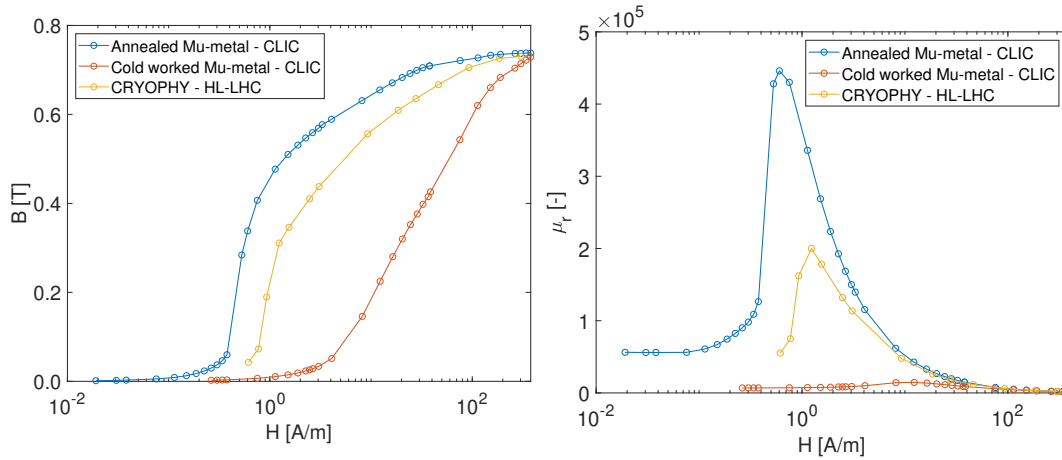
Fig. 1.10 (Left) Initial magnetization curves, and (right) relative permeability values for
annealed and cold worked Mu-metal®, and CRYOPHY [69].

such as vacuum applications [70]. Stainless steels are defined as iron alloys where
the chromium content is higher than 11 % [71]. Without providing too much detail of
metallurgic processes, stainless steels are divided into three different main families:
ferritic, martensitic, and austenitic stainless steels. Ferritic and martensitic stainless
steels present iron in the ferritic phase, α-phase, and δ-phase, where the crystal
has a body-centered cubic structure (bcc). Ferritic stainless steels have a chromium
content between 14.5 % and 27 %, while martensitic stainless steels generally have
chromium content not higher than 14 %. Martensitic steels have, in addition, a
few percent of carbon content to increase hardening [71]. These two families are
ferromagnetic at room temperature.

The addition of other elements such as nickel, molybdenum, nitrogen, and other
alloying elements can suppress the formation of martensitic and ferritic phase and
expand the domain of the iron γ-phase, called austenitic phase, not ferromagnetic
and having face-centered cubic structure (fcc), which is enclosed in a loop between
912 °C and 1394 °C, and up to 14 % chromium content. Further details about the
iron-chromium phase diagram can be found in [71, 72].

Austenitic stainless steels are of particular interest for particle accelerator applica-
tions, where the permeability needs to be kept low. For elements such as vacuum
components or collars, the requirement for the LHC and the HL-LHC is $\mu_r < 1.005$
at $H =$80 kA/m [48]. This requirement results from the fact that when only the
austenitic phase is present, the magnetic permeability $\mu_r < 1.005$. Depending on

their chemical composition, there are different austenitic stainless steels. One of the most used families for vacuum applications is the American Iron and Steel Institute (AISI) 300 series [73], and more in detail, the grades 304L, 316L, and 316LN [71]. 304L is general-purpose and has susceptibility between 0.003 and 0.005. However, this steel grade can undergo a martensitic transformation when cooled to cryogenic temperature or when cold worked, with the susceptibility increasing even of one order of magnitude. Therefore, if magnetic susceptibility is a concern for the application, particular attention shall be paid to the magnetic properties [71]. 316L contains molybdenum, which improves the stability with respect to martensitic transformation. Therefore, a narrower spread of magnetic susceptibility values is expected. 316LN contains nitrogen in addition, which further stabilizes the steel versus martensitic transformations and allows ductility conservation to cryogenic temperature [74]. The main problem is that these steel grades are antiferromagnetic when cooled down below 50 K, representing their Neél's temperature [51] and susceptibility values higher than the typical required permeability of 1.005 can be measured at 4.2 K [48]. For this reason, a high-manganese stainless steel, P506, was selected and used for the LHC beam screen since the susceptibility at 4.2 K is below 0.003 [70]. Fig. 1.11 shows an example of magnetic properties for AISI 310S, stainless steel used as a magnetic sheet for the LHC MQ protection sheets [75].
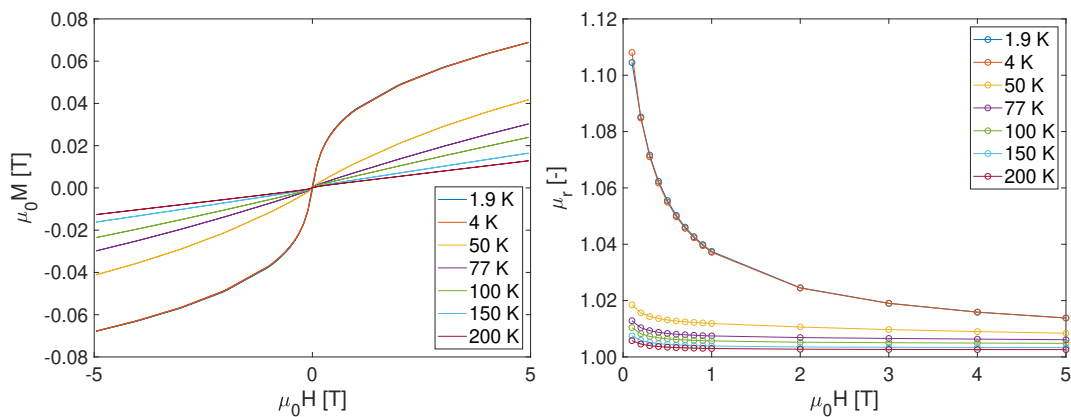
Fig. 1.11 (Left) Hysteresis loops, and (right) relative permeability values for a specimen of AISI 310S, measured at different test temperatures.

1.4.5 Permanent magnets

Permanent magnets, as previously seen in Sec. 1.2.3, present high coercive field values. This feature results in materials that are hard to demagnetize, and therefore their spontaneous magnetization can be seen as permanent. Permanent magnetization means that they can be used as a stable field source, which is often the case of electrical motors [76]. In particle accelerators, magnets can be realized using permanent magnet technology with several advantages, and multiple projects have already implemented it [40]. Their use allows a compact design of the magnets and does not require excitation coils. As a result, no power converters, and the equipment necessary to power the coils, are necessary, thus achieving low costs and efficiency. On the other hand, their use is limited to situations where the beam energy is constant, and no high fields are required (0.5-0.6 T). Another reason is that the facility where the accelerator or the experiment is installed needs to be at a stable temperature. Rare earth SmCo magnets are typically used to build magnets, owing to their energy density values, coercivity, and temperature coefficient (-0.0035 %/K). As reported by Thonet in [40], they are preferred over NdFeB magnets because of the higher resistance to ionizing radiations. Example of implementations are the LInear ACcelerator (LINAC) magnets [77], the neutron - Time of Flight (n-Tof) experiment [78] or the ForwArd Search ExpeRiment at the LHC (FASER) [79]. In order to have repeatable magnet behavior, the magnetic properties of the Permanent Magnet (PM) blocks should be as uniform as possible, typically within 1 %, and with deviations of the magnetization's orientation contained within 2 ° with respect to the nominal value. Fig. 1.12 shows an example of a series test campaign on 690 PM blocks of SmCo, aiming at verifying the uniformity of the properties of the blocks, having a standard deviation of 0.6 % of the average value and a maximum deviation of 2 %.
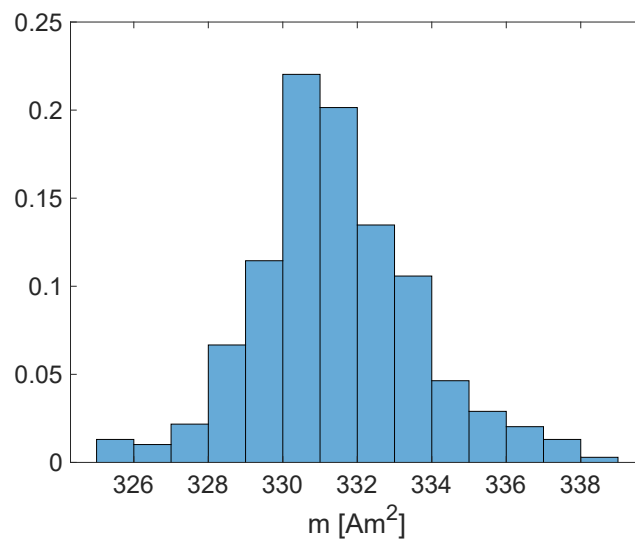
Fig. 1.12 Histogram of the measured magnetic moments on 690 PM blocks for the FASER experiment.

Chapter 2

State of the art

This Chapter presents the state-of-the-art measurement techniques used for the DC characterization of magnetic materials. A broad spectrum of measurement techniques is available, depending on different aspects such as the specimen shape, the detection principle, and the expected material behavior. This Chapter provides an overview of these techniques and highlights how these methods are complementary.

2.1 Classification of the characterization methods

The general approach to characterize the magnetic properties of a material is to apply a magnetic field **H** and detect the flux density **B**, and from this its magnetic state *M*. In general, test methods and specimens shapes determine a symmetric configuration that makes possible to express these fields as scalars. From Eq. 1.2, the material response *B* can be expressed as

$$B = \mu_0(M + H). \tag{2.1}$$

When the permeability is comparable to vacuum, $M \ll H$ and $B \approx \mu_0 H$, thus leading to the necessity of increasing H, and using high-resolution sensors. In the presence of a soft ferromagnetic alloy, $M \gg H$, and low excitation fields can be used. However, in the saturation region, M and H become comparable, so particular attention shall be dedicated to calibrating the sensor used to measure B.

The concept illustrated above shows how complementary methods are necessary to

measure materials having different behaviors. Different test methods are available, depending on the specimen shape, the detection principle, and the expected material behavior, independently from the test temperature. This distinction generated so far different standard test methods, from the IEC 60404 series to American Society for Testing and Materials (ASTM) standards. The measurements can be performed under static (DC) or quasi-static (quasi-DC), or dynamic (AC) conditions (sinusoidal regime). Pulsed field measurements can be included under the quasi-static conditions, because they are performed generally via flux-metric methods, with the field pulse followed by a plateau. In this dissertation, only DC and quasi-DC techniques are described, because magnets for particle accelerators are pulsed or operated in quasi-static conditions.

2.1.1 Closed-circuit and stray-field methods

An initial distinction between measurement techniques depends on the path of the field lines. If the field lines are confined in a loop, the technique is a *closed-circuit method*, and it can consist of particular specimen geometries such as toroids or of a specimen clamped between two magnet poles, closing a magnetic circuit. If the field lines are not confined in a loop, a demagnetizing field is present and therefore they are named *stray-field* methods or *open-circuit* techniques [11].
The distinction between closed-circuit and stray-field methods arises from Gauss's law for magnetism

$$\nabla \cdot \mathbf{B} = 0, \tag{2.2}$$

which implies that

$$\nabla \cdot \mathbf{H} = -\nabla \cdot \mathbf{M}. \tag{2.3}$$

In the absence of free sources, such as in the case of a permanent magnet, from Ampere's law $\nabla \times \mathbf{H} = 0$. Therefore, the field can be described as the gradient of a magnetic scalar potential ψ

$$\mathbf{H} = -\nabla \psi. \tag{2.4}$$

Combining Eq. 2.4 with Eq. 2.3, the magnetic scalar potential can be calculated by solving the following Poisson's equation

$$\nabla^2 \psi = \nabla \cdot \mathbf{M}. \tag{2.5}$$

The solution to this equation in a uniform magnetized body having volume V enclosed in a surface A is

$$\psi(\mathbf{r}) = -\frac{1}{4\pi} \int_V \frac{\nabla \cdot \mathbf{M}(\mathbf{r}')}{|\mathbf{r} - \mathbf{r}'|} dV + \int_A \frac{\mathbf{M}(\mathbf{r}') \cdot \mathbf{n}}{|\mathbf{r} - \mathbf{r}'|} dA, \tag{2.6}$$

where the gradient of the first term describes the volumetric contribution, called demagnetizing field $\mathbf{H}_d$, while the gradient of the second term, describes the field outside the magnetized body, generated by a fictitious magnetic surface charge $\mathbf{M}(\mathbf{r}') \cdot \mathbf{n}$. The field due to the second term is called stray field $\mathbf{H}_s$ and its direction is the same as $\mathbf{M}$. Fig. 2.1 provides visual identification of the two field components.
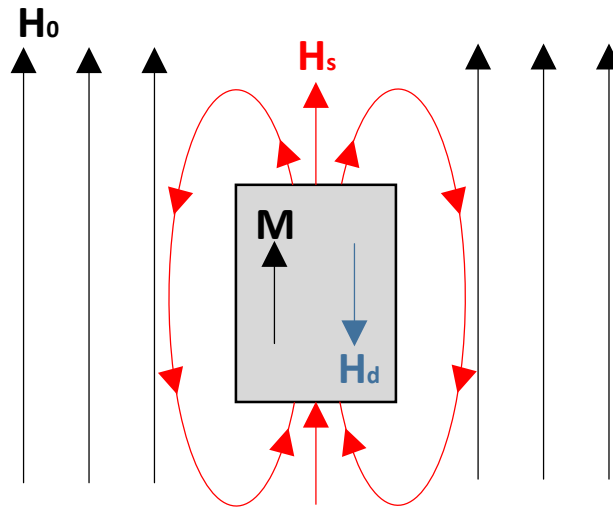
Fig. 2.1 Example of field contributions arising from a uniformly magnetized body. In black the external field $\mathbf{H}_0$ and the magnetization $\mathbf{M}$. In red, the stray field $\mathbf{H}_s$. In blue, the demagnetizing field $\mathbf{H}_d$. Adapted from [53].

In terms of magnetic materials' characterization, the properties of the test specimen have to be identified inside its volume. Therefore, the demagnetizing field $\mathbf{H}_d$ is the contribution that matters and can be expressed as

$$\mathbf{H}_d = -||N_d||\mathbf{M}, \tag{2.7}$$

where $||N_d||$ is called demagnetizing factor and it is a diagonal tensor. In most cases, such as soft ferromagnetic steels, the measurement of the material is performed by applying an external field $\mathbf{H}_0$. Therefore, due to the superposition principle, two fields are present, the external field and the demagnetizing field. If $\mathbf{H}_e$ is the effective field in the specimen volume:

$$\mathbf{H}_e = \mathbf{H}_0 - ||N_d||\mathbf{M}. \tag{2.8}$$

In closed-circuit methods, $\mathbf{H}_e = \mathbf{H}_0$. In fact, being the flux lines inside the test specimen confined on a closed path, $\nabla \cdot \mathbf{M} = 0$. In stray-field methods, $\mathbf{H}_0$ is applied, and $\mathbf{B}$ is measured. However, the effective field is the one that should be taken into account to describe the intrinsic properties of the material.

Evaluating the effective field relies on the knowledge of $||Nd||$, which mainly depends on geometrical factors and is generally evaluated using numerical methods to compute the magnetic scalar potential from Eq. 2.6 [53]. Usually, the computation is mainly performed via FE analysis. For regular geometries such as cylinders, spheres, ellipsoids, or prisms, analytical expressions have been determined [80, 81, 82]. The presence of the demagnetizing field limits the use of stray-field methods to characterize soft ferromagnetic steels because the demagnetizing field is not homogeneous, even in the presence of a uniform external field, and dependent on the relative permeability. For instance, spherical specimens can be used, where the demagnetizing tensor becomes a scalar, $N_d = 1/3$. However, external and demagnetizing fields becomes comparable, and the correction can be inaccurate [83].

In conclusion, soft ferromagnetic steels, having high permeability, are generally measured using closed-circuit methods because the low H-field to apply, in the order of a few tens kA/m, can be generated using an excitation coil. On the other hand, feebly magnetic materials are generally measured using stray-field methods because the contribution of the demagnetizing field can be neglected, and the high necessary field values, in the order of hundreds of kA/m, or higher, can be generated using a magnet.

2.1.2   Detection principles

The general measurement principle of a magnetic material is to apply a magnetic field H and detect the flux density B, as previously mentioned. The second classification depends on the detection principle of B:

- *Flux-metric methods*, where the magnetic state is detected by measuring the flux variations that can be either generated by a change in the material magnetization due to the application of a magnetic field or a change induced by the movement of the test specimen in a constant magnetic field. The sensor technology is the sensing coil, or pick-up coil, which displays a voltage proportional to the flux variations at its terminals. All the closed-circuit methods are based on this measurement principle.

- *Flux-distortion detection methods*, where the specimen, placed in a magnetic field, determines a local distortion of the field lines due to the presence of the stray field. This distortion depends upon the magnetization of the specimen and its geometry, as seen in Sec. 2.1.1, which can be mapped using a local field transducer and the magnetization, or the permeability, computed by inverse calculation. These methods are intrinsically stray-field methods.

- *Force detection techniques*, where the specimen permeability is detected by measuring a force, caused by the interaction between the external field and the specimen's magnetization. In the presence of a field gradient, a translatory force is applied to the specimen. In case the field is uniform, a torque is applied. This force can be detected through the apparent change of the specimen mass, proportional to the permeability, which can be measured with a scale.

- *Magneto-optical techniques*, where the detection is performed by investigating the material surface by magneto-optical Kerr effect [84]. It is used mainly in material research to visualize the domain walls, and steel grains [85, 86].

- *Magnetostrictive techniques*, where the specimen is measured by detecting its change of dimensions following the application of a magnetic field [87, 88].

Only the first three methods are accurately described in the following since they are the most used in industry and research applications. The same detection principle

can work on different specimen shapes, thus leading to the definition of a different standard. Some of these techniques are optimized to measure soft ferromagnetic steels, whereas others are universally used to test paramagnetic, and more generally, weakly magnetic materials.

2.2   Flux-metric methods

Flux-metric methods are a class of test methods where the magnetic state is measured by detecting flux variations in the specimen due to a magnetic field that changes the material magnetization. As previously mentioned in Sec. 2.1.2, flux variations are detected by a sensing coil, which exhibits a voltage proportional to the flux variations at its terminals.

Flux-metric methods can work in closed- and open-circuit configurations. Moreover, the causes of the flux variations determine another sub-classification:

- *Transformer principle*, if the specimen is kept still and a time-varying magnetic field is applied. This principle is behind most methods used for soft ferromagnetic steels.

- *Magnetometer principle*, where the specimen is moved in a constant field. This particular class of methods is generally used for weak magnetic materials and to characterize the remanent field of PM blocks.

The transformer principle is based on the application of a magnetic field H, either by using a primary excitation coil, as shown in Fig. 2.2, wound around the test specimen or by using an external field source (*i.e.*, dipole, or solenoid magnet).

For the former case, a current I is forced to circulate in the primary coil, and the magnetic field can be calculated as

$$H = \frac{N_e I}{l_m},$$ (2.9)

where N_e is the number of excitation turns and l_m the magnetic length. The magnetic length is a function of the specimen geometry. The time-varying magnetic field determines a change in the magnetization and, therefore, in the flux density B. The
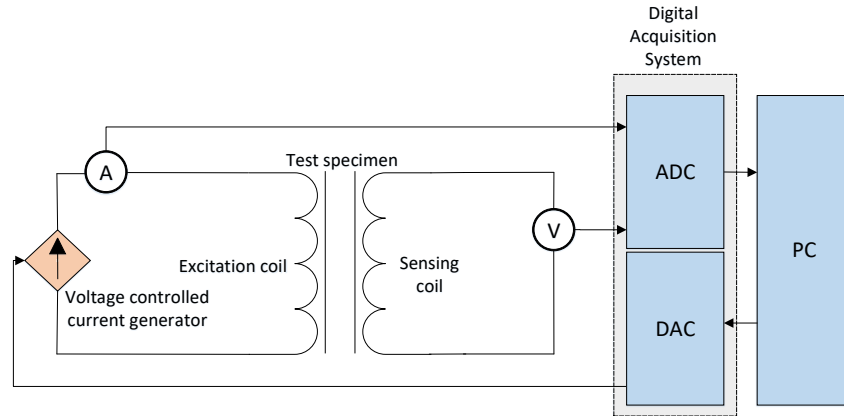
Fig. 2.2 General measurement system setup for material's characterization using the flux-metric method in the transformer configuration.

change of magnetic state determines magnetic flux variations $\Delta\Phi$, which can be measured by integrating the induced voltage across the terminals of the sensing coil

$$\Phi = \Phi_0 + \int_0^t v(\tau)d\tau, \tag{2.10}$$

where $\Delta\Phi = \Phi - \Phi_0$, with Φ_0 the initial flux. In materials' characterization, $\Phi_0 = 0$ because the material is generally measured from a demagnetized state, *i.e.*, virgin or obtained by electrical degaussing. From Eq. 2.10, the magnetic flux density B can be evaluated as

$$B = \frac{\Phi}{N_t A_s}, \tag{2.11}$$

assuming that the sensing coil is wound closely to the test specimen and that no flux leaks out of it (air-flux). A_s is the specimen cross-sectional area, and N_t is the number of sensing turns. Eq. 2.11 can be particularized to take into account the calibration of the sensing coil area and, therefore, the air-flux leakage. If the sensing coil is connected to an air-flux compensation coil, Eq. 2.11 can be applied as-is. If the area A_t of the sensing coil is known, *e.g.*, from calibration, Eq. 2.11 can be modified as

$$B = \frac{1}{A_s}\left(\frac{\Phi}{N_t} - \mu_0 H(A_t - A_s)\right), \tag{2.12}$$

to compensate the air flux in post-processing.

When the magnetometer principle is used, the field is kept constant, and the specimen is moved inside a constant magnetic field H_0 (*e.g.*, rotated, vibrated, and so on). The field distribution detected by the sensing coil is perturbed by the passage of the specimen, exhibiting a magnetization, with a stray field propagating from the surface. In this way, a spatial distortion of the field lines caused by the presence of the stray field is transformed in a field variation over time for the sensing coil. Generally, using a far-field approximation, the time-varying perturbation is related to a magnetic moment m, proportional to the flux Φ. Therefore,

$$B = \mu_0 \left(\frac{k\Phi}{N_t V} + H_0 \right) \tag{2.13}$$

where k is a calibration constant, usually obtained from a reference specimen, and V the specimen volume. This measurement principle is intrinsically an open-circuit method, and it is the principle of the vibrating sample magnetometer [10]. A particular case, where $H = 0$, called rotating sample magnetometer, is used to test the remanent field of permanent magnet blocks [89, 90, 91].

Flux-metric methods working on the transformer principle are widely used to characterize soft ferromagnetic steels because, owing to their high magnetization values, or equivalently high relative permeabilities, they behave as flux multipliers and therefore do not need high fields to characterize them. The available standard test methods [92, 93, 94] define two types of test procedures that can be used to measure the DC initial magnetization curve and the DC hysteresis loop. The first test procedure is the *continuous-recording* method, where the field is continuously ramped from zero up to the maximum magnetic field value. For the hysteresis loop, the field is reversed, and ramped down to the maximum negative field value, and finally reversed again, in a cyclic fashion. The ramp duration from zero to the maximum field is 60 s. Fig. 2.3 provides a visual example of the test cycle.

The other procedure is the *point-by-point method* or *ballistic method*. For the determination of the initial magnetization curve, the magnetic field is ramped back and forth between positive and negative symmetric plateau values. After each reversal, the amplitude is slightly increased. The measurement is performed in correspondence of the plateaus after the eddy current transient at the end of the previous ramp is fully damped. The transient duration depends on the material conductivity, relative permeability, and geometry. Examples of analytical description
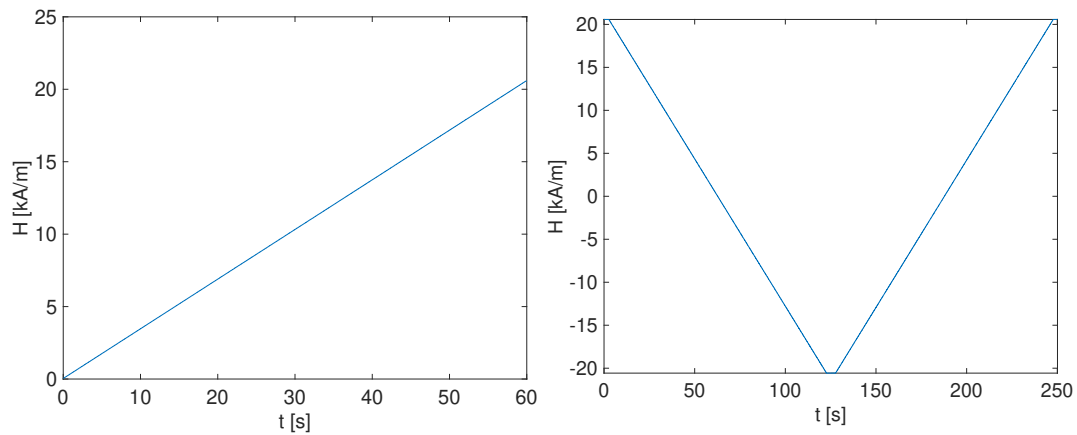
Fig. 2.3 Example of test cycles used for the determination of the initial magnetization curve (left) and the hysteresis loop (right) via continuous recording method.

of eddy currents in toroidal geometry can be found in [95, 96]. For specimen cross sections in the order of 100 mm^2, transient duration spans from less than 1 s for a FeSi alloy to about 5 s for pure iron, at room temperature. For the determination of the hysteresis loop, the specimen is brought into saturation state, kept as a reference value. From the saturation state, the magnetic field H is diminished step-wise until reaching the negative saturation and then reversed back, and increased step-wise until reaching the starting point. Fig. 2.4 provides a visual example of the test cycle for the point-by-point method.

Among the two techniques, if a sufficient plateau duration is adopted, the point-by-point method can be considered fully static (or true DC) in contrast with the continuous recording method, representing a low-frequency approximation. The results presented in Part. II, unless specified differently, are all measured by adopting the point-by-point method.

2.2.1   Ring technique

The ring technique is the application of the flux-metric method to specimens having a toroidal shape. The ring technique is one of the most used test methods to characterize soft ferromagnetic steels. The IEC 60404-4 standard [94] defines the guidelines for the specimen preparation and the operational procedure at room temperature. The specimen shall be cut from the main material slab to avoid heating and cold work,
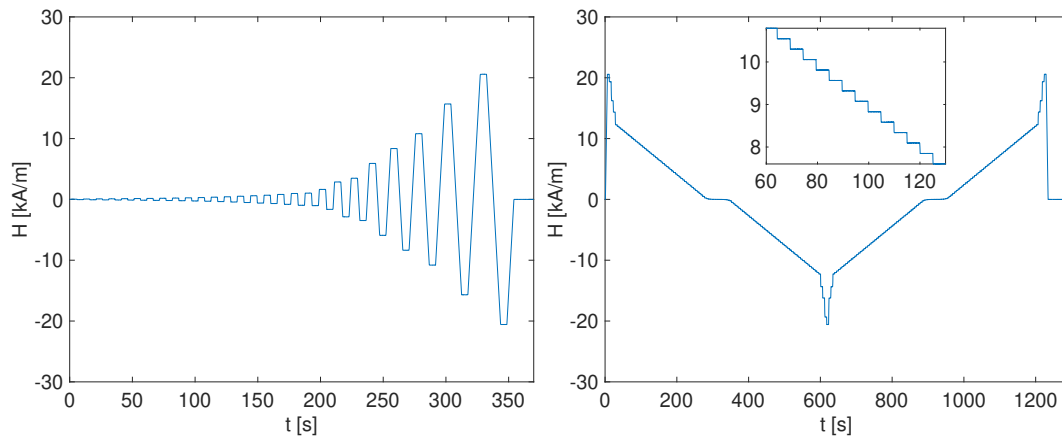
Fig. 2.4 Example of test cycles used for the determination of the initial magnetization curve (left) and the hysteresis loop (right) via point-by-point method. An in-view zoom is provided on the right chart to highlight the step-like variations of the magnetic field.

which influences the magnetic properties. One way to do this is to cut the specimen using water-jet cutting. The standard prescribes a ratio between outer and inner radius $r_1/r_2 \leq 1.1$ to limit the radial variation of the magnetic field. However, it is not unusual to have specimens with different ratios in the literature [97].
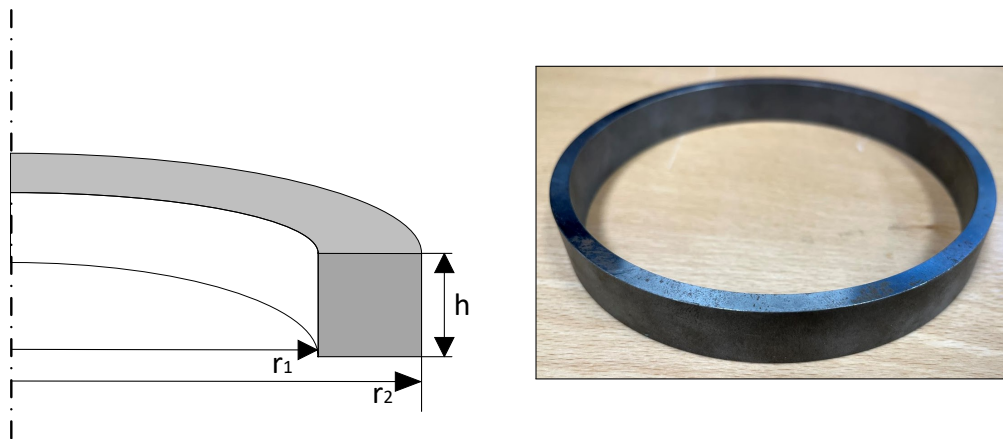
Fig. 2.5 (Left) Toroidal test specimen with relevant geometrical parameters and; (right) Example of IEC-compliant specimen having $r_1 = 52.5$ mm, $r_2 = 57$ mm, $h = 15$ mm.

In the case of a toroidal ring, the magnetic field can be calculated from the excitation current as

$$H(r) = \frac{N_e I}{2\pi r}, \tag{2.14}$$

where r is the radial coordinate. The radial dependency of the magnetic field can be eliminated by considering the field evaluated at the average radius $(r_2 + r_1)/2$, as prescribed by the IEC standard, or by considering the average field across the specimen cross-section:

$$H = \int_{r_1}^{r_2} H(r) dr, \tag{2.15}$$

yielding

$$H = \frac{N_e I}{2\pi r_0}, \tag{2.16}$$

where

$$r_0 = \frac{r_2 - r_1}{\log \frac{r_2}{r_1}}. \tag{2.17}$$

The specimen can be manually wound or an arrangement of rigid conductors that can be opened and closed to place the toroid can be used. The second option is the one implemented at CERN, and it is called split-coil permeameter [16, 35, 98, 99].

The bench consists of three separated coils made of a rigid 1-mm diameter conductor, having 90 turns each. The two outermost coils are connected in series to form the excitation coil. The innermost coil is used as a sensing coil. The excitation coil carries a current up to 40 A and generates a magnetic field up to 24 kA/m. The whole system is air-cooled to keep the specimen temperature variation within $\pm 5\,^{\circ}\text{C}$. The possibility of separating the coils allows to easily calibrate the system by performing a measurement without test specimen and imposing $B = \mu_0 H$. Therefore,

$$A_t = \frac{\Phi}{\mu_0 H}. \tag{2.18}$$
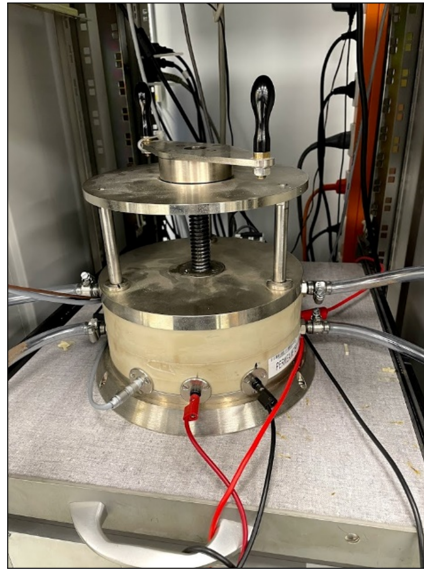
Fig. 2.6 The split-coil permeameter in operation at CERN.

2.2.2 Epstein frame technique

The Epstein frame technique is the application of the flux-metric method to steel strips defined according to the IEC 60404-2 [92]. The Epstein frame consists of an assembly of the strips in a square circuit, forming double-lapped joints at the corners. The excitation and the sensing coils are wound around the square formed by the strips. The test method is widely used for DC and AC characterization of FeSi alloys used in electrical motors [100, 101, 102, 103].

The strips shall have a length between 280 and 320 mm and a width of 30 mm, be burr-free and flat. The total number of strips shall weigh at least 240 g if the strips are 280 mm long. For the Epstein frame, the magnetic field is calculated assuming $l_m = 0.94$ m, according to the standard

$$H = \frac{N_e I}{0.94}.$$

(2.19)

However, different methods are proposed in the literature to provide a different estimate of the magnetic path length, constituting a source of systematic error [104, 105, 106].
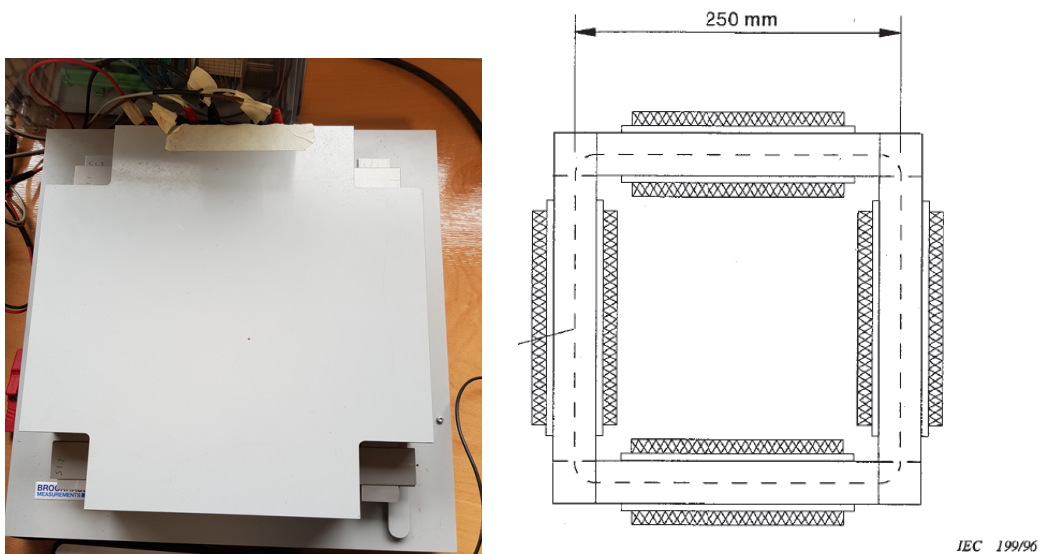
Fig. 2.7 (Left) A photograph of the Epstein frame operated at CERN; (right) Schematic of the Epstein frame from [92] (© 1995-2022 IEC).

2.2.3   Single-sheet tester

The single-sheet tester is the application of the flux-metric method to test a single slab of material, according to the standard IEC 60404-3 [93].
The method consists of winding the excitation coil and the sensing coil around the test specimen. The flux path is then closed through two C-shaped iron yokes, made of a FeSi alloy, having cross-sections much larger than the test specimen.
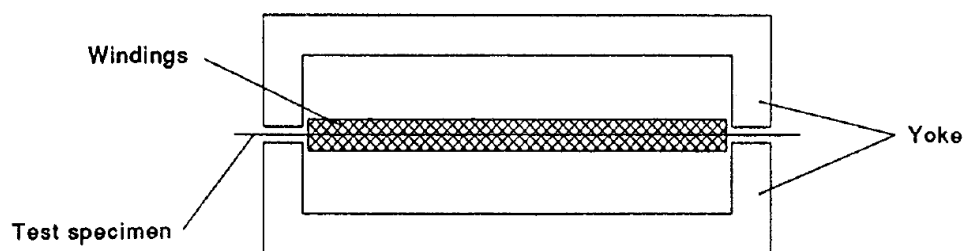
Fig. 2.8 Schematic of the single-sheet tester from [93] (© 1992-2022 IEC).

The length of the material slab shall be no less than 500 mm, the minimum width no less than 15 mm. The slab shall be burr-free and flat. The width of the pole faces shall be 25 mm. Similarly to the Epstein frame, Sec. 2.2.2, a conventional magnetic path length l_m =0.45 m is defined by the standard. Therefore,

$$H = \frac{N_e I}{0.45}.$$ (2.20)

The single-sheet tester is affected by the same problem of the Epstein frame, where a systematic error is introduced due to the definition of a conventional magnetic length. However, also for the single-sheet tester, different evaluation approaches of l_m are proposed in the literature [106, 107]. Moreover, air gaps at the interface between specimen and pole faces and the reluctance of the iron yoke branches determine an additional source of uncertainty.

A single-sheet tester, shown in Fig. 2.9, was in operation at CERN and used for the magnetic characterization of the steel sheets used for the LEP magnets [108, 109, 110].

Fig. 2.9 A photograph of the coercimeter, the single-sheet tester used in the past at CERN.

The system is a variant of the single-sheet tester. The two yoke parts are made of mu-metal, and therefore they behave as ideal "magnetic" short-circuits. Moreover, two couples of excitation and sensing coils are also present on the two yoke branches to evaluate the air-gap length at the interface between specimen and poles. After an initial measurement to evaluate the air gap, the current is commuted on the specimen excitation coil, and the measurement starts, following the usual procedure. The system is called coercimeter because it was mainly used to assess the coercivity of the steel sheets, which is independent from the air-gap length.

2.2.4 Vibrating sample magnetometer

The vibrating sample magnetometry (VSM), proposed for the first time in the literature by S. Foner [10] in 1956, relies on the flux-metric method operated with the magnetometric principle. The original measurement system layout initially proposed in the literature is shown in Fig. 2.10.
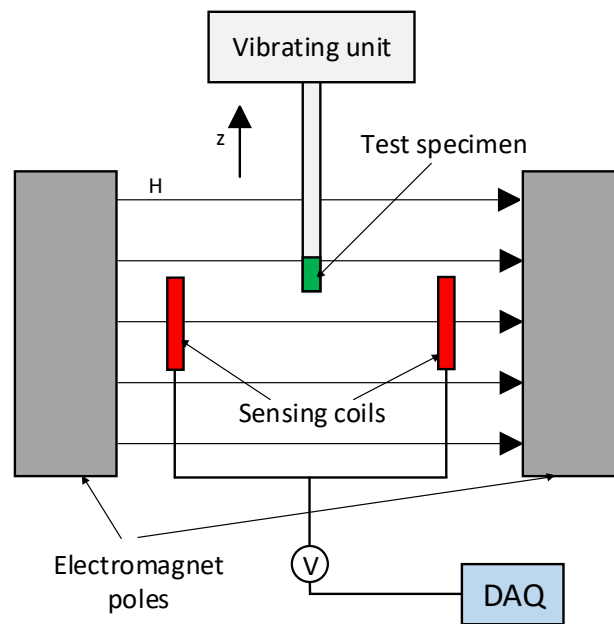
Fig. 2.10 Vibrating sample magnetometer layout. Adapted from [10].

The specimen is vibrated along the *z*-axis inside a constant magnetic field *H*, generated by an external source, namely a dipole magnet or a solenoid magnet. In the absence of the specimen, the induced voltage in the sensing coils is zero because there are no external field variations. When an external field is applied to test specimen, it contributes to the field with its stray field, generated by the magnetization. Therefore, when the specimen is vibrated, the vibration is detected and the signal can be integrated to obtain the magnetic flux. Given the typical low dimensions of the test specimens under test, a far-field approximation is used and the second source is modeled as a field generated by a magnetic moment, *m. m* is evaluated from the magnetic flux Φ by applying a calibration constant evaluated from a reference standard sample with known magnetic moment, *i.e.*, palladium. The evolution of the VSM, used in commercial instruments, includes the use of a superconducting sensing coil connected to a Superconducting QuantUm Interference

Device (SQUID). The system is also called SQUID magnetometer [111, 112, 113, 114]. The state-of-the-art sensitivity value is 10^{-8} emu, corresponding to 10^{-11} Am^2 and accuracy of about 10^{-7} emu [115]). The typical field values can reach up to 7 T, but examples are provided in the literature where higher fields, *e.g.* up to 13 T, are used [46, 116, 117, 118, 119]. Given the low uncertainty values, they are used for weak magnetic material characterization and for characterizing powders [120], thin films [121, 122] or magnetic nanoparticles [123].

2.3 Flux-distortion detection

Flux-distortion detection techniques, rely on the detection of the perturbation caused by the presence of the test specimen in a magnetic field. The standards ASTM A342/A342M-14 [124] and the IEC 60404-15 [125] report as measurement procedure the one adopted by the only commercial instrument working on this principle, the Foerster Magnetoscop® [126], manufactured by Institut Dr. Foerster GmbH & Co. The layout of the measurement instrument is reported in Fig. 2.11.
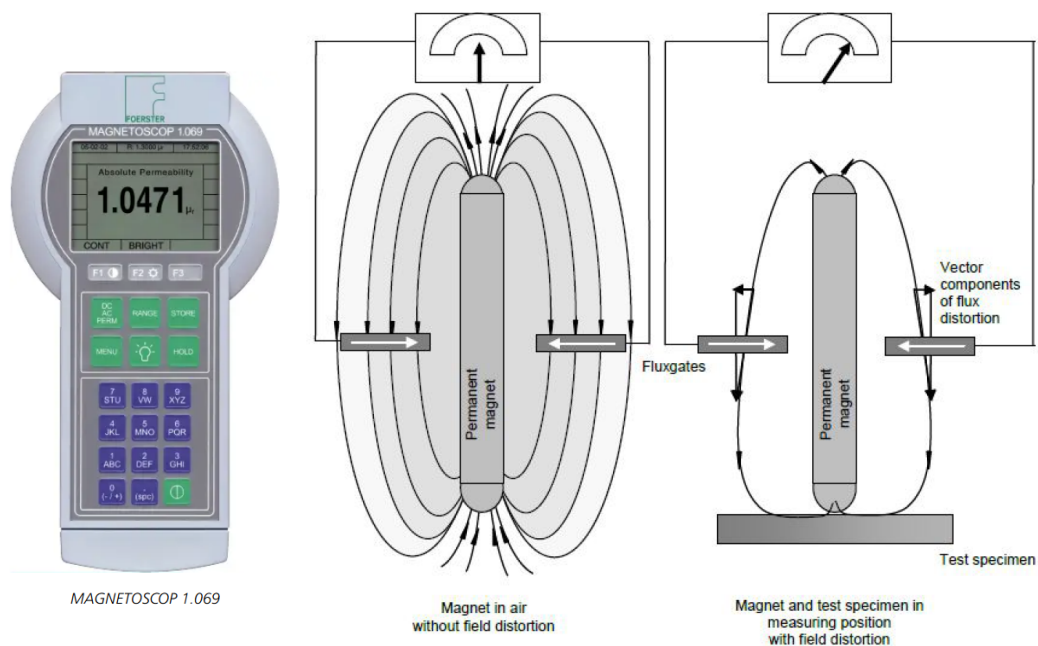
Fig. 2.11 (Left) Foerster Magnetoscop® 1.069 and; (right) schematic of its measurement principle. Adapted from [126].

The Magnetoscop® uses a PM block as a field source placed in contact with the specimen, preferably on a flat part. The distortion caused by the presence of the specimen is measured using two fluxgate magnetometers. The instrument has a resolution of 10^{-5} and an accuracy of 5 % and can be used to measure a test specimen or finished parts. The instrument is calibrated *in-situ* on reference standards with known permeability, and it has been proved to be excellent for specification acceptance and manufacturing control of finished parts.

2.4   Force detection techniques

Force detection techniques are generally used to characterize the permeability of feebly magnetic materials. When a magnetic field gradient exists, the test specimen is influenced by an attractive or a repulsive force, depending on the sign of the magnetic susceptibility, χ_m. In fact, the force $d\mathbf{F}$ acting on a local magnetic moment $d\mathbf{m}$ inside a field $\mathbf{H}$ is

$$d\mathbf{F} = (d\mathbf{m} \cdot \nabla)\mu_0\mathbf{H}. \tag{2.21}$$

By integrating Eq. 2.21 over the material volume V and considering that $d\mathbf{m} = \mathbf{M}dV$:

$$\mathbf{F} = \int_V \mu_0(\mathbf{M}dV \cdot \nabla)\mathbf{H} = \mu_0\chi_m \int_V (\mathbf{H} \cdot \nabla)\mathbf{H}dV. \tag{2.22}$$

Force detection techniques were historically implemented using the Gouy balance [127], the Faraday balance [128, 129], or the Evans balance [130]. The three techniques are very similar. In the Gouy balance, the test specimen is partially suspended in between the poles of a dipole magnet, where the gradient field is the highest because the specimen is in the fringe field region. In the Faraday technique, the specimen is completely immersed between two magnet poles, shaped such that a region where the product $H\frac{\partial H}{\partial z}$ is constant. In both of the aforementioned cases, the measurement setup is realized in such a way that the specimen moves in the direction of Earth's gravity. The magnetic susceptibility is measured by detecting the apparent change in the specimen's mass using an analytical balance. Fig. 2.12 shows the layout of a Gouy balance.
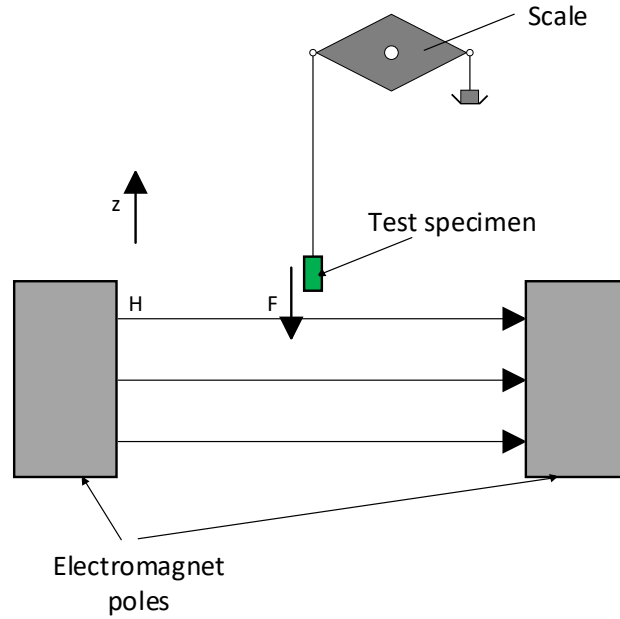
Fig. 2.12 Gouy balance layout. Adapted from [131].

$$\chi_m = \frac{2(\Delta m)g}{\mu_0 A H^2} \tag{2.23}$$

where g is the gravitational acceleration and A is the specimen's cross-section.
Force detection methods were originally limited to measurement laboratories because strong field magnets and high sensitivity instrumentation are required. Nowadays, they are implemented using a Neodymium permanent magnet and an electronic balance with a resolution of 0.001 g [132, 133], making the setup inexpensive and allowing to measure susceptibilities in the order of 10^{-5} with an uncertainty ranging between 15 % and 30 % of the measured value.

2.5   Test temperature

The different measurement principles available for magnetic characterization of materials work independently from the test temperature, as previously also mentioned in Sec. 2.1.
The susceptibility of diamagnetic materials is independent on the field and temperature, as already mentioned in Sec. 1.2.1. For paramagnetic materials, as mentioned

in Sec. 1.2.2, the magnetic susceptibility depends on the temperature as a result of Curie's law

$$\chi_m = \frac{k_C}{T}, \tag{2.24}$$

where k_C is the Curie's constant, dependent on the material, and T the temperature. Therefore, the susceptibility of paramagnetic materials increases as the temperature decreases. This law is an approximation for low fields and $T \to \infty$. For low temperatures and high fields, saturation should be considered, and Eq. 1.5 or Eq. 1.7 should be used to determine the susceptibility.

A relation similar to Eq. 2.24, the Curie-Weiss's law, can be used to describe the susceptibility of a ferromagnetic material above the Curie's point, where the material behaves as a paramagnet

$$\chi_m = \frac{k_C}{T - T_c}, \tag{2.25}$$

where T_c is the Curie's temperature.

Below Curie's point, the description becomes more complicated due to different energy exchange mechanisms occurring at microscopic level [12, 17], and determining a dramatic increase of the magnetic susceptibility, up to values greater than 1000. However, some analytical relations were obtained for the saturation region, where the magnetization is mainly dominated by domain rotation, similarly to a paramagnet. In fact, as shown in [12], the saturation magnetization increases as the temperature decreases. This behavior arises from an energy balance where exchange interactions between magnetic moment, grouped in domains, and thermal fluctuations. Thermal fluctuations oppose the magnetization and determine its value decrease until Curie's point, after which the material behaves as a paramagnet.

The dependency of the saturation magnetization as a function of the temperature can be derived by solving the following system of equations, similar to the description of a paramagnetic material (see Eq. 1.7),

$$\begin{cases} \frac{M}{M_s} = B_J(q) \\ q = \frac{g_J \mu_B J (\mu_0 H + \lambda M)}{k_B T}, \end{cases} \tag{2.26}$$

where for ferromagnetic elements, a transcendent system of equations is obtained. Solutions for different values of J were published in [134]. Fig. 2.13 show the theoretical saturation magnetization as a function of the temperature, normalized with respect to the value at 0 K, for three different ferromagnetic elements. The results presented in [134] were used, where $J = 5/2$ was used for iron and $J = 1/2$ for nickel and cobalt
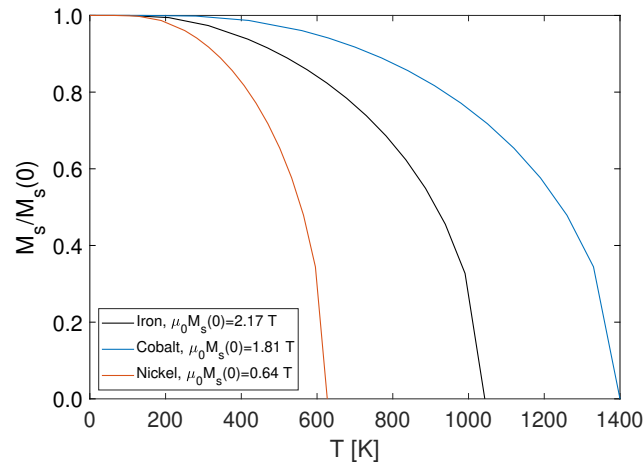
Fig. 2.13 Normalized saturation magnetization as a function of the temperature for three different ferromagnetic elements, evaluated using the tables in [134].

At low temperatures, close to 0 K, the behavior of the saturation magnetization can be approximated using Bloch's $T^{3/2}$ law [135],

$$\frac{M_s(T)}{M_s} = 1 - \left(\frac{T}{T_c}\right)^{\frac{3}{2}}. \tag{2.27}$$

For lower magnetization values, in the region of the hysteresis loop across the coercive field, the physics becomes more complex because also anisotropy participates in the energy balance. Moreover, most materials are not single crystals and are not pure elements because they are used in the form of alloys. Therefore, this justifies the need to characterize soft ferromagnetic materials at their operating temperature. An increase of coercive field and a decrease of peak permeability occurs when the temperature decreases, due to the growth of the inter-domain closure regions [136], which increases the anisotropy. As mentioned in Sec. 1.2.3, domain walls' motion is the prevailing phenomenon in the regions corresponding to H_c and $\mu_{r,max}$. Characterizing materials at temperatures different from room temperature adds extra

complexity to the measurement setup because the test specimen needs to be placed in an adiabatic environment. Depending on whether the test temperature is higher or lower than room temperature, a distinction should be made. Measurements at high temperatures are of interest for electric vehicles, where temperatures up to 200 °C can be found. An example of characterization of a ring specimen, made of non-oriented silicon steel (35A360), up to 800 °C is presented in [97], showing that the peak permeability increases as the temperature increases, and a reduction of the iron losses with temperature. Another example on toroidal specimens is presented in [137]. In [138], measurements up to 100 °C were performed by using a small-sized single-sheet tester. In both cases, the entire setup is placed in an oven. For vibrating sample magnetometry, it is unnecessary to place the whole setup at the test temperature, and temperature control can be implemented using a variable-temperature holder. An example for high temperature applications is shown in [139].

Low-temperature applications are much more common in the literature and are mainly used for research in physics, material science, and energy conversion. Measurements of stainless steels at 1.9 K or higher are common because they are performed by using high field VSMs, where high-field superconducting magnets are used [140, 141]. On the other hand, cryogenic characterization of soft ferromagnetic steels is less common. Usually, due to space constraints in the cryostat, ring test is preferred [142] and the test temperature is often 77 K, even though a few examples of measurements at 4.2 K can be found [143, 144]. The example provided by Pei et al. in [142] shows that the temperature can be spanned using commercial variable-temperature cryostats and presents measurements performed at 21 K, 42 K, 60 K, 131 K, and 180 K.

Part II

Characterization of magnetic materials at extreme ranges of field and temperature

Chapter 3

Context and problem statement

In Part II, a novel measurement device, the superconducting permeameter, is presented for the magnetic characterization of soft ferromagnetic alloys at flux densities up to 3 T and cryogenic temperatures. The system works on the flux-metric method, and more in detail, the ring method was adopted. This Chapter presents context and motivation that led to the development of the superconducting permeameter by presenting the results of a 5-years study performed on ARMCO Pure Iron® Grade 4, the selected material to be used as the iron yoke of the new superconducting magnets for the High Luminosity upgrade of the LHC. In particular, the results of a first study aiming at selecting the annealing sequence are briefly summarized. Moreover, the series measurements for the production of 1800 tonnes of steel are presented to assess how uniform the magnetic properties are among different production batches. This work was done in collaboration with A. Parrella, who started it out in 2015, and part of the results presented in this Chapter was also previously published in [P1]. The data reported in Sec. 3.2 and Sec. 3.3 were re-processed with respect to the published version to correct the systematic error introduced by the residual of degaussing ($\Phi_0 \neq 0$).

3.1   ARMCO® Pure Iron for the HL-LHC supercon-
ducting dipole and quadrupole magnets

The High-Luminosity Large Hadron Collider is the forthcoming upgrade of the
LHC with the scientific goal of exploiting the LHC's full capacity by reaching an
integrated luminosity level of about ten times the initial design target [2]. This
upgrade will be implemented by installing new stronger superconducting magnets,
RF crab cavities, additional collimators, upgrade of the injection chain (LIU project),
exploiting new technologies in the domain of superconductivity, cryogenics, and
electronics.

The iron yoke of the LHC superconducting magnets installed in the 2000s is
made of MAGNETIL BL®, a low-carbon steel, manufactured by Cockerill Sambre-
ARCELOR Group [59, 145, 146]. However, for the HL-LHC a different material
was chosen, because MAGNETIL BL® was not available at the moment of the
tender.

The iron yoke of the new superconducting magnets, therefore, will be realized in
ARMCO® Pure Iron Grade 4 from AK Steel, as specified by the CERN requirements
[147]. This material has been extensively characterized for the past five years in
view of the production of 1800 tonnes.

ARMCO® Grade 4 is a low-carbon steel that becomes chemically pure during the
melting process, and presents a maximum carbon content of 0.003 %, with lower
values of other elements such as nitrogen, cobalt, oxygen, and sulfur. AK Steels
declares ARMCO® with a purity of more than 99.85 % Fe [148].

Table 3.1 Chemical composition of ARMCO® Pure Iron Grade 4 [148]

Element	Max. %
Carbon (C)	0.0010
Manganese (Mn)	0.060
Phosphorus (P)	0.005
Sulfur (S)	0.003
Nitrogen (N)	0.005
Copper (Cu)	0.03
Cobalt (Co)	0.005
Tin (Sn)	0.005

The steel is hot-rolled at 800 °C, air-cooled, non-aging type, and delivered in 4000×750 mm^2 sheets with a thickness of 5.8 mm. Although the steel has only marginal mechanical properties, the grade is mechanically adequate for operation at 1.9 K. The sheets accepted by CERN have an ASTM grain size lower than 6, thus they have an average area greater than 2016 μm^2. In addition, they have a yield strength of about 180 MPa and an ultimate tensile strength of around 300 MPa.

3.2 Choice of the annealing sequence

An initial set of 5 specimens was machined and delivered in 2015 to determine the most appropriate annealing sequence through magnetic measurements. As previously illustrated in Sec. 1.4.1, the annealing consists of a thermal treatment aiming at boosting the magnetic properties, H_c and $\mu_{r,max}$ in particular, by allowing a better diffusion of the pinning sites, and therefore improving the domain wall's motion, and for high-temperature annealing, even increasing the grain size.
The five specimens were hot rolled at 700 °C, and treated at different hold temperatures and different durations.

Table 3.2 Annealing sequence for the five specimens of ARMCO$^®$ Pure Iron

Specimen	Thickness [mm]	Annealing temperature [°C]	Annealing time [h]
A	6.03	Not Annealed	0
B	6.06	750	1
C	6.10	750	5
D	6.10	850	1
E	6.07	850	5

The specimens are toroids having 114 mm outer diameter, 76 mm inner diameter, and realized by stacking three smaller toroids, as shown in Fig. 3.1. The thickness of each of the small toroid is reported reported in Tab. 3.2. The initial magnetization curves were measured using the flux-metric method at room temperature, adopting the point-by-point method, and by means of the split-coil permeameter, already shown in Sec. 2.2.1.

The measured initial magnetization curves and corresponding relative permeability values are shown in Fig. 3.2. The results are also summarized in Tab. 3.3. The

Fig. 3.1 First set of ARMCO® Pure Iron specimens to be tested

uncertainty of the *B*-values is 3 % due to a low scattering of the data at fields below 1.5 T. No reliable DC hysteresis measurements were performed at the time. The coercive field H_c and remanence B_r values shown in Tab. 3.3 were evaluated from the measurements presented in Sec. 3.4, repeated three years later.
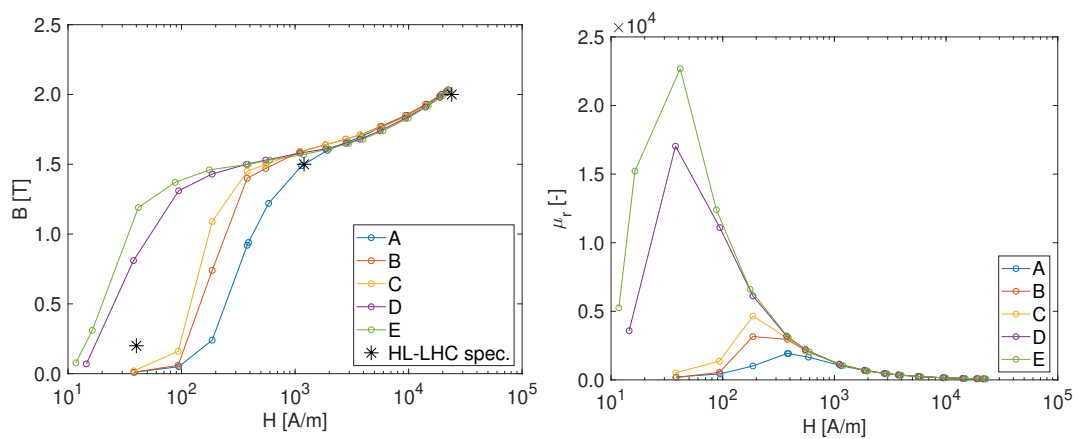
Fig. 3.2 Initial magnetization curves and corresponding relative permeability values for the five specimens of ARMCO® measured in 2015 [courtesy of A. Parrella].

The magnetic performance of the specimens progressively improves as the annealing treatment becomes more severe. The impact of the annealing is particularly evident on the peak permeability, which increases up to one order of magnitude, and the coercive field, which decreases by about the same factor. The remanence also increases, from 1.24 T in specimen A to 1.53 T in specimen C. The impact of the annealing is negligible at fields greater than 2 kA/m, where the material is approaching the saturation region. In fact, in that region, the magnetization dynamics are mainly

Table 3.3 Summary of the test results from the measurement campaign performed in 2015 on the five specimens of ARMCO®

Specimen	A	B	C	D	E	Spec.
B |40 A/m [T]	0.01	0.01	0.02	0.81	1.19	0.2
B |1.2 kA/m [T]	1.49	1.59	1.59	1.58	1.57	1.5
B |24 kA/m [T]	2.05	2.05	2.05	2.05	2.03	2
$\mu_{r,max}$	1928	3158	4659	17040	22675	
H_c [A/m]	268	196	170	36	33	
B_r [T]	1.24	1.51	1.53	1.43	1.47	

dominated by domains' rotation rather than walls' motion, and the *B*-values depend only on the chemical composition, as previously illustrated in Sec. 1.4.1.

Among the five test specimens, only specimens D and E fully respected the requirements for the HL-LHC magnets and were initially selected for cryogenic measurements. Specimen D was tested only in liquid helium (4.2 K) and specimen E in liquid nitrogen initially and then in liquid helium (77 K, 4.2 K).

3.3 Operation temperature dependency

The iron yoke of a superconducting magnet is immersed in a helium bath, at a temperature between 4.2 K and 1.9 K. Therefore specimen E, initially selected as the candidate material, was measured at cryogenic temperatures to assess its performance at operation temperature. The test was performed in liquid helium, at 4.2 K instead of 1.9 K, to keep the measurement layout simple and because no significant variations of the magnetic properties were expected from 4.2 K to 1.9 K, in light also of the curves shown in Fig. 2.13. Fig. 3.3 shows the results of a more extensive test, including also the measurements performed at 77 K.

The material softening decreases significantly as the temperature decreases. This effect is visible on the peak permeability, where a decrease up to one order of magnitude can be observed. This reduction was expected because decreasing the temperature makes the inter-domain closure regions grow, increasing the hysteresis anisotropy constant [136]. In the saturation region, the flux density increases by about 1 % due to Bloch's $T^{3/2}$ law (see Sec. 2.5). However, the observed decrease of peak permeability was not expected. The three curves were expected to be closely comparable, similarly to MAGNETIL® [59]. This behavior might be explained
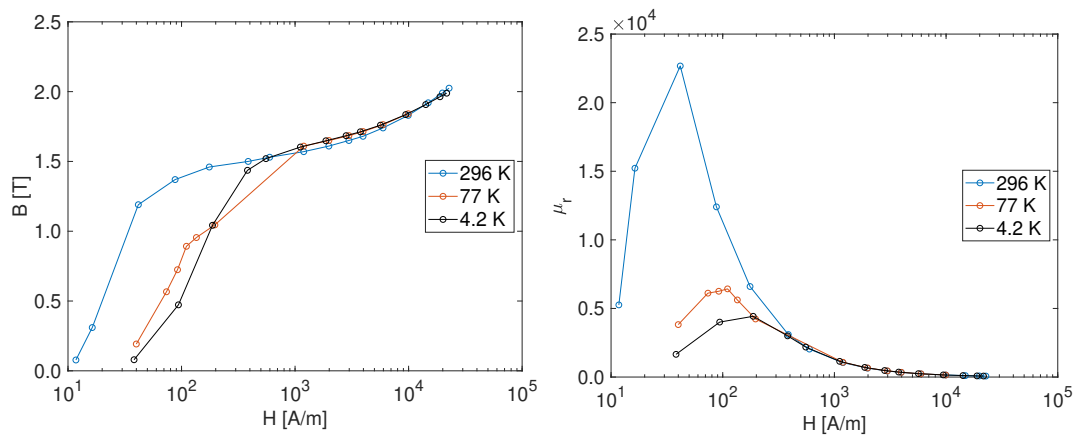
Fig. 3.3 Initial magnetization curves and corresponding relative permeability values for the ARMCO® specimen E [courtesy of A. Parrella].

as an effect of the material degradation, illustrated in Sec. 3.4, due to the applied mechanical strain on the specimen when cooled down to cryogenic temperatures. The results show a qualitative trend, but they are inaccurate. The uncertainty of the *B*-values is 5 %, mainly due to underestimating the eddy currents' decay duration in the low-field region, 5 s against 30 s, which led to underestimating the flux density values. Another contribution is given by neglecting the thermal contraction of the specimen, between 2 ‰ and 3 ‰ of the cross-section (see Sec. 4.2), from 293 K to 4.2 K. Moreover, the curves measured at cryogenic temperatures intersect with the one measured at 293 K, due to a poor calibration of the sensing coil. The calibration issue has been fixed for the results presented in Chap. 5, using the procedure presented in Sec. 4.2.

3.4 Loss of annealing performance

The five specimens of Sec. 3.2 were re-measured in 2018 to evaluate the impact of aging and the stability over time. The measurement results are shown in Fig. 3.4 and Fig. 3.5, and summarized in Tab. 3.4. The DC hysteresis curves were evaluated by using the point-by-point method.

The specimens D and E showed a severe degradation with the peak permeability decreased to less than 6000. Their coercive fields increased by a factor of about

(a) Specimen A

(b) Specimen B

(c) Specimen C

(d) Specimen D

(e) Specimen E

(f) Relative permeability values
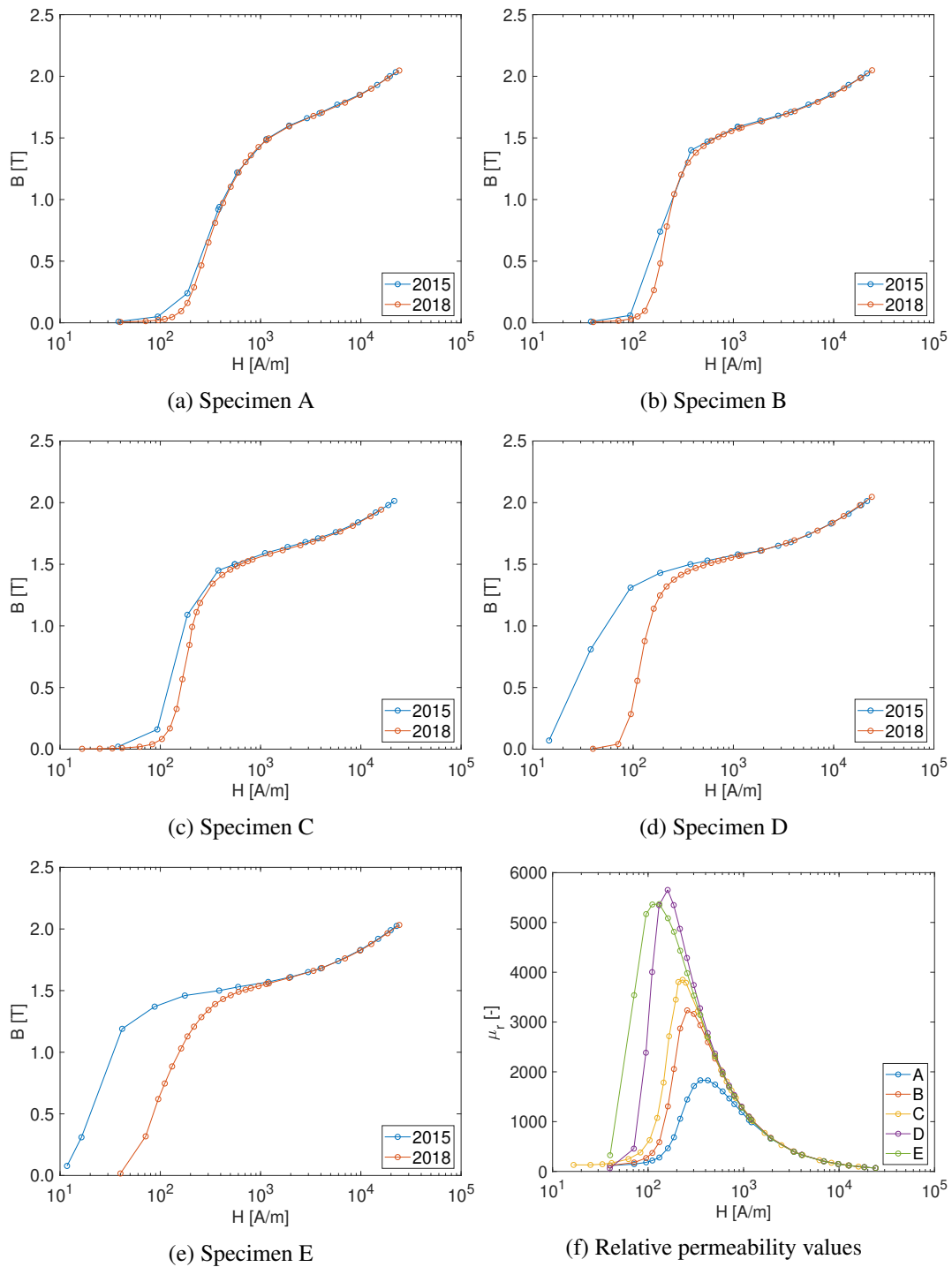
Fig. 3.4 Initial magnetization curves and corresponding relative permeability values for the five specimens of ARMCO® measured in 2018 (red) and compared with the measured values of Fig. 3.2.
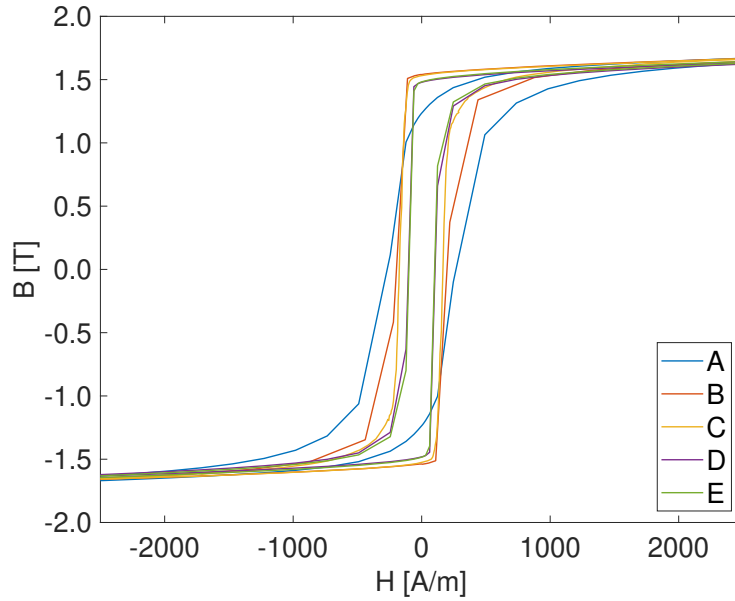
Fig. 3.5 Hysteresis loops

Table 3.4 Summary of the test results from the measurement campaign performed in 2018 on the five specimens of ARMCO®

Specimen	A	B	C	D	E	Spec.
B |40 A/m [T]	0.006	0.006	0.009	0.003	0.0163	0.2
B |1.2 kA/m [T]	1.496	1.585	1.585	1.573	1.559	1.5
B |24 kA/m [T]	2.047	2.049	2.048	2.049	2.032	2
$\mu_{r,max}$	1830	3235	3982	5653	5361	
H_c [A/m]	268	196	170	103	100	
B_r [T]	1.236	1.512	1.529	1.479	1.482	

3. The other test specimens did not show a significant change in their magnetic properties. The same coercive field and the remanence values were previously reported in Sec. 3.2. For specimens D and E, since the conductivity of the material is constant over time, the values of H_c in 2015 were estimated as

$$H_{c,2015}^{DC} = H_{c,2018}^{DC} - (H_{c,2018}^{R} - H_{c,2015}^{R}), \tag{3.1}$$

where $H_c^{D}C$ are the DC values and H_c^{R} are the values estimated by continuous recording method, at a ramp rate of about 3057 $\mathrm{Am^{-1}s^{-1}}$.

The only possible hypothesis of specimen D and E degradation is the thermal bath at cryogenic temperatures and, in particular, the fast cooling rate of the specimen.

In fact, the liquid cryogen was directly poured on the specimens, and therefore they underwent a temperature variation of more than 290 °C, with a cooling rate between 4 and 6 K/min. This thermal shock may have generated internal strains that did not disappear once the specimens were brought back at room temperature, determining a higher coercivity and a lower peak permeability.

Another potential reason is that the improvement of the magnetic properties of the two selected specimens, which received the most severe annealing sequences, was unstable. The same thermal cycle was applied to specimen B to verify this, which was immersed in the helium bath and returned to room temperature for further measurements. The results are shown in Fig. 3.6.
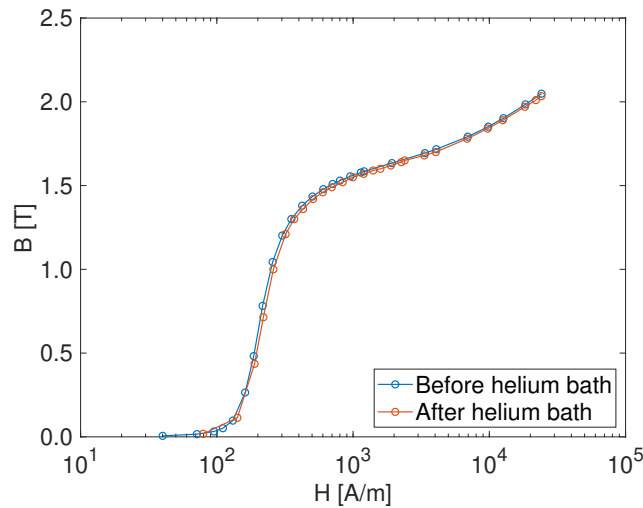
Fig. 3.6 Initial magnetization curves of the specimen B before (blue) and after (red) the helium bath.

No significant variations were measured. Therefore, the conclusion is that the more severe is the annealing sequence, the more unstable is the final state, and therefore, the more likely it is that the material loses the annealing boost if it undergoes severe stress such as the thermal shock of a cryogenic bath.

This problem, combined with surface scaling issues introduced by the annealing, led to the decision to remove the annealing from the production process, thereby saving about 9 % of the budget. Therefore, the steel chosen for the production is not annealed and hot-rolled at a higher temperature, 800 °C.

3.5   Effect of the cold working on the magnetic properties

Another measurement campaign was performed on three test specimens before the series measurements to verify how the mechanical stress applied to the material's coils impacts the magnetic properties during the production process. Three test specimens were delivered, A25112-3, A25114-4, and A25112-4, shown in Fig. 3.7. The specimens were initially measured as delivered. Afterward, the first two specimens were bent by 6 mm and the last one by 4 mm. The specimens were finally measured after the bending. The values of the applied deformation were chosen to simulate a worst-case scenario because such deformations usually do not occur in the material's main coil.
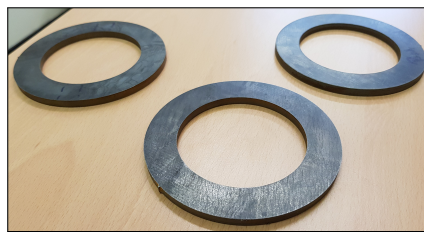
Fig. 3.7 Second set of ARMCO® Pure Iron specimens to be tested

Fig. 3.8 and Fig. 3.9 show the results of the measurement campaign. Fig. 3.8 shows the initial magnetization curves and their corresponding relative permeability values for the three test specimens, measured before and after the application of the bending deformation. Fig. 3.9 shows the relative degradation of the initial magnetization curves and the hysteresis loop of specimen A25112-4 to show how the cold work impacted the hysteresis loop shape. The uncertainty of the *B*-values is the same as in Sec. 3.4. The hysteresis loops were measured by continuous recording method, resulting only in a doubled coercive field value with respect to the point-by-point method.

The cold work degraded the magnetic properties, with the degradation values following the same trend showing the most significant impact at low fields, in correspondence of the initial relative permeability, where differences up to 40 % were detected. In correspondence of the peak permeability, the differences are between the 10 % and 20 %. The impact is negligible at fields greater than 5 kA/m, where the material is approaching the saturation region. The degradation of the magnetic prop-

(a) A25112-4 - Initial magnetization

(b) A25112-4 - Relative permeability

(c) A25112-3 - Initial magnetization

(d) A25112-3 - Relative permeability

(e) A25114-4 - Initial magnetization

(f) A25114-4 - Relative permeability
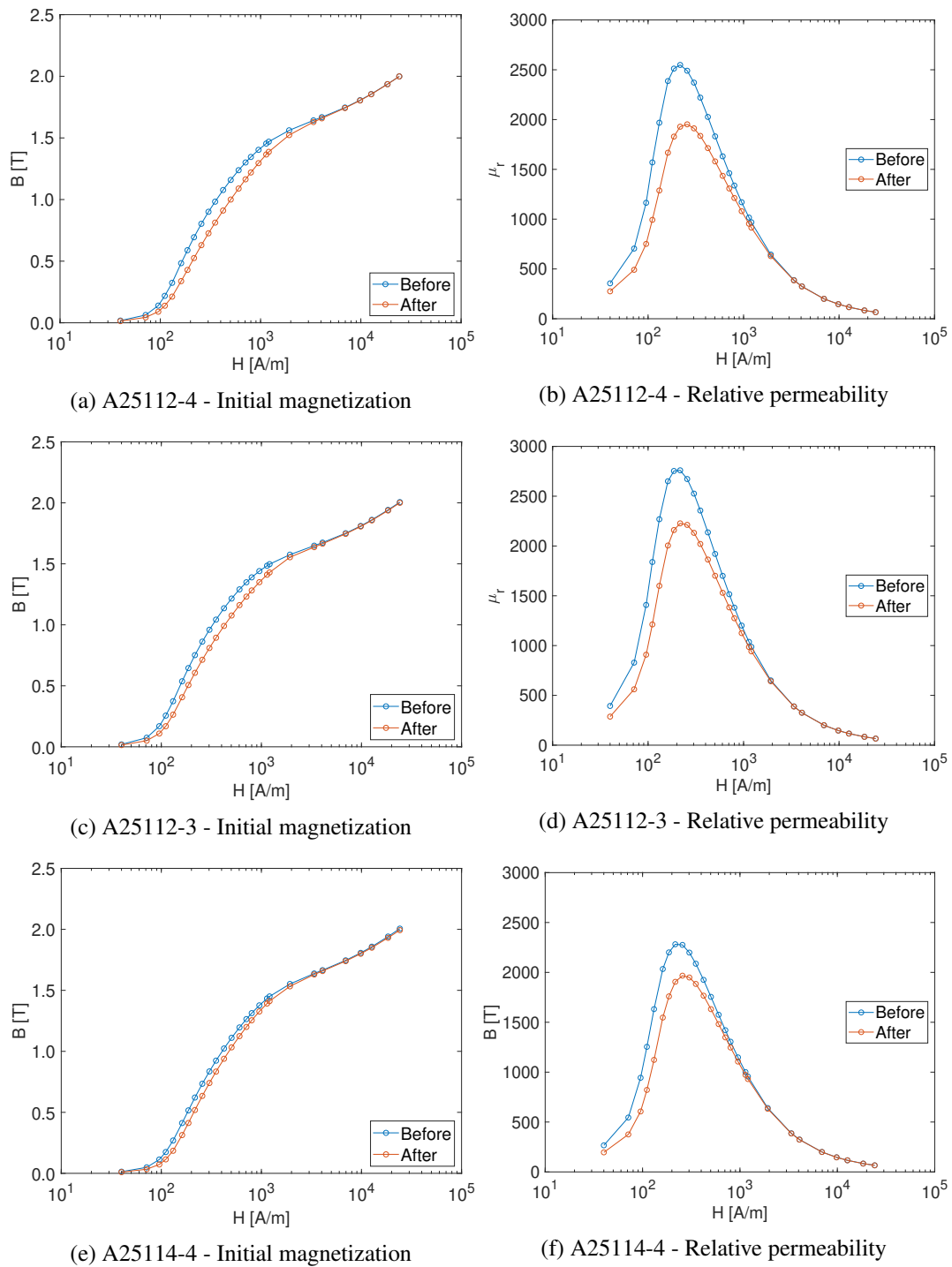
Fig. 3.8 Initial magnetization curves (left) and corresponding relative permeability values (right) for the second set of three specimens of ARMCO® measured before and after the application of the bending deformation.

(a) Relative variation

(b) A25112-4 - Hysteresis loops
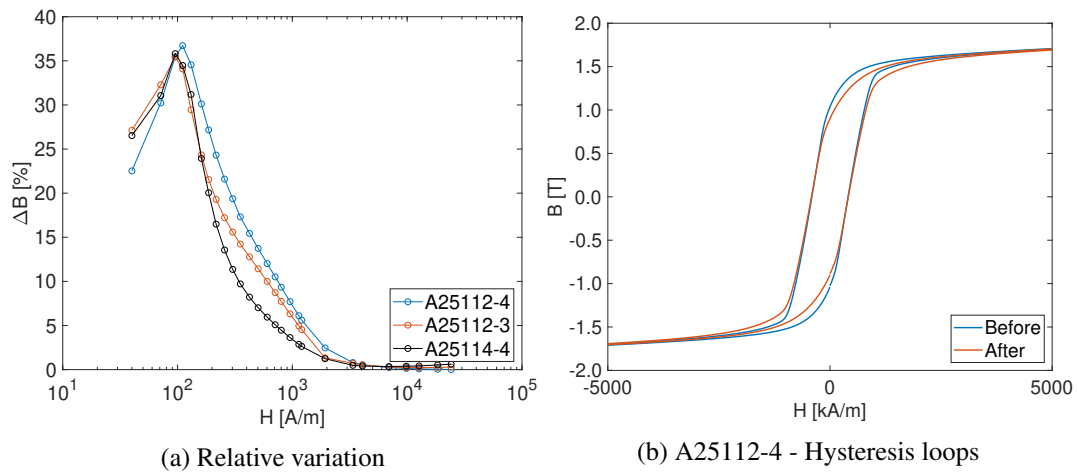
Fig. 3.9 Flux density relative degradation for the three specimens (left) and hysteresis loop of specimen A25112-4 measured before and after the bending deformation (right).

erties is reproducible among the three specimens, and slightly higher values of ΔB, up to 5 %, occur when the bending deformation is higher (specimen A25112-4). The coercive field remained unaltered, whereas a significant decrease of the remanence was detected, from about 1.04 T to 0.9 T.

As a conclusion of these two test campaigns, the properties of ARMCO® can be boosted through an annealing process. However, the effect of a more severe annealing process can be lost if the material is cycled between room and cryogenic temperature. Moreover, being the material a high-purity iron, degradation of its magnetic properties when it is cold-worked was expected, as previously mentioned also in Sec. 1.4.1.

3.6   Series measurements for the production

The production of the 1800 tonnes of ARMCO® Pure Iron was followed up by a series measurement campaign. A batch of 26 test specimens was measured to assess the quality of the production and the sample-to-sample repeatability. Two test specimens were cut from 13 primary coils. Each specimen has 114 mm outer diameter, 76 mm inner diameter, and 5.8 mm thickness.

Fig. 3.10 shows the results of the series measurement in terms of initial magnetization curves and corresponding relative permeability values. Fig. 3.11 shows the DC hysteresis loops, evaluated by using the point-by-point method. Finally,

Tab. 3.5 summarizes the results of the series measurement campaign, where the requirements for the HL-LHC magnets and the results of specimens A and B from the pre-production are reported for comparison. The measurement uncertainty of the *B*-values is of about 1 %.
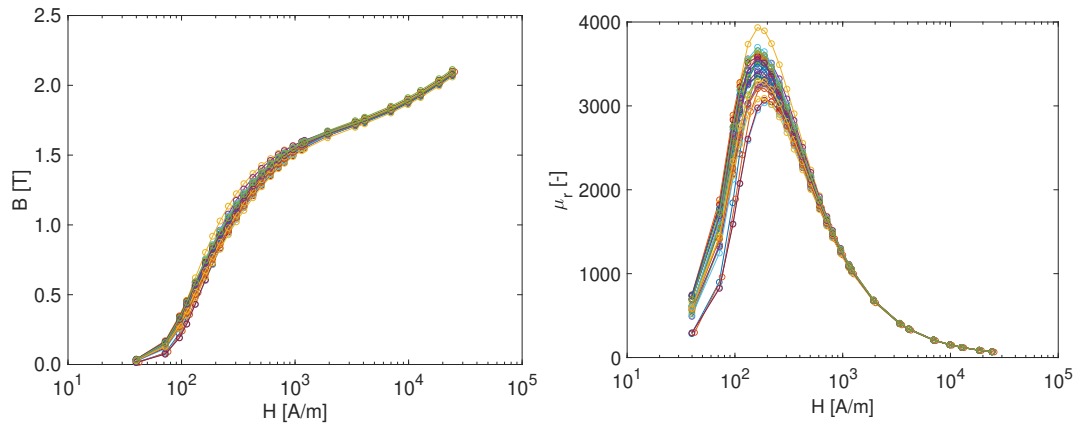
Fig. 3.10 Measured initial magnetization curves and corresponding relative permeability values of ARMCO® during the series measurement.
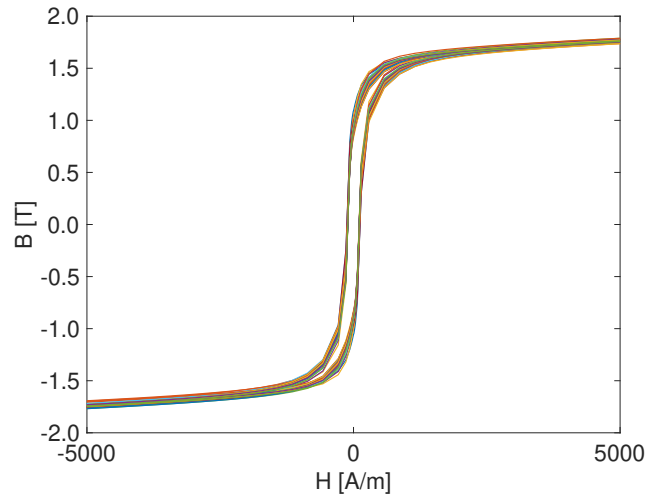
Fig. 3.11 Measured hysteresis loops of ARMCO® during the series measurement.

The material properties are uniform within the 1 % range above 1.8 T, where the saturation region is approached. Such dispersion might be due to a combination of measurement uncertainty and impurity inhomogeneities within the material batch. The material properties are much less uniform in the low field region, where a significant dispersion of 25 % and up to 50 % was measured. In terms of coercive field H_c,

Table 3.5 Summary of the test results from the measurement campaign performed in 2018 on the five specimens of ARMCO®

Specimen	Production	A	B	Spec.
B ∣40 A/m [T]	0.029±0.007	0.006	0.006	0.2
B ∣1.2 kA/m [T]	1.567±0.016	1.496	1.585	1.5
B ∣24 kA/m [T]	2.089±0.012	2.047	2.049	2
$\mu_{r,max}$	3439±215	1830	3235	
H_c [A/m]	112±6	268	196	
B_r [T]	0.926±0.060	1.236	1.512	

variations up to 5 % were measured.

The results generally respect the requirements for HL-LHC, except for a few specimens that do not respect the specification on the low field value. However, as the application is for superconducting magnets, this is not critical because the iron contributes to no more than 20 % to the total field in the gap (see Sec. 1.3. Moreover, yoke laminations are generally shuffled during the magnet assembly, and lamination-to-lamination differences are smoothed. The values of the initial magnetization curve are very similar to specimen B of the pre-production, but the hysteresis shape is significantly different. In particular, the hysteresis shape is very similar to the one of specimen A, but with a much lower coercive field value; this is because the material was not annealed and hot-rolled at a higher temperature, thus determining a positive effect of stress relief.

3.7   Problem statement and motivations for characterization at high fields

The increasing level of the magnetic field generated by the new magnets of the HL-LHC determines heavily saturated regions in their iron yokes, as shown in Fig. 3.12, where the flux density around the aperture reaches a value ranging from 3 to 4 T. To accurately predict the magnet behavior, it is necessary to characterize the yoke magnetic properties up to a flux density of 3 T and measure the full saturation region. Fig. 3.13 highlights how the saturation region impacts the field quality, showing the influence of different magnetization curves on the MBH 11 T dipole transfer function. It is worth noticing how the impact of the magnetization curves is

negligible in the low-field region, and the three transfer functions match despite the different yoke behaviors, thus confirming what was previously illustrated in Sec. 1.3 and Sec. 3.6.
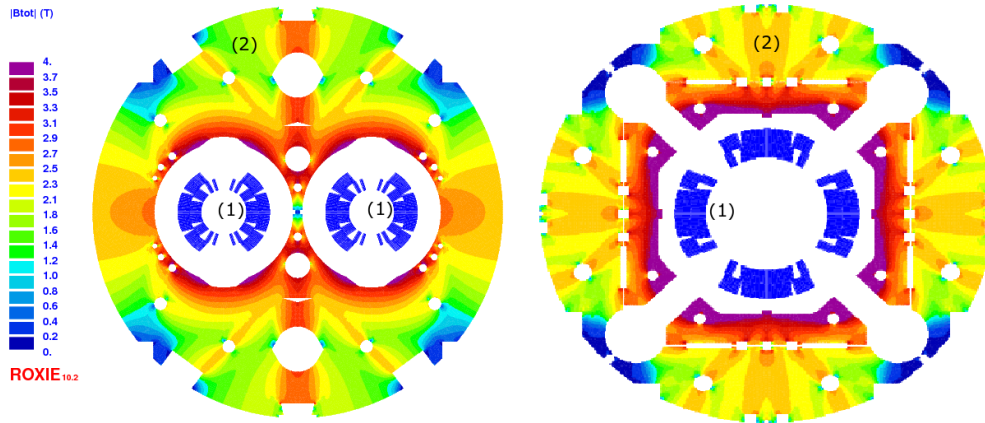
Fig. 3.12 FE simulations of the MBH 11 T dipole (left) and the MQXF inner triplet quadrupole (right). (1) Superconducting windings; (2) Iron yoke (© 2019 IEEE).
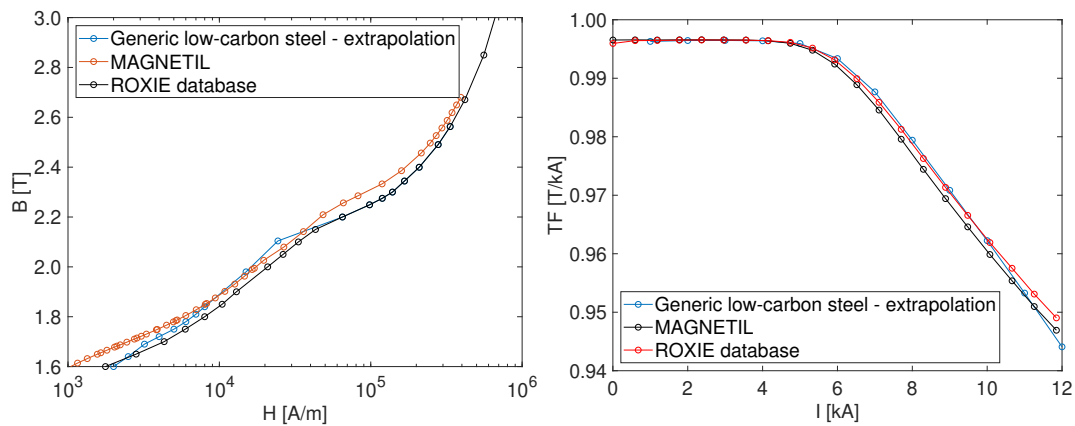
Fig. 3.13 (Left) Some initial magnetization curves in their saturation region; (right) corresponding transfer functions for the MBH 11 T magnets for the HL-LHC [courtesy of S.I. Bermudez].

Data at flux densities values higher than 2 T can be obtained using data from similar materials or by extrapolating the saturation region from lower field values. However, this second approach determines the least accurate outcome if the material has not fully saturated yet, which is often the case with low-carbon steels. Another

motivation is that data for ARMCO® Pure Iron up to a 3 T flux density, at 4.2 K, are not available in the literature.

Ring permeameters generally perform measurements up to a 2 T flux density at magnetic fields up to 25-50 kA/m because components such as electrical motors or magnets are usually designed by optimizing the iron core geometry to make it work around the peak permeability region and minimize the iron core volume. An example of flux density distribution in the iron core of a motor is shown in [4]. However, a measurement of flux densities up to 2.5-3 T requires an increase of the magnetic field by a factor of 10. This increase of magnetic field can be achieved by increasing the excitation current, the number of excitation turns, or a combination of the two. As shown in Sec. 4.1, where the design criteria are presented, the solution chosen in this dissertation is to develop a permeameter based on superconducting coil technology to remove the constraints of increasing the coil-cross section and allocate a higher number of turns. This approach has already been used in the past to characterize data at high fields. For example, in [149] this approach was used for the 10 T superconducting dipoles developed at the National Laboratory for High Energy Physics in Japan (KEK). In [59, 146], MAGNETIL® was measured up to 2.6 T. These works do not provide enough detail on the experimental setup and do not describe how the system was designed and how quench events are handled. Moreover, data measured in the saturation region may lack accuracy. Normally, the characterization of soft ferromagnetic steels is done at low fields, where the contribution of the sensing coil area calibration is negligible because the magnetic flux is confined only to the test specimen volume. Therefore, the sensing coil area is calculated from the geometry to compensate for the small air-flux contribution, or it is not calculated at all, and the air flux is considered negligible. For instance, the IEC standard reports both approaches [94]. Nonetheless, if the coil geometric area is used, a correction factor has to be applied to take into account the thermal contraction. This problem has been addressed by proposing an approach for *in-situ* calibration. Finally, guidelines are provided in the next Chapter to perform tests at cryogenic temperatures accurately.

Chapter 4

Proposal

In this Chapter, a superconducting permeameter is proposed to address the need for experimental data at high-fields and cryogenic temperature of ARMCO® Pure Iron, the yoke material of the new HL-LHC magnets. The system consists of a ring-wound permeameter with the excitation coil made of more than 3000-turns of NbTi superconducting wire to overcome the limitations of using a copper excitation coil, mainly space and electrical resistance. The design steps, the implementation, and the metrological model are presented. This work was done in collaboration with A. Parrella, who collaborated in the early development stage, and E. Stubberud, who performed the quench simulation analysis. Part of the content presented in this Chapter was previously published also in [P2, P8].

4.1 Superconducting permeameter design

4.1.1 Design criteria

The goal of the superconducting permeameter is to measure the magnetic properties of low-carbon steels such as ARMCO® up to magnetic flux densities greater than 2.5 T, at 4.2 K. Magnetic fields higher than 240-250 kA/m are necessary to achieve such flux density values. In the following, the design choices will be presented using as a reference the geometry parameters shown Sec. 3.2, a toroid having an outer diameter of 114 mm and an inner diameter of 76 mm. The specimen thickness can be ignored in this phase.

Two possible alternatives can be chosen to increase the magnetic field: increasing the excitation current or the number of excitation turns. A combination of both is another viable solution.

Increasing the excitation current is a viable solution, provided the availability of a suitable power supply. For example, using 180 turns, a current of about 400 A would be necessary to obtain 240 kA/m. The cross-section of the current leads and the cables carrying the current to the cryostat, at 293 K, would be not higher than 185 mm^2. Nevertheless, this value is calculated for a DC current of 400 A. Given the typical current cycles used for material characterization, the RMS value of the current would be certainly lower, and lower cross-sections can be used for the warm part (*e.g.* 35 mm^2, 120 A RMS, 650 s of cycle duration in a current ranging from 2.5 A to 380 A). Inside the cryostat, the cross-section of the excitation turns shall be of at least 1.5 mm^2 if copper is chosen.

The other alternative is to increase the number of excitation turns and keep the current constant. For example, using a current of 40 A, the number of excitation turns necessary would be 1800. The higher number of excitation turns determines an increase in electrical resistance and inductance. The inductance increases with the square of the number of turns. The electrical resistance increases linearly with the number of turns in a first-order approximation. For example, if a copper wire of 0.5 mm diameter were used, the total coil resistance would be about 16 Ω at 293 K, thus 0.53 Ω at 4.2 K (adopting a residual resistance ratio of 30 [150]). Considering that the system is immersed in the helium bath, thermal considerations should also be taken into account because the excitation coils would dissipate 848 W, thus accelerating the helium evaporation and reducing the time available to carry out the measurement campaign. However, this last problem can be addressed by increasing the cross-section of the coil, on the condition of seeking a trade-off between the number of turns and the space necessary to allocate the turns, or by adopting superconducting coil technology.

In this dissertation, the proposed solution is to allocate as many turns as possible on the specimen and adopt NbTi superconducting coil technology to have negligible electrical resistance. This choice is motivated by the necessity of keeping the cost low and exploiting the already available hardware, without need to increase the cross-sections of cables and current leads. For instance, the available power supply can only generate up to 40 A and 15 V, thus limiting the load resistance to a maximum of 0.375 Ω. In truth, the limit is lower because the specimen inductance reduces the

load margins requiring an additional voltage contribution when the current is ramped up and down.

4.1.2 Superconducting permeameter layout

The superconducting permeameter layout is shown in Fig. 4.1.
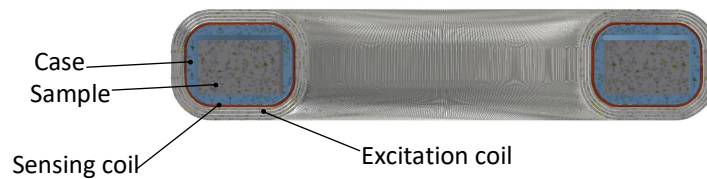
Fig. 4.1 Superconducting permeameter layout. (© 2019 IEEE)

The superconducting permeameter is a wound permeameter, with the coils uniformly spaced in accordance with the guidelines provided by the standard IEC 60404-4 [94]. Two prototypes were produced. The first one was used to measure ARMCO® specimen B from Sec. 3.2 to validate the design. The second one was used to measure a different ARMCO® specimen, from the production batch.

4.1.3 Holder

The specimen holder is made of Accura® Bluestone to prevent mechanical strain on the sensing coil due to thermal contraction when the system operates in the helium bath. The holder is 3D printed, and it was designed to host a specimen with a squared cross-section. The outer shape has round corners to avoid sharp edges that could damage the sensing coil. The holder's material was chosen among other alternatives, such as the Nylon Glass Fiber used to prepare the specimen measured in Sec. 3.3, because of its thermal contraction coefficient, about 6 mm/m of variation at 4.2 K from 293 K, which is lower than other plastics and comparable with stainless steel. The choice of using Bluestone was originally intended to preserve the sensing coil area when cooling down the specimen to 4.2 K, because the geometric area would have been used. However, given the *in-situ* calibration procedure presented in Sec.4.2, the holder material is not relevant. Fig. 4.2 shows examples of contraction coefficients from 293 K.

Plastics thermal contraction comparison VD 5.08.13
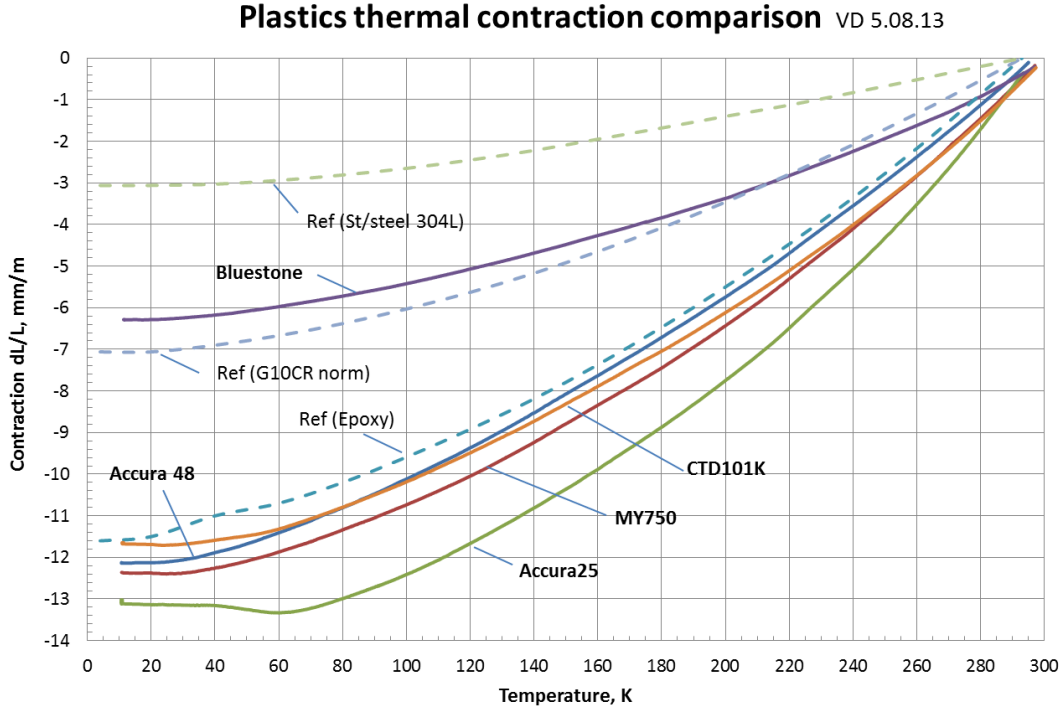
Fig. 4.2 Selection of plastics and their corresponding thermal contraction curves [151].

4.1.4 Superconducting excitation coil

The superconducting excitation coil consists of a multi-turn winding, with its turns uniformly distributed on multiple layers, each one separated from the next by a layer of Kapton tape to prevent movement. The superconducting wire is manufactured by Furukawa Electric Co. and has a diameter of 0.5 mm. The parameters of the wire are reported in Fig. 4.3, highlighted in red.

The minimum available diameter of 0.5 mm was chosen because it guarantees operation margins. The declared minimum critical current at a 5 T field is 160 A. Using the critical surface model proposed in [16, 153], the critical current density can be expressed as a function of the field and the temperature as

$$J_c(B,T) = \frac{J_c^{ref} C_0 B^{\alpha-1}}{B_{c2}^{\alpha}} (1-b)^{\beta} (1-t^{1.7})^{\gamma}, \tag{4.1}$$

where J_c^{ref} is a reference critical current density, B_{c20} the upper critical field at $T = 0$ K, T_{c0} the critical temperature at zero field, C_0, α, β, γ model parameters. Moreover,

Specifications for NbTi Round Wire · F830/2.0 series

Furukawa Electric Co., Ltd.
Spec. No. SCH-1114D
November 14, 2014

Type		F830/2.0/50	F830/2.0/65	F830/2.0/75	F830/2.0/85	F830/2.0/100
Superconductor		Nb-47±1wt%Ti	Nb-47±1wt%Ti	Nb-47±1wt%Ti	Nb-47±1wt%Ti	Nb-47±1wt%Ti
Bare Wire Diameter	(mm)	0.50 ± 0.01	0.65 ± 0.01	0.75 ± 0.01	0.85 ± 0.01	1.00 ± 0.01
Filaments						
- Mean Diameter (nominal)	(μm)	10.0	13.0	15.0	17.0	20.0
- Number of Filaments (nominal)		830	830	830	830	830
- Twist Pitch	(mm)	12 ± 2	15 ± 2	18 ± 2	19 ± 2	20 ± 2
- Twist Direction *1)		S	S	S	S	S
Matrix		Oxygen Free Copper	Oxygen Free Copper	Oxygen Free Copper	Oxygen Free Copper	Oxygen Free Copper
Cu to Superconductor Ratio		2.0 ± 0.2	2.0 ± 0.2	2.0 ± 0.2	2.0 ± 0.2	2.0 ± 0.2
Insulation						
- Material		Polyvinyl Formvar	Polyvinyl Formvar	Polyvinyl Formvar	Polyvinyl Formvar	Polyvinyl Formvar
- Breakdown Voltage	(Vac)	> 2,000	> 2,000	> 2,000	> 2,000	> 2,000
- Insulated Diameter	(mm)	0.55 ± 0.02	0.70 ± 0.02	0.80 ± 0.02	0.90 ± 0.02	1.05 ± 0.02
Minimum Critical Currents at 4.2K and 10⁻¹³Ωm						
- Ic at 5T	(A)	> 160	> 280	> 370	> 475	> 660
- Ic at 6T	(A)	> 130	> 220	> 290	> 370	> 520
- Ic at 7T	(A)	> 100	> 170	> 220	> 280	> 400
Minimum RRR		> 100	> 100	> 100	> 100	> 100
Minimum Piece Length	(m)	5,000	5,000	3,000	3,000	3,000
Number of Piece		≦ W/50	≦ W/50	≦ W/50	≦ W/50	≦ W/50
Total weight	(kg)	W (TBD)	W (TBD)	W (TBD)	W (TBD)	W (TBD)
Length (nominal)	(m)	TBD	TBD	TBD	TBD	TBD

[Notes]
*1) Twist Direction "S" means the left hand screw twist.

Fig. 4.3 Superconducting strand specifications from Furukawa Electric Co. Ltd [152].

$$t = \frac{T}{T_c0}, \tag{4.2}$$

and

$$b = B/B_{c2}(T). \tag{4.3}$$

The critical field scales with temperature as

$$B_{c2} = B_{c20}(1 - t^{1.7}). \tag{4.4}$$

Using a $J_c^{ref} = I_c/A_w = 8.15 \times 10^8$ A/m^2 at 4.2 K and 5 T, $B_{c0} = 14.5$ T, $T_{c0} = 9.2$ K, $C_0 = 27.04$ T, $\alpha = 0.57$, $\beta = 0.9$, and $\gamma = 2.32$, Fig. 4.4 shows the critical current for the chosen strand as a function of the field. A_w is the cross-section area of the wire.
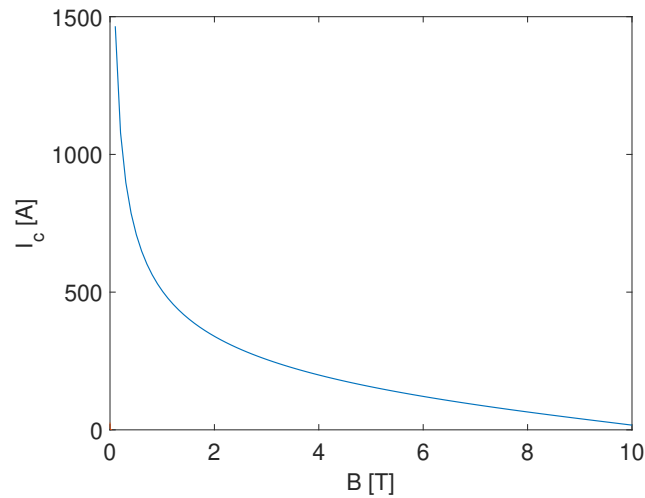
Fig. 4.4 Critical current as a function of the field for the highlighted in Fig. 4.3, at an operation temperature of 4.2 K.

Given the field values reported in Tab. 4.1, the current shall be limited to the critical value in correspondence with the field at the innermost layer. Therefore, I_c ranges from 324 A to 666 A, and $B_{c2} = 10.68$ T. Since the maximum excitation current will be 40 A, the NbTi wire will be used well below its operation limits. The last quantity to evaluate is the magnetization of the superconducting excitation coil. From a phenomenological point of view, when a magnetic field is applied to a superconductor, eddy currents are induced on its surface, preventing the field from penetrating the superconductor volume. According to Wilson's model for a cylindrical filament [16, 38], these currents are confined into two semi-shells, with a current density of J_c and $-J_c$ respectively, as shown in Fig. 4.5 (left).
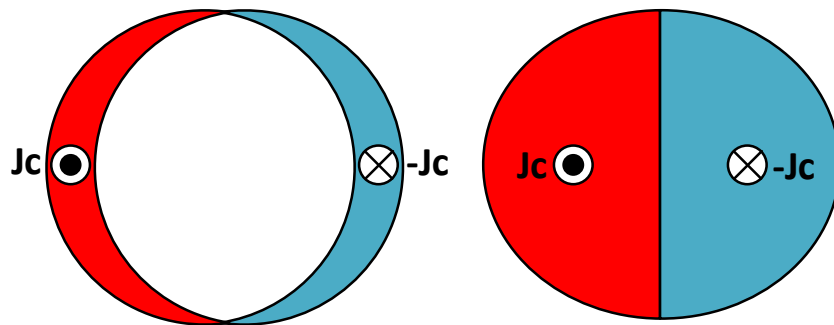
Fig. 4.5 Current density distribution inside a cylindrical filament when the field is not totally penetred (left), and when it is totally penetred (right).

When the field is increased above a level B_p, called *penetration field*, the field penetrates the filament volume, and the distribution becomes as shown in Fig. 4.5 (right). When the field is reduced, the polarity of the currents is reversed, and an additional layer of screening currents is induced on the surface. When the field is increased back to B_p again, the additional layer wipes out the previous one. These screening currents can be modeled as a magnetization $M_f(B)$, displaying hysteretic behavior because the values of M_f depend on its past-history values.

According to Wilson's model, the value of B_p is

$$B_p = \frac{2\mu_0 J_c r_f}{\pi}. \tag{4.5}$$

where r_f is the radius of the superconducting filament. The wire chosen to carry out the measurement campaign is made of 830 filaments having $r_f =$5 μm. J_c=3.40$\times10^9$ A/m^2, if a maximum current of 40 A is adopted and the wire is exposed to a field of B=0.57 T (see Sec. 4.1.5). Therefore, B_p=13.6 mT and the field penetrates the coil volume. The magnetization of a filament M_f can be computed from the critical current density as a function of the applied field using the following formula from [38]:

$$M_f = -\frac{4}{3\pi} J_c r_f. \tag{4.6}$$

The magnetization of the entire wire M_s can be calculated as

$$M_s = \lambda M_f, \tag{4.7}$$

where λ is the filling factor. In detail,

$$\lambda = \frac{1}{1 + \lambda_{Cu-Su}}, \tag{4.8}$$

where λ_{Cu-Su} is the copper-to-superconductor ratio. From Fig. 4.3, $\lambda = 1/3$. From Eq. 4.6, it is clear that one can reduce the impact of the superconductor magnetization by reducing the filament radius and adopting multi-filament wires/cables.

Using the current density distribution J_c calculated from Eq. 4.1, one can compute the hysteresis loop using Eq. 4.7. The result is shown in Fig. 4.6. The model is an approximation and differs significantly from experimental data around $B =$0, where the superconductor magnetization has a peak around $B = -0.1$ T [16]. The super-

conductor hysteresis presented in this Section is not the only contribution. Similarly to ferromagnetic materials, when ramping the field, dynamic effects determine a widening of the hysteresis loop [16]. However, a description of dynamic effects is beyond the scopes of the dissertation and, therefore, they will not be considered. Only the DC magnetization values from 4.6 will be used to assess the impact of the superconductor magnetization in terms of measurement uncertainty in Sec. 4.4.5.
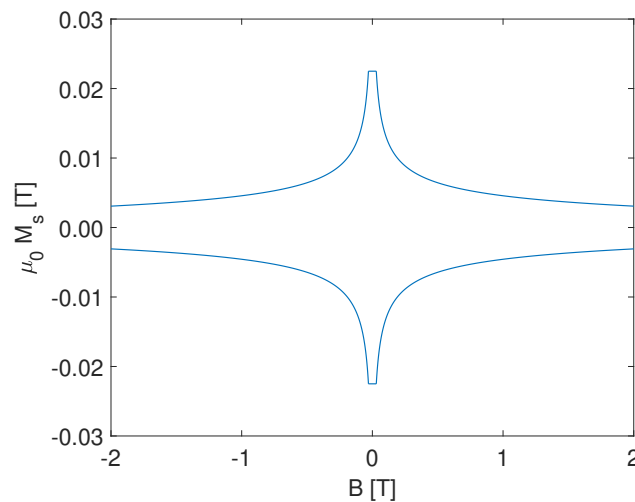
Fig. 4.6 Calculated hysteresis loop for the superconducting wire of Fig. 4.3.

4.1.5   Quench simulation and system protection

When a superconducting system is designed, particular attention is dedicated to the quench events, namely a loss of superconductivity that occurs when a superconductor operates outside its operating margins. This loss of superconductivity becomes a source of heat dissipation, can compromise the system's integrity, and can be dangerous in operation because the helium's boil-off can increase the pressure inside the cryostat. Therefore, an analysis has to be carried out to verify if the operation currents are safe in operation by calculating the hotspot temperature and assessing if a quench detection system is needed.

The protection study was carried out at three values of the current, 40 A, 80 A, and 150 A, at a temperature of 4.2 K, and considering 2557 excitation turns split in four layers, evaluated from the rendering in Fig. 4.1. The study consisted of different steps, and different software tools were used. The specimen geometry was assumed to be a toroid of 114 mm outer diameter, a 76 mm inner diameter,

and 12 mm thickness. A first FE model implemented in COMSOL® was used to evaluate the operation flux density B and the inductance L of the coil. In this model, the coil's shape was simplified by modeling it as a single conductor with thickness proportional to the inverse of the toroid's radius, similarly to how the thickness of the winding scales with the radius. The elements are summarized in Fig. 4.7. The values of the inductance and magnetic flux density are reported in Tab. 4.1.
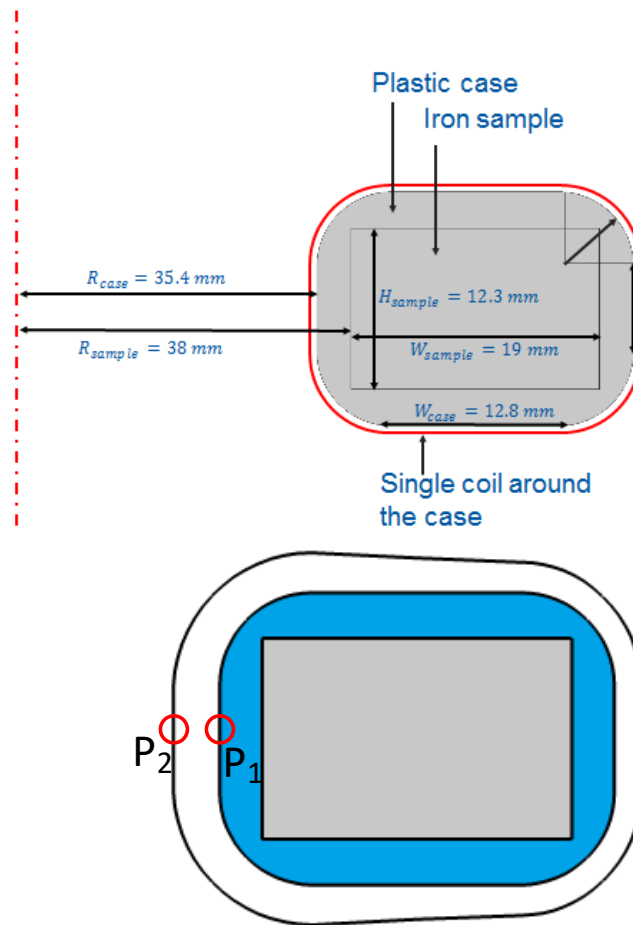
Fig. 4.7 Geometry of the FE model (top) and, winding shape and; (bottom) point where the flux density was evaluated (© 2019 IEEE).

The quench simulations were performed by using a software tool developed at the Laboratory for Accelerators and Applied Superconductivity (LASA) of the Instituto Nazionale di Fisica Nucleare (INFN), called QLASA [154, 155], coupled with a PSpice circuit.
QLASA is a software tool to perform quench thermal propagation analysis in straight superconducting solenoids. As the tool works only with straight geometries, the

Table 4.1 Magnetic flux density and inductance values for each current level.

Current I	Inductance L	$B(P_1)$	$B(P_2)$
40 A	45.92 mH	0.5733 T	4 mT
80 A	29.71 mH	1.1466 T	8 mT
150 A	22.13 mH	2.1500 T	14.9 mT

simulation was performed on a solenoid, having a length equal to the innermost circumference of the toroid. The coil cross-section was assumed to be equal to the innermost cross-section of the windings in the r-θ plane. Finally, to take into account that the field scales with the radius of the toroid, the field was assumed constant in the solenoid volume and equal to its values in P_1 and P_2 outside, to achieve conservative results.

Toroidal shape   Solenoidal shape
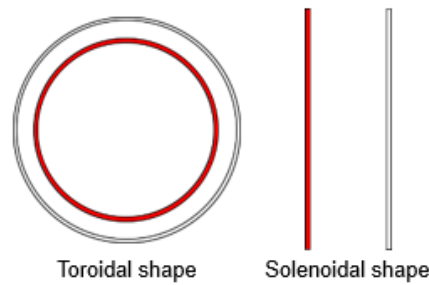
Fig. 4.8 Transformation step of the toroidal geometry into a straight geometry [courtesy of E. Stubberud].

The thermal analysis was performed in adiabatic conditions, thus assuming no heat transfer from the coil to the surrounding helium. The adiabatic conditions were assumed because the turns are isolated from the helium bath, and the typical dynamics of quench events are fast, in the order of 100 ms.
The output of the thermal model was provided as input to a circuital model, having the same parameter of the experimental setup. The circuit is shown in Fig. 4.9.

The power supply is modeled as a current generator. The superconducting permeameter is represented by an R-L load, with the resistive element $r(t)$ that varies over time during a quench. In normal conditions, it can be assumed to zero. During a quench, $r(t)$ suddenly increases. As a protection element, a diode represented by a crowbar in series with a resistance R_D of 1 mΩ was used. In this way, when $r(t)$ increases as a result of a quench event, the voltage drop increases. When the voltage
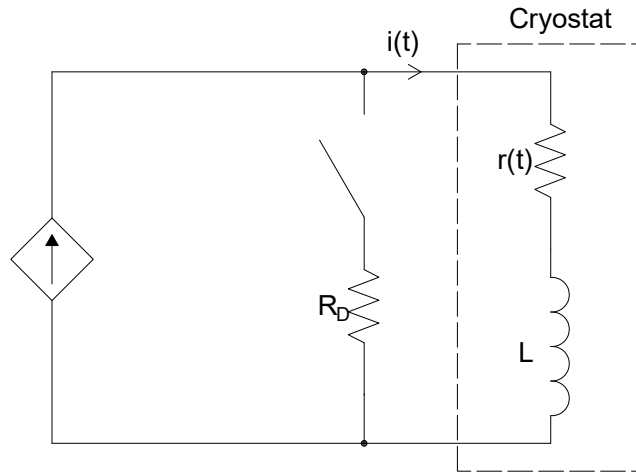
Fig. 4.9 Electrical model of the quench simulation (bottom).

reaches a threshold value, set to 1 V, the power supply turns off, and the crowbar
switches off. Fig. 4.10 shows the results of the quench event simulations.

The hotspot temperature increases as the current increases, but it remains well
below 100 K in all cases. In conclusion, the simulations show that the system is
self-protected in all three cases.
The voltage threshold limits the time derivative of the current in the coil. If V_t is the
voltage threshold level,

$$\left(\frac{di}{dt}\right)_{max} = \frac{V_t}{L}. \tag{4.9}$$

The threshold voltage limits the ramp rate of the current to 21.7 A/s at 40 A,
33.7 A/s at 80 A, and 44.2 A/s at 150 A. The maximum operation current was kept
at 40 A, and the ramp rate limits are well below the maximum rate allowed by the
power supply (10 A/s).

4.2 Guidelines for the characterization of soft ferro-magnetic materials at cryogenic temperatures

Characterizing a soft magnetic material at cryogenic temperatures lies upon the same
principle of room temperature characterization. However, some aspects should be
taken into account to avoid introducing deterministic errors in the measurement

(a) Current

(b) Voltage

(c) Resistance

(d) Hotspot temperature
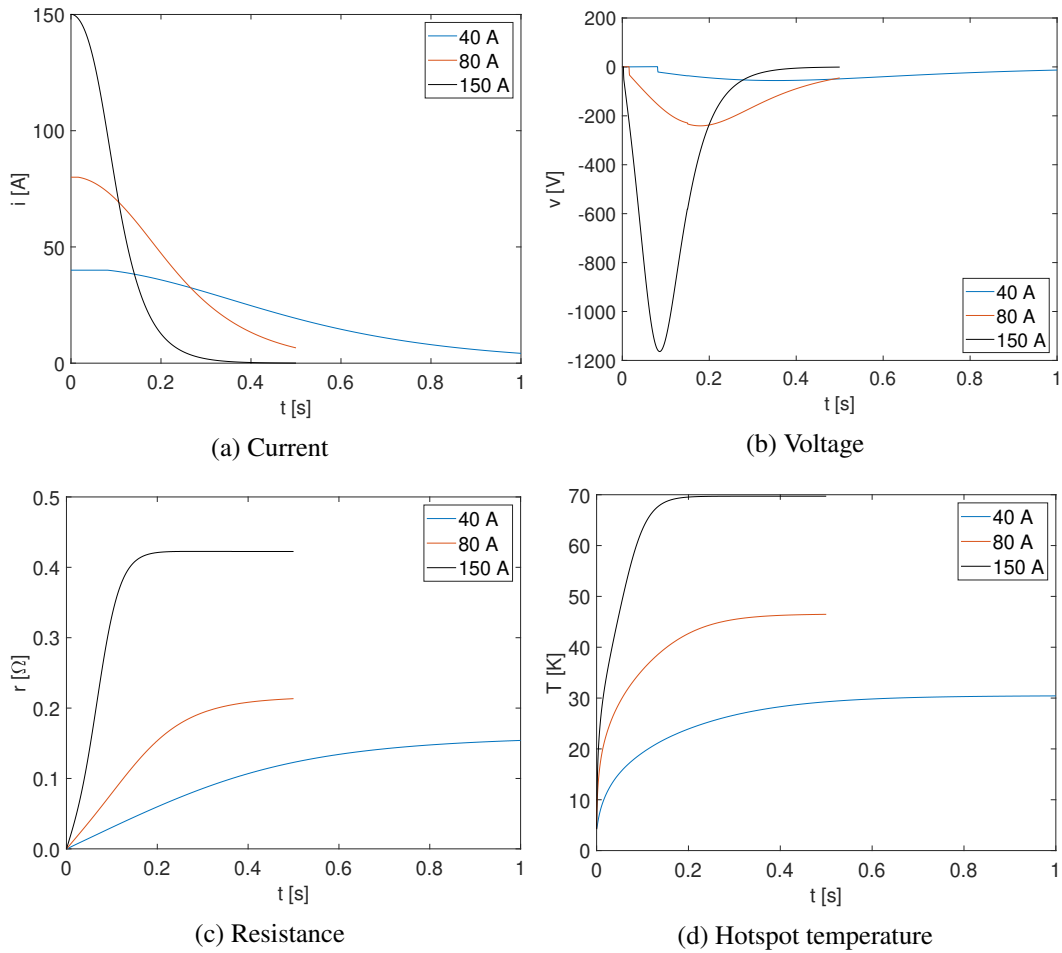
Fig. 4.10 Evolution of current, voltage, resistance and hotspot temperature after a quench event [courtesy of E. Stubberud].

results. As the concern is the characterization of soft ferromagnetic materials, the following guidelines are referred to measurements performed by flux-metric method in the transformer configuration.

4.2.1 Eddy currents

The main difficulty when measuring a material at cryogenic temperature is that the conductivity of the material under test increases, first linearly down to about 20-30 K, and then the conductivity saturates at a residual value. In the literature, the ratio between the resistivity at 300 K and the one at 0 K, is called Residual Resistance Ratio (*RRR*) and is defined as

$$RRR = \frac{\rho_{300\ K}}{\rho_{0\ K}} \qquad (4.10)$$

where $\rho = 1/\sigma$ is the resistivity of the material. The *RRR* ranges between 30 and 250 for pure iron [156]. This increase of conductivity results in an increase of the eddy currents' amplitude circulating in the material. On the other hand, the decrease of the differential permeability slightly limits the increase of the eddy currents' amplitude. As a conventional test procedure, the standard IEC 60404-4 prescribes, when adopting the continuous recording method, a ramp duration of 60 s, or 120 s if the material is pure iron, from 0 to the maximum field, as illustrated in Sec. 2.2. This means that when the temperature decreases, the ramp duration should theoretically scale accordingly with the *RRR*. Nonetheless, accurate measurement of the DC hysteresis cannot even be performed at room temperature on materials such as pure iron by continuous recording method, because it is intrinsically a dynamic method and the coercive field H_c might result overestimated.
Fig. 4.11 shows for specimen B of Sec. 3.2 how these eddy currents impact at three different temperatures, 293 K, 77 K, and 4.2 K, when the hysteresis is measured by continuous recording method. The DC hysteresis, measured by point-by-point method is plotted for comparison to visually highlight the estimation error.

The ramp rate values corresponding to a ramp duration between 40 s and 90 s lie between 807 Am^{-1}s^{-1} and 403 Am^{-1}s^{-1}. At room temperature, the coercive field is overestimated of a factor from 1.5 to 2 when using the continuous recording method. At 77 K, the overestimation is of factor from 2.5 to 3.5. At 4.2 K, from 4 to 5. In conclusion, the continuous recording method shall be avoided when measuring at cryogenic temperatures, and the hysteresis should always be measured using the point-by-point method.
The same principle also applies when measuring the initial magnetization curve by using the point-by-point method, where higher plateau durations shall be used at cryogenic temperatures. At 4.2 K, a plateau duration of 60 s was conservatively used in the peak permeability region.

4.2.2   Thermal contraction

The second issue when measuring a material at cryogenic temperature is that the material thermal contraction should be considered to avoid underestimating the flux

(a) Room temperature

(b) Liquid nitrogen temperature

(c) Liquid helium temperature
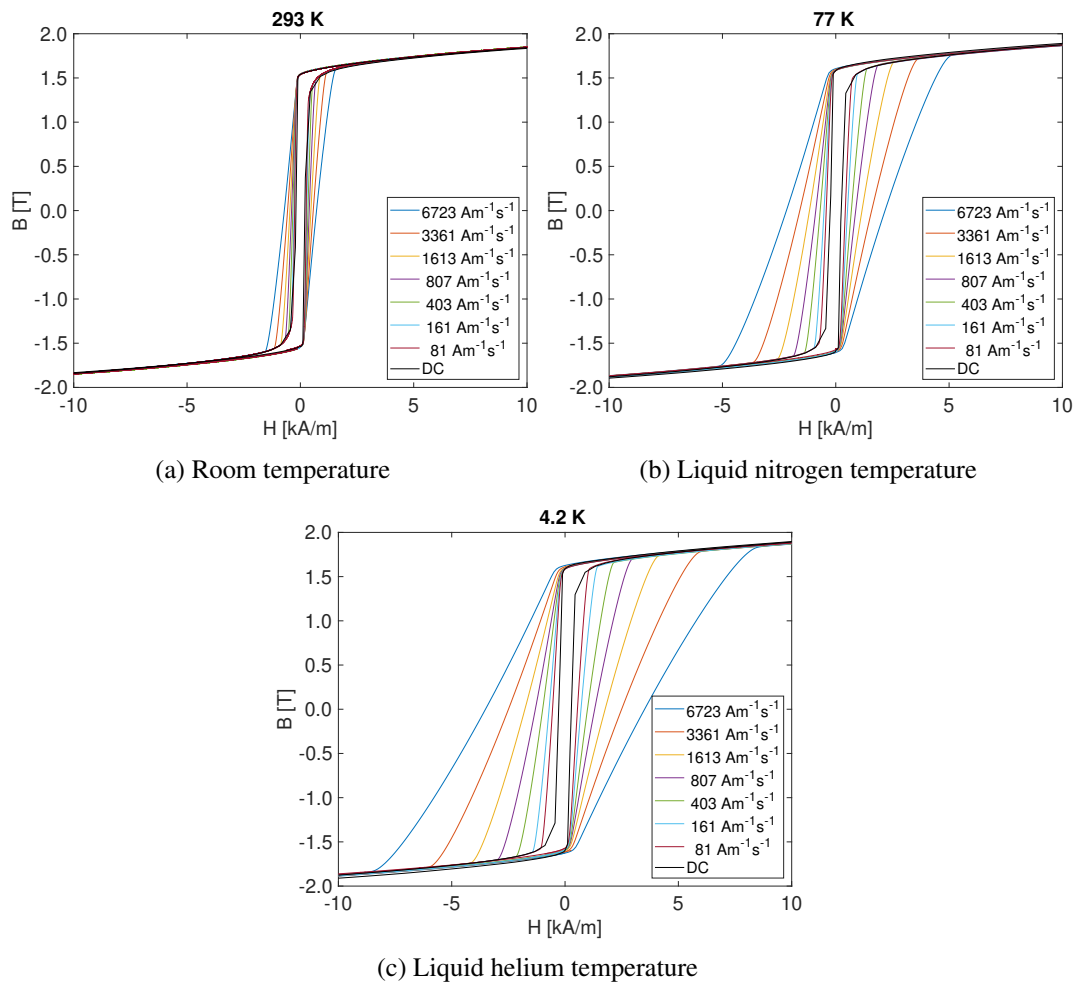
Fig. 4.11 Hysteresis loops of ARMCO specimen B from Sec.3.2, measured at different ramp rate values and different test temperatures.

density values. This issue can be addressed by applying a correction factor to the specimen dimensions when post-processing the data. The value of the correction factor depends upon the test temperature, and for metals such as pure iron or stainless steel, it can range between 2 ‰ and 3 ‰ at 4.2 K (see also Fig. 4.2).

4.2.3   Sensing coil area calibration

Sensing coil area calibration is another crucial aspect to be addressed when measuring a toroidal specimen at cryogenic temperatures. If the impact of the coil area is negligible at low field values, well below 10 kA/m, this progressively increases as

the excitation field increases due to the increasing term in Eq. 2.12, depending on H, and describing the air-flux compensation. Considering that the full saturation region needs to be measured, thus at field values above 50 kA/m, the impact of this coil area can be in the order of a few percent.

At room temperature, the sensing coil area can be calibrated using Eq. 2.18, when using a split-coil permeameter due to the possibility of closing the coils and directly measuring the air flux. If this is not possible, the IEC standard 60404-4 proposes using a reference standard coil mutually coupled with the toroidal specimen to compensate for the air flux.

Three possible alternatives are presented in the following. The first and most basic option is to assume the sensing coil area as equal to the geometric cross-section area of the specimen holder on the condition that the sensing coil is the innermost coil layer, which is often the case in many experimental setups. In this way, it is only necessary to apply a correction factor to consider the holder's thermal contraction (see Fig. 4.2). However, deviations up to 10 % were observed between the holder cross-section area and the effective coil area, impacting with deviations up to 10 % in the saturation region.

A second approach could be to wind the same number of excitation and sensing turns on an identical specimen holder, power the excitation coil, and calculate the sensing coil area as:

$$A_t = \frac{\Phi}{\mu_0 N_t H}. \tag{4.11}$$

This solution can be easily implemented in split-coil systems, such as the one used to perform the experiments presented in Chap. 3. However, realizing a dual system with thousands of superconducting excitation turns identical to the one containing the specimen is too expensive, given the high cost of superconductors, and time-demanding.

A new approach for calibration is proposed in this dissertation and was used to obtain the experimental results presented in Chap. 5. The method consists of performing the calibration in the saturation region, where the behavior of the material is known. In particular, when the material is fully saturated, the following relation holds:

$$\frac{dB}{dH} = \mu_0. \tag{4.12}$$

Hence, by ramping the specimen at a conveniently high field, *e.g.*, 50 kA/m, imposing Eq. 4.12 and using Eq. 2.12, the sensing coil area can be calculated as:

$$A_t = \frac{1}{\mu_0 N_t} \frac{d\Phi}{dH}. \tag{4.13}$$

The method can be generalized and used in the approach-to-saturation region at magnetic fields greater than 10 kA/m, and *B* between 1.8 and 2 T. In this case, Eq. 4.12 and Eq. 4.13 can be modified using the value of the average differential permeability in the region where the analysis is performed. Since the differential permeability is independent of the test temperature, and the magnetization curves remain parallel, the value to impose can be derived from a measurement at room temperature performed using a system already calibrated.

4.3   Acquisition hardware and measurement system setup

The experimental setup is based on the one used for flux-metric methods, already shown in Fig. 2.2, but with some modifications, as shown in Fig. 4.12.
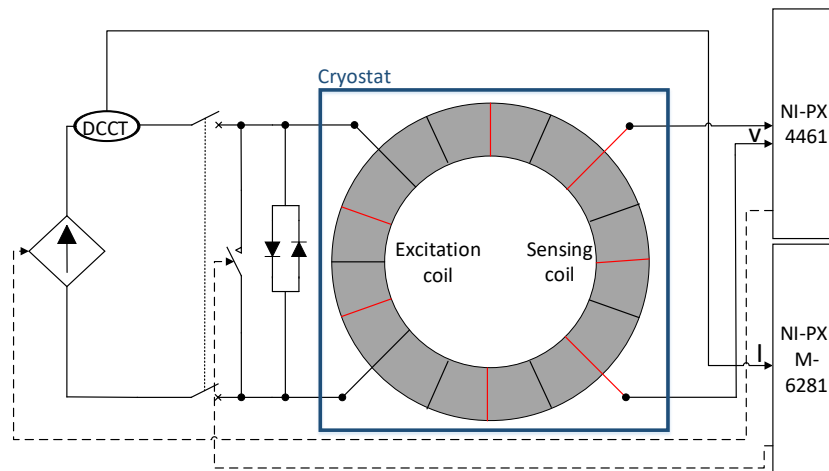
Fig. 4.12 Measurement system layout. The area delimited in the blue box is operated at 4.2 K.

The measurements were performed using a current-controlled power supply, whose reference voltage is supplied by an analog signal generated by a Digital-

to-Analog Converter (DAC). The current is measured with a DC Transformer (DCCT) installed on the primary excitation coil. The induced voltage is measured across the terminal of the secondary coil. Current and voltage are continuously recorded during the measurement process. The induced voltage is measured by a commercial Dynamic Signal Acquisition device NI-PXI 4461 [157], equipped with two independent 24-bit Σ-Δ Analog-to-Digital Converter (ADC). The same board is equipped with two DAC channels, one of which was used to generate the reference voltage for the power supply. The main parameters are summarized in Tab. 4.2. A second commercial general-purpose NI-PXI M-6281 [158] is used to measure the excitation current. The M-6281 also is used to provide a digital signal to a contactor, connected in parallel with the load. This contactor is used to short-circuit the load at the beginning of the generation process because the intrinsic high-pass nature of the NI-PXI 4461 determines an overshoot on the first 90 generated samples, which might create problems with the power supply internal control algorithm. The main parameters are summarized in Tab. 4.3.

Table 4.2 Specifications of the NI DAQ 4461

Parameter	
Analog input (AI) resolution	24 bit
Maximum AI range	$\pm$ 31.6 V
Minimum AI range	$\pm$ 0.316 V
Max. Sample rate	204.8 kS/s
Analog output (AO) resolution	24 bit
Maximum AO range	$\pm$ 10 V
Minimum AO range	$\pm$ 0.1 V

Table 4.3 Specifications of the NI DAQ M-6281

Parameter	
Analog input (AI) resolution	18 bit
Maximum AI range	$\pm$ 10 V
Minimum AI range	$\pm$ 0.1 V
Max. Sample rate	625 kS/s

The quench detection was implemented by installing two power diodes in anti-parallel. In normal operation conditions, the diodes are not in conduction because the load voltage is lower than their threshold voltage. In case of a quench event, the voltage increases abruptly and one the diodes starts to conduce, short-circuiting

the system. The quench event can be visually identified by the operator performing the measurement, blocking the power supply. The chosen diode model is a STTH200W06TV1, produced by STMicroelectronics [159], with a threshold voltage of 1 V and forward RMS current of 145 A. This model has two diodes mounted in the same packaging.

Finally, a rheostat was added in series with the measurement system to avoid instability of the power supply control system, working only on loads with non-zero resistance.

Data were post-processed online by using the Flexible Framework for Magnetic Measurements (FFMM), a suite of interactive programs [160] written in $C++$ to perform magnetic measurements by adopting a high-level approach based on object-oriented programming.

4.4 Uncertainty assessment

4.4.1 Summary of the uncertainty sources

The uncertainty assessment was performed by adopting the International Organization for Standardization (ISO)-Guide to the Expression of Uncertainty in Measurement (GUM) approach [161]. The sources of uncertainty are summarized in Fig. 4.13. Their values are reported in Chap. 5, where the experimental results are presented.

4.4.2 Propagation of the uncertainties

The uncertainty of the magnetic field at the time instant k, $u(H_k)$, can be derived from Eq. 2.16, thus yielding

$$u(H_k) = \sqrt{\left(\frac{N_e}{2\pi r_0}\right)^2 u^2(I_k) + \left(\frac{N_e I_k}{2\pi r_0^2}\right)^2 u^2(r_0)}, \qquad (4.14)$$

where
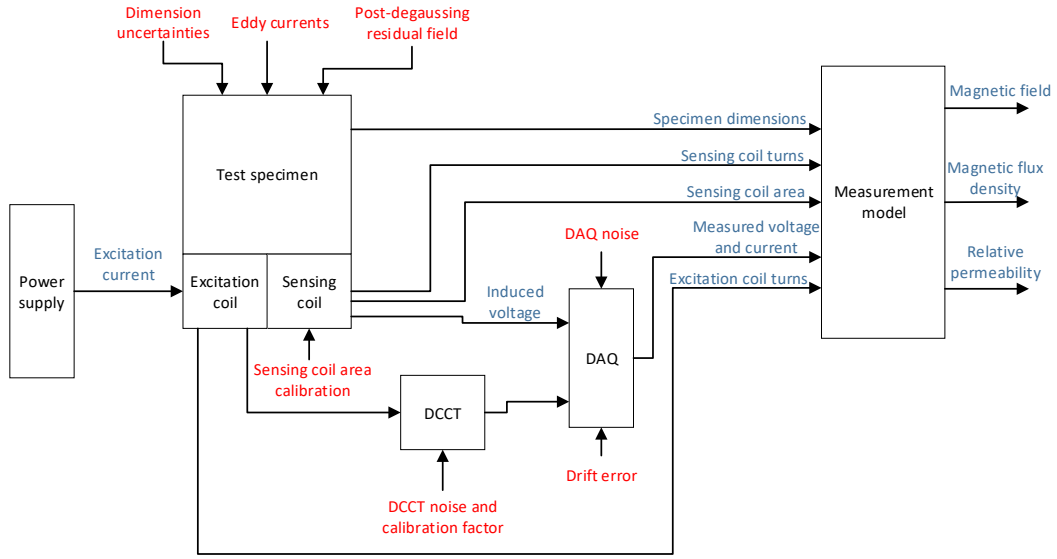
Fig. 4.13 Summary of the uncertainty sources of the superconducting permeameter. In blue) the measurement parameters with their uncertainty and; in red) the uncertainty sources.

$$u(r_0) = \frac{1}{\ln(\frac{r_2}{r_1})} \sqrt{\left(1 - \frac{r_2 - r_1}{r_2 \ln(\frac{r_2}{r_1})}\right)^2 u^2(r_2) + \left(\frac{r_2 - r_1}{r_1 \ln(\frac{r_2}{r_1})} - 1\right)^2 u^2(r_1)}, \quad (4.15)$$

and it is derived from Eq. 2.17.

The uncertainty of the magnetic flux density at the time instant k, $u(B_k)$, can be derived from Eq. 2.12, thus yielding:

$$u(B_k) = \left[\left(\frac{1}{A_s N_t}\right)^2 u^2(\Phi_k) + \left(\frac{\mu_0(A_t - As)}{A_s}\right)^2 u^2(H_k) + \left(\frac{\mu_0 H_k}{A_s}\right)^2 u^2(A_t) + \right.$$
$$\left. + \frac{1}{A_s^4}\left(\frac{\Phi_k}{N_t} - \mu_0 H_k A_t\right)^2 u^2(A_s)\right]^{1/2},$$
$$(4.16)$$

where

$$u(A_s) = \sqrt{h^2[u^2(r_2) + u^2(r_1)] + (r_2 - r_1)^2 u^2(h)} \quad (4.17)$$

whereas $u(\Phi_k)$ can be calculated as

$$u(\Phi_k) = \sqrt{u^2(\Phi_{k-1}) + (u^2(v_k) + u^2(v_{k-1})) \frac{T_s^2}{4}}, \qquad (4.18)$$

assuming that μ_0 and the sampling time T_s have zero uncertainty and using the trapezoidal rule for integration. The formulae do not take into account two deterministic contributions, described in the following.

4.4.3 Post-degaussing residual field

The first deterministic contribution is assuming zero initial condition for the integration, thus by neglecting the remanent field B_0 left from the degaussing. This contribution can be evaluated separately *a posteriori* and can be evaluated as:

$$B_0 = \frac{1}{2}(B_{sat,P} + B_{sat,N}) \qquad (4.19)$$

where $B_{sat,P}$ and $B_{sat,N}$ are two points of the magnetization curve evaluated in the saturation region, at two opposite symmetric magnetic field values H_{sat}, such that $H_{sat,P} = -H_{sat,N}$.

4.4.4 Integration drift

The integration drift is a problem common to a wide variety of applications, where the signal of interest is obtained by integrating another signal, which is possible to measure. Integration drift is typical of inductive magnetic field measurements, where the induced voltage at the terminals of a sensing coil is integrated to obtain the linked flux and the magnetic flux density. More specifically, integrating a signal magnifies low-frequency noise components, generally having a $1/f$ profile, arising from different sources in the acquisition chain [162]. In general, the measured voltage v can be decomposed as:

$$v = v_s + v_o, \qquad (4.20)$$

where v_s is the measurand signal and v_o is a slow varying offset term, causing the drift. Fig. 4.14 provides a visual representation of the problem on typical test cycles used for DC flux-metric methods.
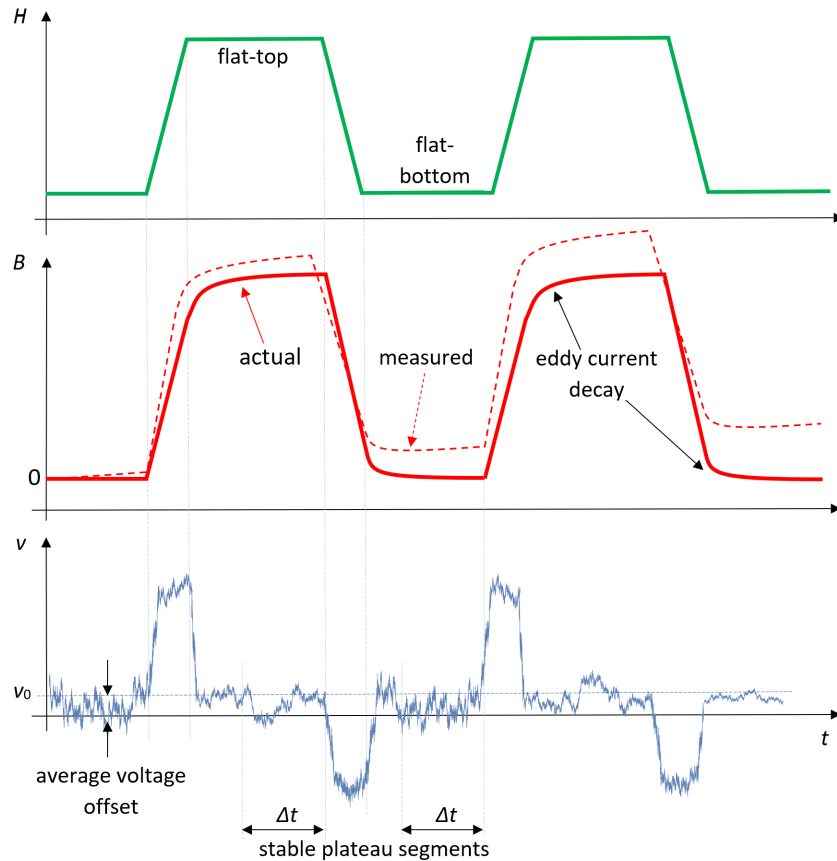
Fig. 4.14 Schematic representation of a test cycle. The offset voltage determines a deviation of the measured value from the actual one, increasing with time.

Ideally, the measured voltage is expected to be zero on the plateaus after the eddy currents generated during the preceding ramp have fully damped. Actually, the measured voltage is never zero because the offset voltage v_o is superimposed to the measurand signal. v_o changes are slower than the measurand and can be approximated as a constant during the integration period. Constant v_o means linear drift. This approximation is the principle of the most basic correction algorithms. For the experimental results presented in Chap. 5, the offset voltage is compensated utilizing two correction techniques. The first is an online updating algorithm, where the offset voltage is assumed to behave as a piece-wise constant function. Each piece has a duration interval of 1 s, where the estimate is updated. The update is calculated

by averaging the measured values in the considered time window. The update is calculated and applied only when B reaches a stable plateau and the eddy currents generated in the previous ramp have fully damped. The offset estimate is constant on the ramps and during the eddy currents' transients, and it is not updated. As the points of the initial magnetization curve are evaluated by semi-difference between positive and negative symmetric values, any residual drift accumulated on the ramps is already compensated. Fig. 4.15 shows an example of voltage offset estimated by using the algorithm mentioned above. In order to avoid long periods where the offset is not updated, the ramp rate value was kept constant for each current cycle (or equivalently, field cycle) and at a convenient high value, such that the ramp duration is lower than the next plateau.
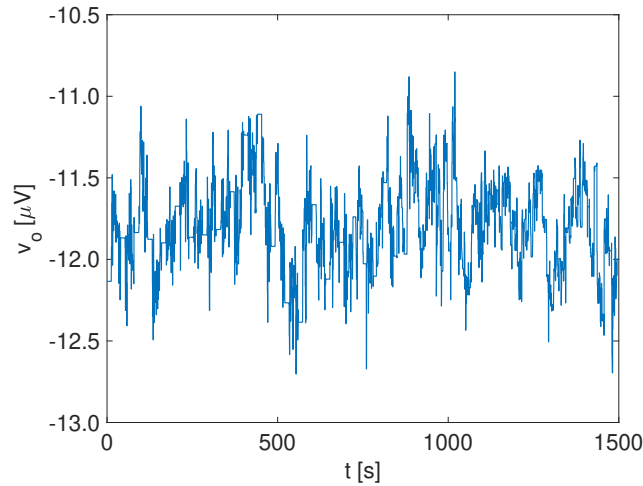
Fig. 4.15 Example of offset voltage estimated online on the plateaus.

The second technique, applied in addition to the first one for hysteresis loop measurements, is the method of the envelope [163, 164, 165], where the signal is corrected on the assumption is periodic. More specifically, since the hysteresis loop measurement consists of cycling the test specimen with a periodic waveform, the linear trend of the signal can be removed by imposing the symmetry between the first and the last measured point.

4.4.5   Impact of the superconductor magnetization

The superconductor magnetization can have a non-negligible impact at low excitation fields and influence the measurement results, and therefore, it needs to be verified.

In Sec. 4.1.4, it was seen that the excitation coil is magnetized when the excitation field is applied. In many applications such as superconducting magnets [16, 39, 166, 167, 168], the persistent currents have a significant impact at low field values, while in others, such as superferric magnets, [169], the effect can be ignored because the field in the air gap is modeled by suitably shaping the magnet poles.

In [16, 38], the magnetization M_s of the superconductor is modeled as a dipole field produced by two lines of current I_s and $-I_s$, placed at a distance d_w, where d_w is the wire diameter. A similar approach can be proposed for a torodal permeameter, in which the magnetization M_s of the superconductor can be modeled as a magnetic field generated by a fictitious toroidal coil, having N_e turns and carrying an equivalent current I_s. An equivalent representation is to model this coil as two parallel arrays of current lines I_s and $-I_s$, separated by a distance d_w, arranged along a circumference. Therefore, I_s can be computed from the following formula,

$$M_s = \frac{N_e I_s}{2\pi r_p},$$
(4.21)

where r_p is the superconducting wire radial position and N_e the number of excitation turns. Using the model presented in the model used in Sec. 4.1.5, being $B = 0.57$ T at an excitation current of $I = 40$ and $N_e = 2557$ turns, from Fig. 4.6, M_s=4.61 kA/m at $B = 0.6$ T. If the coil is at a radius of $r_p = 35$ mm, this leads to $I_s \approx 0.42$ A. Given how the excitation coil is wound around the permeameter (black current lines in Fig. 4.16), the superconductor magnetization contributes twice: one fictitious coil wound on the inner side of the toroid (red current lines in Fig. 4.16) and another one wound on the outer side of the toroid (green current lines).

In this configuration, having two parallel toroidal solenoids, ideally, the field should be confined inside the toroid. Therefore, the contribution from M_s to the field H should be zero. On the other hand, a stray field contribution H_M can leak from outside the fictitious coils, determine a field bias, and influence the iron magnetization. Stray fields in a toroidal geometry are non-negligible in the case of large toroidal solenoids, where the radial thickness of the toroid is comparable with its circumference or when the stacking of the excitation turns is low. Examples can be found in the literature [170, 171], where for large solenoids having 8 to 16 turns on a circumference length in the order of a few m, a non-negligible stray field is present. Given the high-density stacking of the excitation turns, 500 turns for each layer, the contribution of M_s to the applied field is negligible. The hypothesis can be verified
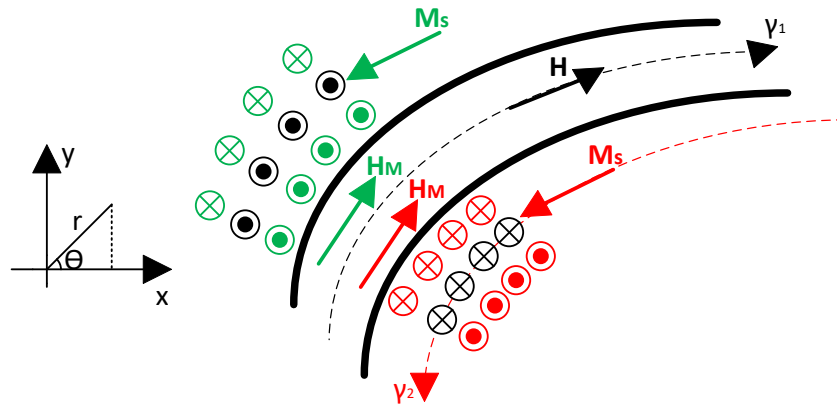
Fig. 4.16 Representation of the persistent current lines, and the transport current lines, in the reference frame of the permeameter. In black, the transport current lines. In red, the current lines generating the superconductor magnetization.

analytically and numerically. A simplification that can be introduced, given the high-density stacking of the turns, is to model the red and the green current lines in Fig. 4.16 as two couples of two concentric circular shells carrying a current $N_e I_s$, pointing in opposite directions in the two shells, respectively. The impact can be assessed only for one couple of shells.
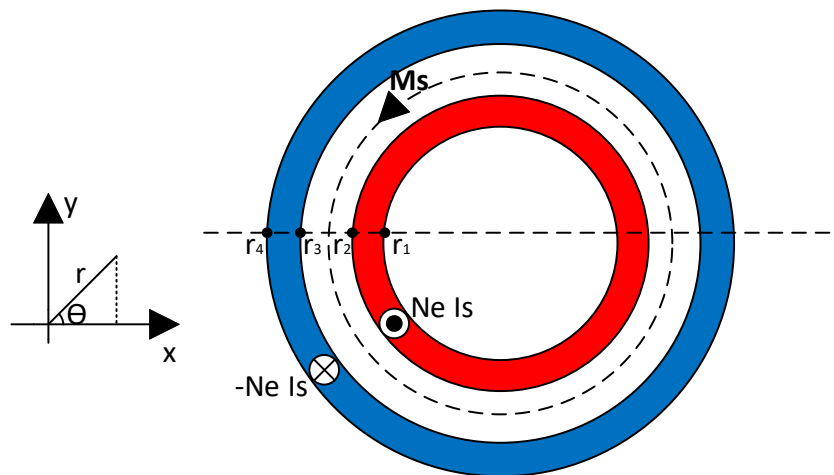
Fig. 4.17 Two concentric current shells carrying a current $N_e I_s$ (red) and $-N_e I_s$ (blue), modeling a toroidal solenoid having a high number of turns.

For $r < r_1$ and $r > r_4$, M_s=0. For $r > r_r 4$, $M_s = 0$. For $r_3 <= r <= r_2$, $M_s = N_e I_s/(2\pi r)$.

The verification has also been performed numerically by considering the layout

of Fig. 4.16, and thus the spacing between turns, using FE analysis for validation. The results, shown in Fig. 4.18 and Fig. 4.19, demonstrate that in the absence of a transport current, the superconductor magnetization provides a contribution of about 0.0002 A/m in the iron core, which is six orders of magnitude lower than the minimum applied field. Inside the two layers of current lines, the field increases up to the superconductor magnetization M_s. In conclusion, the superconductor magnetization provides a negligible contribution to the applied field, and therefore, it can be ignored.
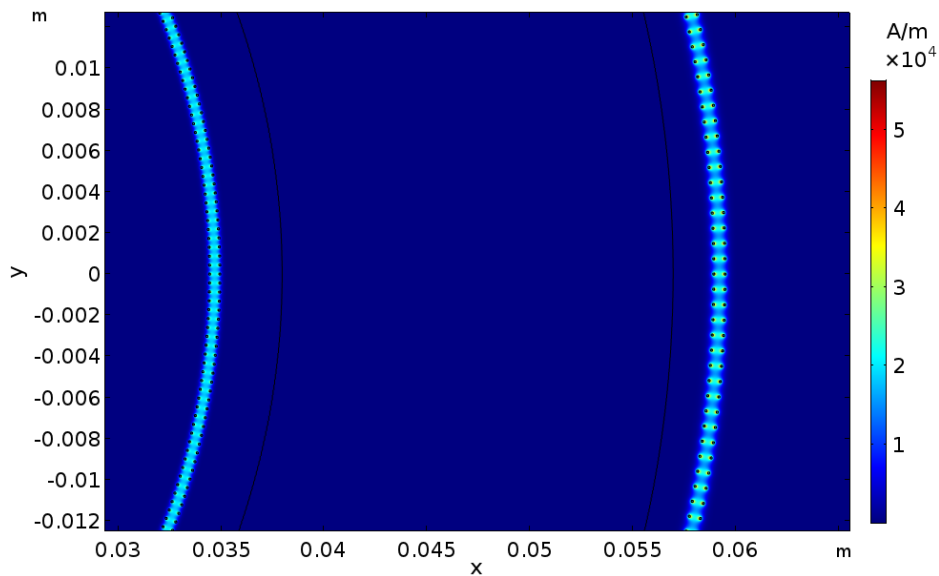
Fig. 4.18 FE simulation of the superconductor magnetization, modeled according to the configuration shown in Fig. 4.16 as generated by a fictitious distribution of current lines.
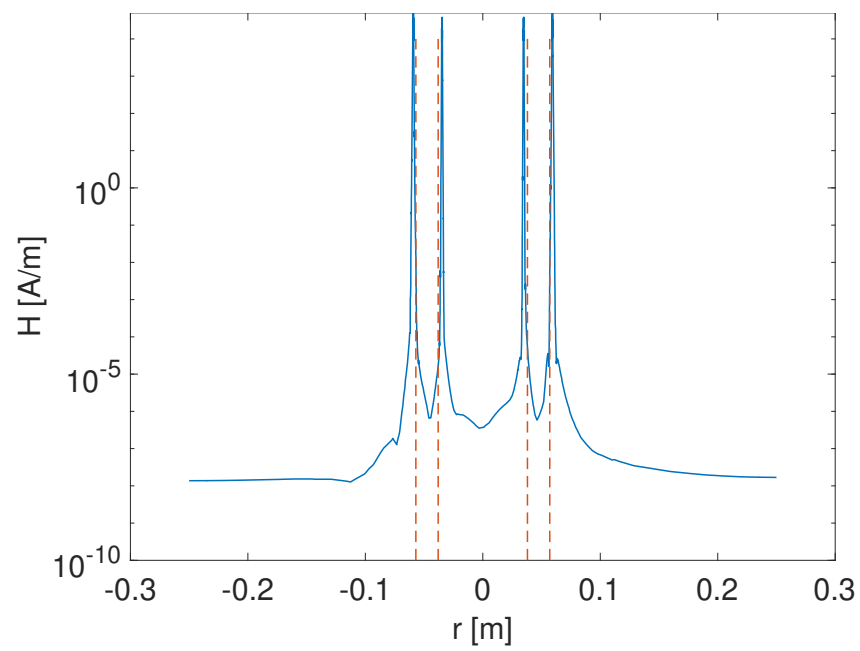
Fig. 4.19 Module of the magnetic field H shown in Fig. 4.18 as a function of the radial position. The red dashed lines were drawn to visually identify the iron toroid position.

Chapter 5

Experimental results and discussion

In this Chapter, the performance of the superconducting permeameter proposed in Chap. 4 is assessed by presenting two case studies concerning the magnetic characterization of ARMCO® Pure Iron, the yoke steel for the HL-LHC magnets, at very high-fields. Two test specimens were measured, specimen B from the pre-production (see Sec. 3.2), to validate the design, and a specimen from the production batch (see Sec. 3.6). The results of ARMCO® Pure Iron were previously published also in [P2]. However, the measurement results presented in this dissertation were determined with a higher accuracy, because the guidelines presented in Sec. 4.2 were applied.

The results were validated by comparison with the measurements performed on a second test specimen and with measurements performed at different test temperatures, 77 K and 293 K, verifying how the saturation flux density scales with the temperature and comparing the results with those from the literature.

5.1   ARMCO® specimen B

5.1.1   Measurement parameters

Tab. 5.1 reports the parameters used for the characterization of ARMCO® specimen B.

Table 5.1 Measurement parameters for ARMCO® specimen B. A coverage factor of 2 was applied to the uncertainty values.

Parameter	Value
Excitation turns N_e	3298
Sensing turns N_t	90
Induced voltage	0.20+0.00219v_k [mV]
Excitation current	0.61+0.0058I_k [mA]
Specimen inner diameter d_1	75.96$\pm$0.03 mm
Specimen outer diameter d_2	113.92$\pm$0.03 mm
Specimen total thickness h	12.12$\pm$0.03 mm
Sensing coil area (geometrical) A_t	386.552 mm^2
Sensing coil area (calibrated) A_t	421.357$\pm$0.306 mm^2
Iron thermal contraction coefficient k_{Fe}	0.99796$\pm$2.05$\times$10^{-5}

5.1.2   Initial magnetization curve

Fig. 5.1 shows the measured initial magnetization curve and the corresponding relative permeability values, up to a magnetic flux density 2.72 T.

Fig. 5.1 Measured initial magnetization curves and corresponding relative permeability values of ARMCO® specimen B at 4.2 K.

The material saturates at a flux density of 2.260 T at 4.2 K, corresponding to a saturation magnetization of 2.167. The measured value is comparable with similar values from the literature, and with the theoretical curve shown Sec. 2.5. The peak relative permeability is 2541$\pm$89, thus having an uncertainty of 3.49 %. The initial permeability could not be measured due to a lack of resolution in controlling the

power supply for currents lower than 20 mA, impacting the degaussing procedure and determining a shift on the *B*-axis of the first hysteresis loops, which are asymmetric and oscillate around the residual of degaussing. The uncertainty of the magnetic field values is $(10.99 + 0.0004H_k)$ A/m, which results in an uncertainty of about 4 % on the first measured H value. A coverage factor 2 was applied to obtain the uncertainty corresponding to a 95 % level of confidence. The relative uncertainty decreases as the field increases, reaching a value of 0.044 % at 442 kA/m. The uncertainties of the magnetic field and the flux density values are also reported in Fig. 5.2, and plotted as a function of *B*.
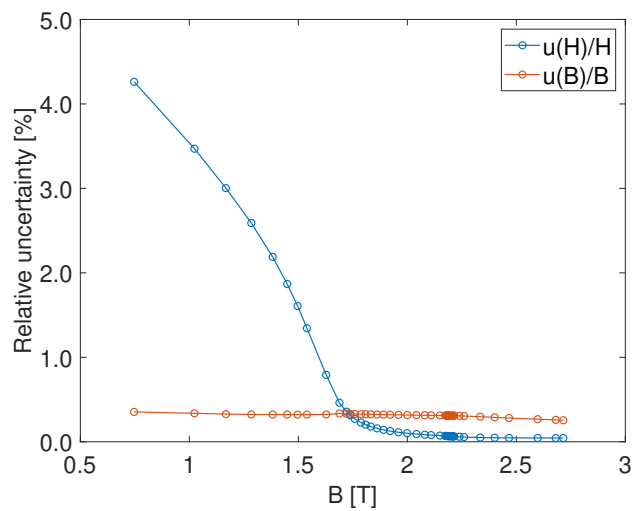
Fig. 5.2 2-σ relative uncertainty values corresponding to the magnetization curve presented in Fig. 5.1

The flux density values have an uncertainty lower than 0.35 %, decreasing as the flux density increases. At flux densities higher than 1 T, the uncertainty ranges between the 0.25 % and the 0.32 %. Fig. 5.3 shows the comparison between the measured magnetization curve and other three curves, measured on another specimen of the same material at 4.2 K, 77 K, and room temperature, respectively, by using a copper excitation coil with 277 turns. The measurements at 293 K were also previously shown in Fig. 3.6.

The relative permeability values, thus the flux density values at a fixed excitation field, decrease for fields lower than 1.5 T as the temperature decrease. The reduction, as previously mentioned in Sec. 3.3, was expected due to an increased anisotropy. In particular, the peak permeability decreases from about 3000 at room temperature to about 2800 at 77 K, until 2541 at 4.2 K. In the saturation region, the flux density

Fig. 5.3 Comparison between measured initial magnetization curves and corresponding relative permeability values of ARMCO® specimen B. (1) is the measurement performed by superconducting permeameter at 4.2 K. (2) indicates the measurements performed on another specimen of the same material, performed respectively at 4.2 K, 77 K and 293 K. In the bottom figure, the uncertainty values for the three measurements of specimen (2).

goes from about 2.03 T, at 24 kA/m and 293 K, to about 2.07 T at 4.2 K. In terms of magnetization, it is 2.003 T at room temperature and 2.03 T. This behavior is also consistent with Fig. 2.13 in Sec. 3.3.

The two curves measured at 4.2 K by two different systems are consistent, and they present a maximum mismatch of about 0.1 %, within the uncertainty values. In the low field region, the curves differ by 10 %, but this is not an issue because the variations are within what could be expected when measuring two different specimens of the same material. Sec. 3.6 reports an example.

In conclusion, the agreement between the two measurements performed at 4.2 K, the behavior in the saturation region consistent with the literature, and the agreement be-

tween the room temperature measurements performed by using two different systems, Fig. 3.6 are all factors that validate the design and the metrological performance of the superconducting permeameter. The uncertainty values of the H-field, at a fixed B-field value, are one order of magnitude higher. This because, from Sec. 4.4.2, $u(H)/H \approx N_e u(I)/I$. Being the current measured with the same uncertainty, increasing the number of excitation turns leads to an increased uncertainty of the H values. On the other hand, the uncertainty of the B-field values is lower, at a fixed H-field, because the cross-section area of specimen (1) is twice the cross-section of specimen (2).

The data of the magnetization curve from Fig. 5.1 were fit by using Wlodarski's equation (Eq. 1.11), to be used as an input to FE analysis software and simulate the magnet behavior. Fig. 5.4 shows the comparison between the measured values and the best fit. The parameters of the fit are: $\mu_0 M_a = 0.4437$ T, $\mu_0 M_B = 1.7216$ T, $a = 7015.8$ A/m, and $b = 107.55$ A/m.
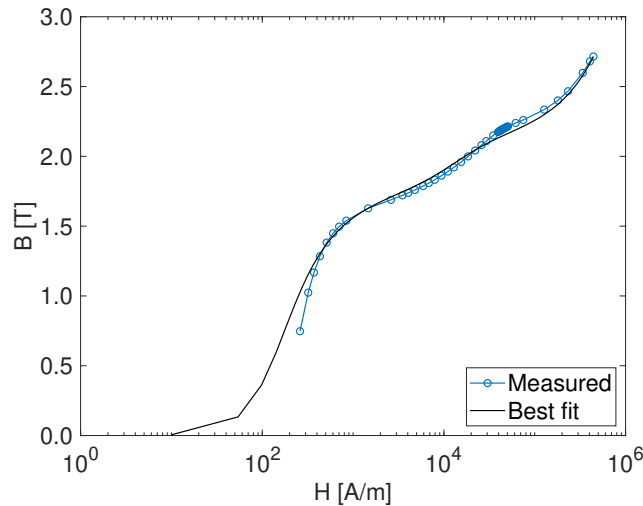
Fig. 5.4 Initial magnetization curve of ARMCO® specimen B measured at 4.2 K (blue) and best fit obtained using Eq. 1.11 (black).

Due to modeling limitations, Eq. 1.11 does not fit the experimental data in the low field region properly. In fact, Eq. 1.11 is based on a Brillouin's function (Eq. 1.11), and describes an anhysteretic magnetization curve, which can differ significantly from the initial magnetization curve in the low-field region.

5.1.3   Hysteresis loop

Fig. 5.5 shows the measured DC hysteresis loop.
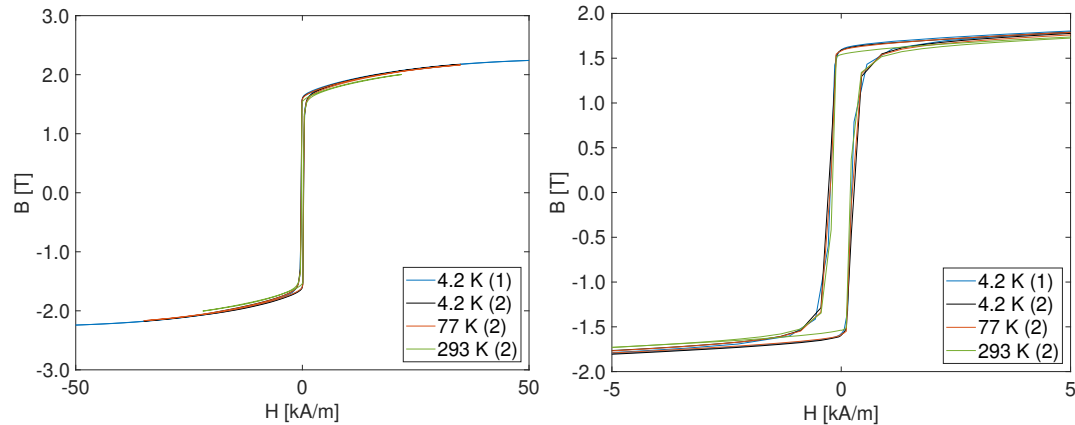
Fig. 5.5 Measured hysteresis loop of ARMCO® specimen B measured at cryogenic temperature by superconducting permeameter (blue). The hysteresis loops measured at room temperature (green), 77 K (red), and 4.2 K (black) on a second specimen are plotted for comparison. Left) Full hysteresis loop, and Right) Zoom on the low field region.

The hysteresis loop area increases as the temperature decreases, and therefore, the material becomes magnetically harder. More specifically, the coercive field value increases by about 23 %, from 196 A/m at room temperature up to 241 A/m at cryogenic temperature. Ideally, a lower variation was expected, of about 16 %, similarly to the decrease of the peak permeability, but the increasing remanence partially mitigates the decrease of peak permeability. In fact, as a result of the saturation magnetization increase, the remanence also increases, from 1.54 at room temperature to 1.59 at 4.2 K. The uncertainty of the coercive field value is 13 A/m, corresponding to about 5.2 % of the measured value. This value is mainly due to the low data scattering in the coercive field region, and that H_c is determined by linear interpolation of the two closest measured values. However, it does not differ significantly from the typical 3 % that the standard IEC 60404-4 reports. Tab. 5.2 summarizes the relevant measured values.

Table 5.2 Summary of the results of the magnetic characterization of ARMCO® specimen B at different temperatures.

Specimen/Temperature	1/4.2 K	2/293 K	2/77 K	2/4.2 K
B |1.2 kA/m [T]	1.597	1.570	1.599	1.602
B |24 kA/m [T]	2.06	2.03	2.06	2.07
$\mu_{r,max}$	2541	3062	2824	2557
H_c [A/m]	241	196	246	248
B_r [T]	1.59	1.54	1.58	1.59

5.2 Specimen from the production batch

5.2.1 Measurement parameters

Tab. 5.3 reports the parameters used for the characterization of ARMCO® from the production batch.

Table 5.3 Measurement parameters for ARMCO® from the production batch. A coverage factor of 2 was applied to the uncertainty values.

Parameter	Value
Excitation turns N_e	4595
Sensing turns N_t	90
Induced voltage	$0.10+0.00219v_k$ [mV]
Excitation current	$0.61+0.0058I_k$ [mA]
Specimen inner diameter d_1	104.88 ± 0.03 mm
Specimen outer diameter d_2	114.30 ± 0.03 mm
Specimen total thickness h	5.85 ± 0.03 mm
Sensing coil area (geometrical) A_t	174.416 mm^2
Sensing coil area (calibrated) A_t	167.738 ± 0.086 mm^2
Iron thermal contraction coefficient k_{Fe}	$0.99796\pm2.05\times10^{-5}$

5.2.2 Initial magnetization curve

Fig. 5.6 shows the measured initial magnetization curve and the corresponding relative permeability values, up to a magnetic flux density of 2.82 T.
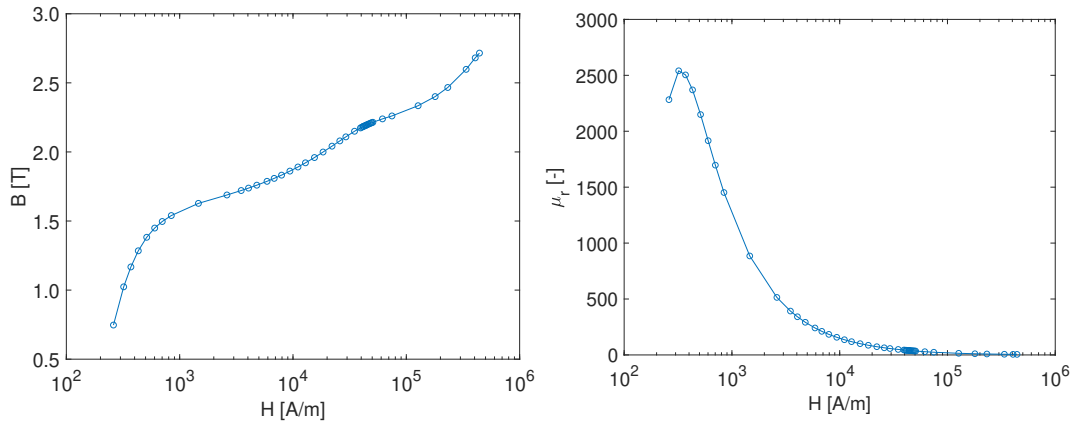
The material saturates at a flux density of 2.250 T at 4.2 K, corresponding to a saturation magnetization of 2.155. The value is again compatible with values
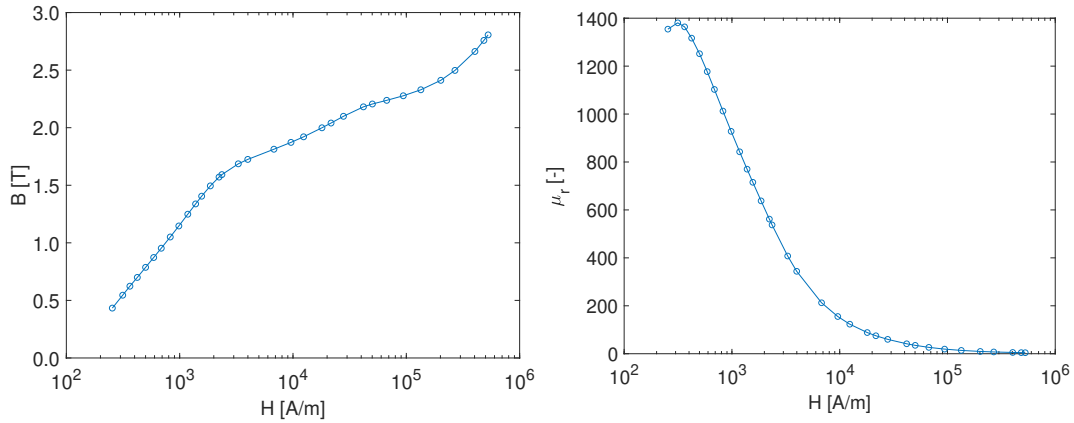
Fig. 5.6 Measured initial magnetization curves and corresponding relative permeability values of ARMCO® from the production batch at 4.2 K.

from the literature and with the value reported in Sec. 5.1.2. The peak relative permeability is 1381±53, thus having a relative uncertainty of 3.86 %, comparable with the previous case. The initial relative permeability could not be measured for the same reason mentioned in Sec. 5.1.2. The uncertainty of the magnetic field values is $(9.63 + 0.0003H_k)$ A/m, which results in an uncertainty of about 4.58 % on the first measured H-value. However, the trend of $u(H)$ as a function of B is different, due to the higher circumference radius r_0 in Eq. 4.14. A coverage factor 2 was applied to obtain the uncertainty corresponding to a 95 % level of confidence. The relative uncertainty decreases as the field increases and reaches a value of 0.037 % at 527 kA/m. The uncertainties of the magnetic field and the flux density values are reported as a function of B in Fig. 5.7.

The flux density values have an uncertainty lower than 1.07 %, decreasing as the flux density increases and presenting the same uncertainty trend already shown in Sec. 5.1.2, as a function of B. On the other hand, the smaller cross-section area of the specimen determines a higher average uncertainty, which reaches a minimum value of 0.77 % at 2.80 T.

Fig. 5.8 shows the comparison between the measured magnetization curve, the corresponding magnetization curve measured at room temperature, and other three curves, measured on another specimen of the same material at 4.2 K, 77 K, and room temperature, respectively. The measurements of both specimens at room temperature were performed by split-coil permeameter described in Sec. 2.2.1. The measurements
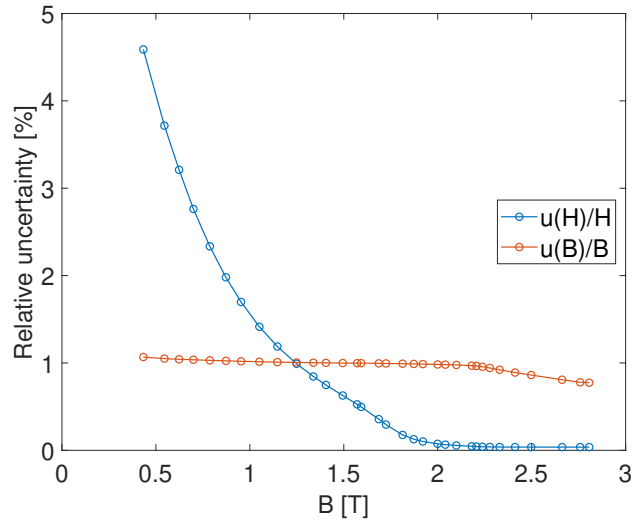
Fig. 5.7 2-σ uncertainty values corresponding to the magnetization curve presented in Fig. 5.6

performed at cryogenic temperatures on the specimen (2) were performed using a manually wound permeameter with a copper excitation coil of 417 turns.

The properties of the two specimens at room temperature are very similar, and their peak permeabilities are 2610 (specimen 1) and 2517 (specimen 2). The peak permeability of specimen 2 ranges from 2517 at room temperature, to 2054 at 77 K, and 1809 at 4.2 K. A similar degradation was also expected for specimen 1, but the measured peak permeability is much lower (1381). On the other hand, in the saturation region, the flux density values consistently increase as the temperature decreases. They pass at 19 kA/m from 1.95 T at 293 K to about 2.02 T at 4.2 K. The mismatch between the two curves measured at 4.2 K was further investigated by comparing their hysteresis loops, and the results are commented in Sec. 5.2.4. The data of the initial magnetization curve were fit by Wlodarski's equation, similarly to Sec. 5.1.2 and the result is shown in Fig. 5.9. The parameters of the fit are: $\mu_0 M_a = 0.4715$ T, $\mu_0 M_B = 1.6889$ T, $a = 7016.5$ A/m, and $b = 314.20$ A/m.

5.2.3   Hysteresis loop

Fig. 5.10 shows the measured DC hysteresis loop. Tab. 5.4 summarizes the relevant measured values.

The material becomes magnetically harder as expected, and the coercive field increases by about 8.67 %, from 196 A/m at room temperature to 213 A/m at
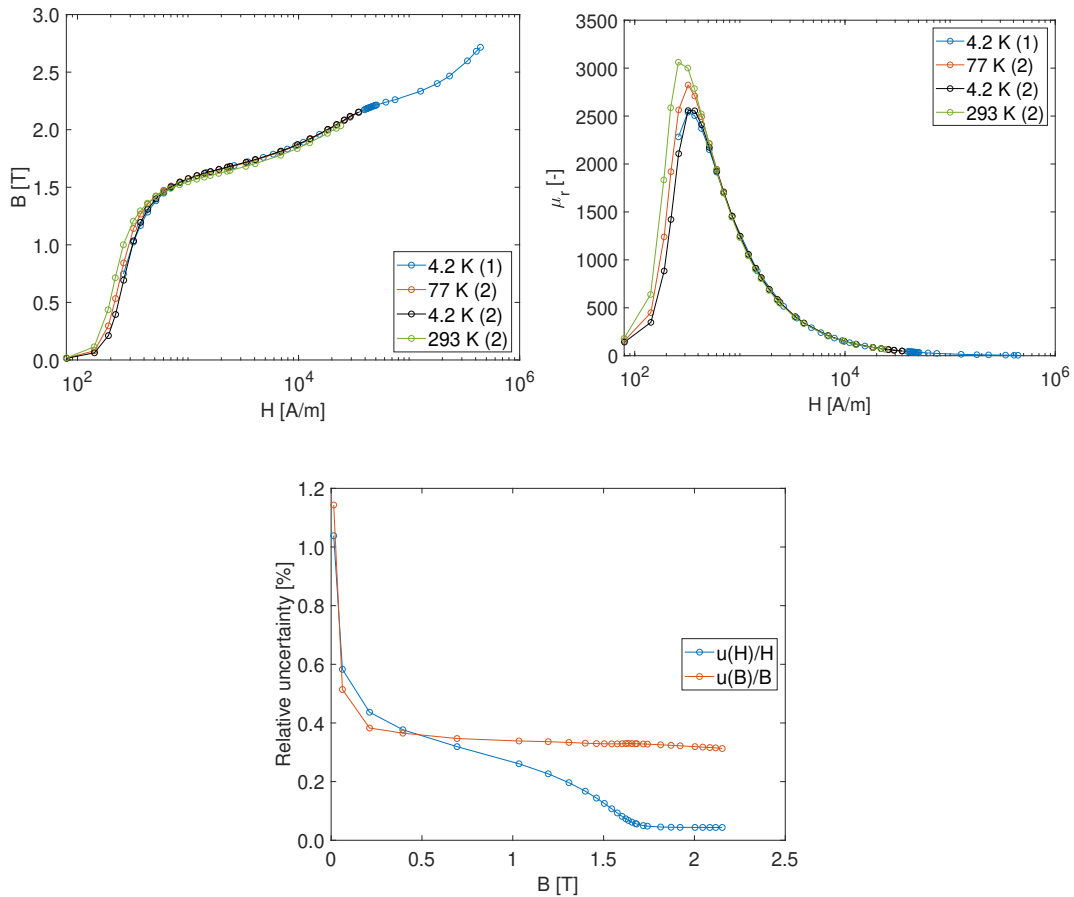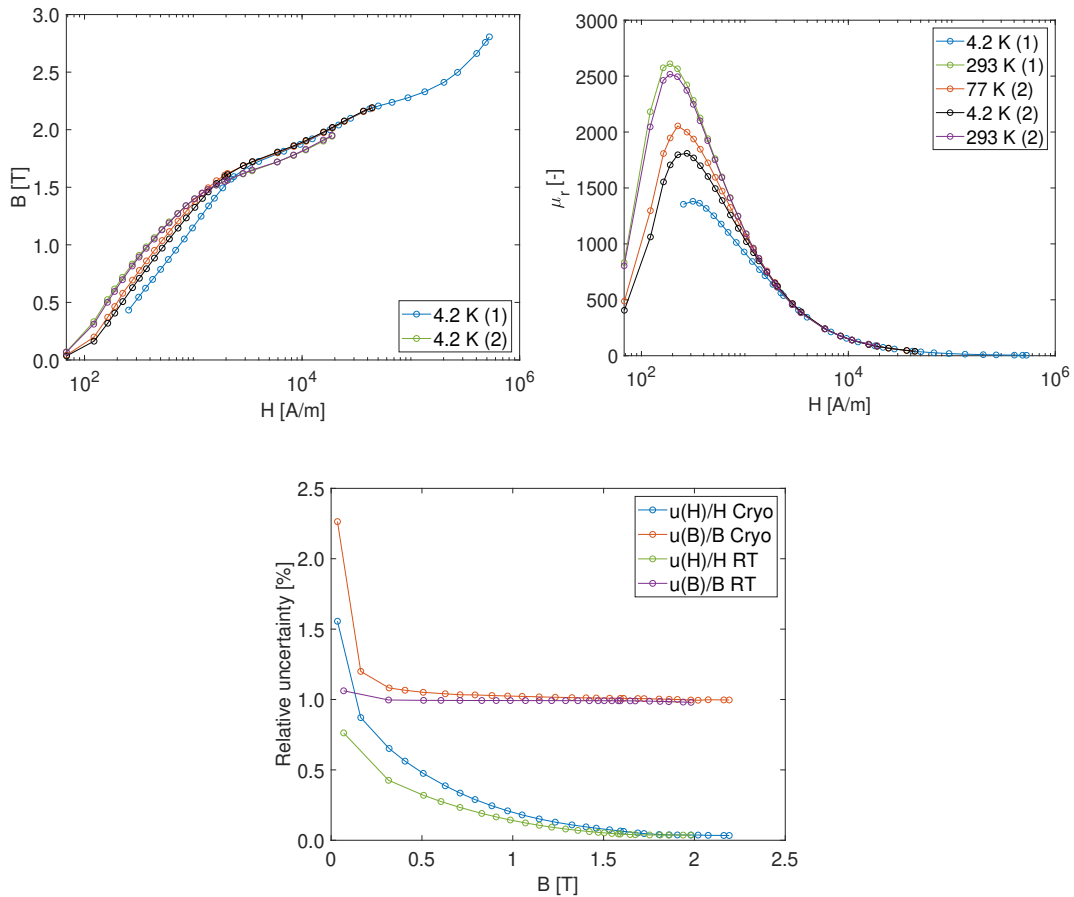
Fig. 5.8 Comparison between measured initial magnetization curves and corresponding relative permeability values of ARMCO® from the HL-LHC production batch. (1) indicates the specimen measured by superconducting permeameter (blue), measured also at room temperature (green). (2) indicates the measurements performed on another specimen of the same material performed respectively at 4.2 K (black), 77 K (red), and 293 K (purple). In the bottom figure, the uncertainty values for the three measurements of specimen (2).

4.2 K. The uncertainty of the coercive field value measured at 4.2 K is 37 A/m, corresponding to about 17.2 % of the measured value. This value is higher than the previous case study due a combination of poor data scattering in the coercive field region, similarly to the results shown Sec. 5.1.2, and to the higher uncertainty of the flux density values.

On the other hand, the remanence sensibly decreased from 0.83 T to 0.65 T, which is unexpected. A decrease is observed also on specimen (2), where the remanence decreased of 0.05 T from 293 K to 4.2 K. However, the decrease lies within the uncertainty value, about 1 %, and therefore it is not considered as significant.

In conclusion, the mismatch among the measurements performed on specimens (1)
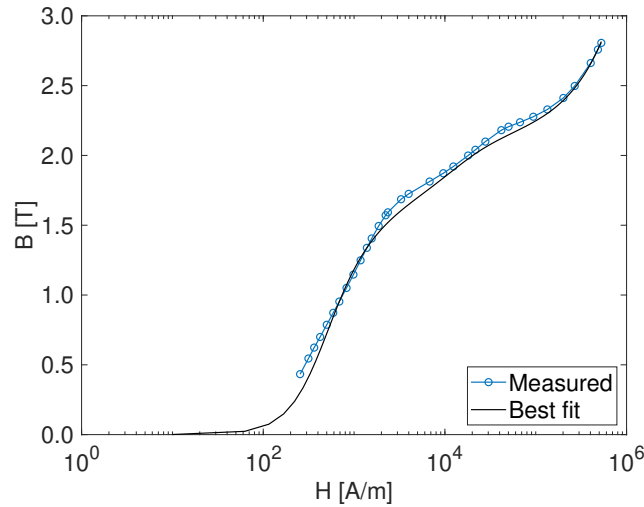
Fig. 5.9 Initial magnetization curve of ARMCO® from the production batch measured at
4.2 K (blue) and best fit obtained using Eq. 1.11 (black).
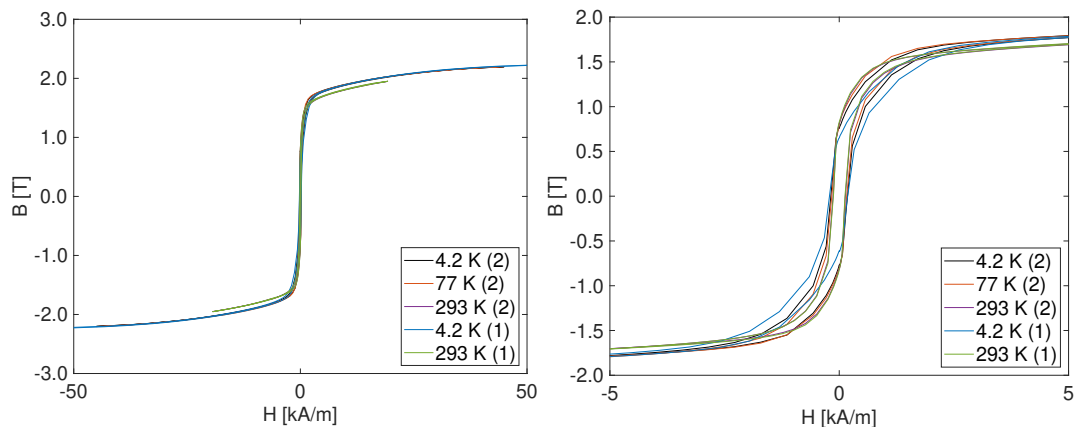
Fig. 5.10 Measured hysteresis loop of ARMCO® from the production batch for different test
temperatures. The loops were measured on two different test specimens, (1) also measured
by using the superconducting permeameter and (2) measured at cold by using a copper
excitation coil. Left) Full hysteresis loop, and Right) Zoom on the low field region.

and (2) at 4.2 K is also present on the hysteresis loops. A difference of 30 A/m is
detected on the coercive field, whereas the residual flux density decreased by about
15 %, from 0.76 T to 0.65 T. This outcome is discussed in Sec. 5.2.4.

Table 5.4 Summary of the results of the magnetic characterization of ARMCO® from the production batch at different temperatures.

Spec./Temp.	1/4.2 K	1/293 K	2/293 K	2/77 K	2/4.2 K
B ǀ1.2 kA/m [T]	1.249	1.447	1.450	1.444	1.401
B ǀ24 kA/m [T]	2.06	2.01	2.01	2.07	2.07
$\mu_{r,max}$	1381	2610	2517	2054	1809
H_c [A/m]	213	134	128	163	183
B_r [T]	0.65	0.83	0.81	0.81	0.76

5.2.4   Degradation of the magnetic properties

The initial magnetization curves and the hysteresis loops measured at 4.2 K on the specimen from the production batch, presented in Sec. 5.2.2 and Sec. 5.2.3, show a significant mismatch. The mismatch is visible in Fig. 5.11.
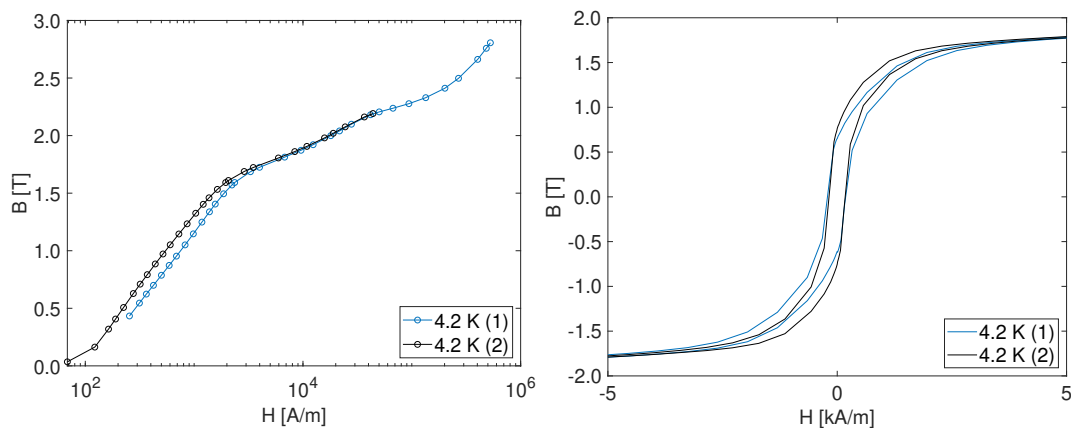
Fig. 5.11 Measured initial magnetization curves (right) and hysteresis loops (left) of ARMCO® from the production batch at 4.2 K, measured by means of the superconducting permeameter (1) and a permeameter with copper excitation coil.

A difference of 23 % of the peak permeability from 1809 (2) to 1381 (1) was measured, whereas the coercive field did not change significantly. The remanence significantly decreased from 0.76 T to 0.65 T. Their identical behavior in the saturation region and their consistency with the curves measured at 77 K and 293 K excludes calibration errors in the measurement operation.
The behavior seems mechanical, related to applied cold work on the test specimen (1), and the trend very similar to the one presented in Sec. 3.5, where the stress was applied in controlled conditions.

A dedicated study should be carried out to identify the cause of this mechanical stress. A possible source is a too high cooling rate, which might have created some internal stress within the specimen during the cooling process from room temperature. In fact, preliminary measurements performed on specimen B, from Sec. 5.1.2, in liquid nitrogen showed a similar pattern in terms of magnetization curve and hysteresis loop. In one case, the cryogen was directly poured on the specimen (black), while in the other case (blue), the specimen was cooled slowly using gas nitrogen at an average rate of 1 K/min to avoid thermal shock. Liquid nitrogen was poured once the temperature was 100 K. Slowly cooling the specimen apparently solves the problem, on the one hand. On the other hand, this degradation is not reproducible and requires further investigation to understand its cause and how to avoid it.
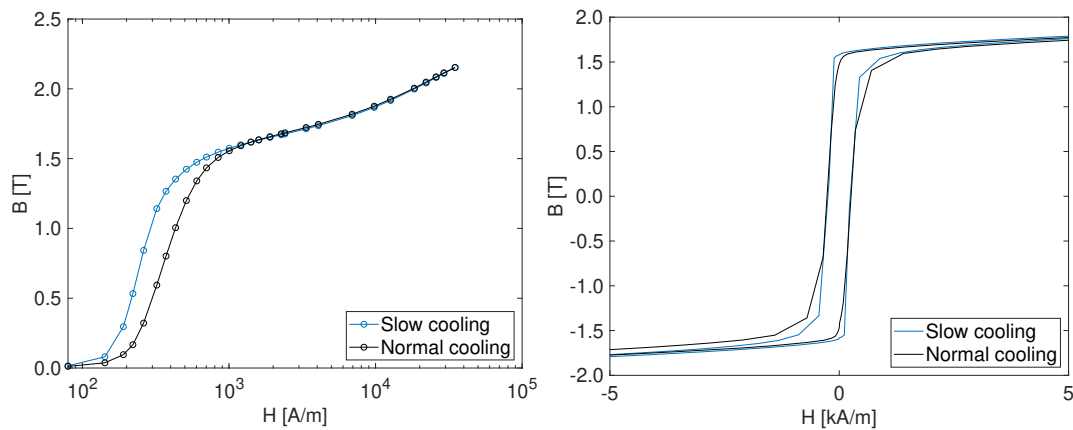
Fig. 5.12 Measured initial magnetization curves (right) and hysteresis loops (left) of ARMCO® specimen B, measured at 77 K, when measured after direct immersion in nitrogen bath (black) and when the specimen was slow cooled up to the test temperature.

5.3   Summary and final comments

In this Part, a superconducting permeameter was proposed, designed, and validated to perform accurate measurements of soft ferromagnetic alloys in the saturation region and respond to the demand of data for ARMCO® Pure Iron in the context of the HL-LHC project.

The system was validated by presenting two case studies concerning the characterization of two specimens of ARMCO® Pure Iron, presenting different properties at

room temperature, up to a magnetic field H of about 500 kA/m, and comparing the magnetization curves in the saturation region with the measurement performed on another identical test specimen, and with theoretical values from the literature.

The superconducting permeameter proved to be inaccurate in the low-field region, where uncertainty values of H up to 5 % were obtained, more than one order of magnitude higher than room temperature measurements at the same value of B. The higher uncertainty originated from the higher number of excitation turns, about 4000 versus 180 at 293 K, which increased the sensitivity to the excitation current measurement uncertainty. Moreover, the higher number of turns makes the system more sensitive to power supply inaccuracies, which impact the degaussing procedure. On the one hand, the residual of degaussing is corrected. On the other hand, measurements at lower B are not possible because the iron magnetization remains confined on a minor asymmetric loop, that can be wiped out only applying a higher field.

The uncertainty of the B-field values is closely comparable to room temperature in the second case study because the number of sensing turns is the same, and the specimen's cross-section does not change significantly from warm to cold. Values lower than 1.07 % were obtained in the second case study, decreasing as the flux density increases. In the first case study, the uncertainty of the B values is one order of magnitude lower than in the second case study due to a specimen cross-section eight times higher than in the second case study. In conclusion, the system is not optimized for low-field characterization due to the higher uncertainty of the H values. This outcome was expected since the system was conceived to measure in the high-field region of the magnetization curve. Nonetheless, the problem can be easily addressed by winding a second auxiliary copper excitation coil with fewer turns to perform low-field characterization.

The proposed guidelines for magnetic characterization at cryogenic temperatures proved effective, especially for the calibration of the sensing coil. However, they need further refinement because effects of mechanical stress, most likely caused by a too high cooling rate, were detected in the low-field region. As previously shown in Sec. 3.5, cold work degrades the magnetic properties because it decreases the remanent field, thus resulting in a lower peak permeability. This effect is planned to be further investigated to improve the reproducibility of the measurement results.

Part III

A static-sample magnetometer for characterizing weak magnetic materials

Chapter 6

Problem statement and proposal

This Part of the dissertation presents a measurement method called static-sample magnetometry (SSM), proposed to measure the magnetic properties of feebly magnetic materials. The method is based on the flux-distortion detection principle, was realized with instrumentation already available in-house, and achieves a relative permeability resolution of 10^{-5}, comparable with VSM, the state-of-the-art solution. This Chapter presents the motivations leading to the proposal of this novel technique. Moreover, the measurement principle and its implementation are illustrated. Part of the content presented in this Chapter was previously published also in [P5].

6.1   Problem statement

In particle accelerators applications, many elements are required to display vanishing magnetic properties to avoid distorting the field interacting with the particle beam, as previously shown in Sec. 1.3. For the machines operated at CERN, the requirement for elements such as vacuum chambers, collars, or radiation shields, is that they shall have a relative permeability $\mu_r < 1.005$ at fields greater than 80 kA/m [48]. This requirement was originally intended for stainless steels, because for $\mu_r < 1.005$, the iron is exclusively in its austenitic phase, as also mentioned in Sec. 1.4.4.
Measuring such low values of relative permeability is challenging, and high-sensitivity systems are necessary to detect the properties of materials having permeability close to 1. For instance, given an excitation field of about 80 kA/m, namely 0.1 T in air, as a rule of thumb, a resolution in the order of 10^{-4} T would be necessary for a

specimen volume of hundreds of cm^3.

Flux-metric methods in a closed-circuit configuration such as toroids [172] show permeability uncertainties in the order of percent because they are limited in the range of excitation fields that can be generated, generally up to 50 kA/m due to space constraints in allocating the excitation coil turns. This field range is enough for soft ferromagnetic steels displaying relative permeabilities higher than 1000 but inadequate for feebly magnetic materials as mentioned in Sec. 2.1. Moreover, sensing coils with higher areas are necessary to detect the contribution of the test specimen to the total measured flux density. An example is shown in Fig. 6.1, where the uncertainty evaluated on a toroidal test specimen, made of co-wound stainless steel to be used for the voltage taps for the quench protection system in the International Thermonuclear Experimental Reactor (ITER) [172], is reported. Given a permeability of $\mu_r = 1.16$, the performance were considered as satisfying. However, for permeability values below 1.01, a 2 % uncertainty means that this value represents also the permeability resolution of the measurement system.
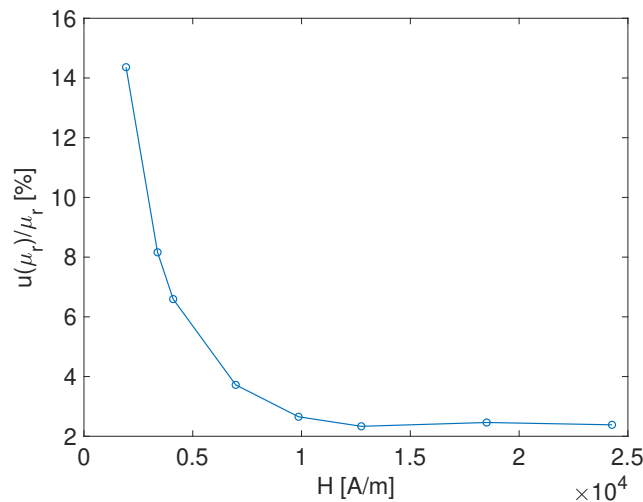
Fig. 6.1 2-σ uncertainty values of the relative permeability measured on a co-wound stainless steel for ITER [172]. Average relative permeability value $\mu_r = 1.16$.

The general approach when using a flux-metric method is to use an external field source, generally a magnetizing solenoid, to generate a field of 100 kA/m (about 0.13 T), as also proposed by the ASTM A342-A342M standard [124] and the IEC 60404-15 standard [125]. A similar approach was attempted to assess the metrological performance by realizing a mini-permeameter, shown in Fig. 6.2, where the excitation field is generated by a dipole magnet. The measurement system

consists of a 15000-turns sensing coil wound to obtain an area of 6.993 m^2 out of about 2 cm radius circumference. The holder hosting the sensing coil has a slot in the center to place the test specimen, having typical dimensions of 4x4x10 mm^3. The field generated by the magnet coil is measured twice, with and without the test specimen, using this sensing coil placed in the mid-plane of the magnet gap.
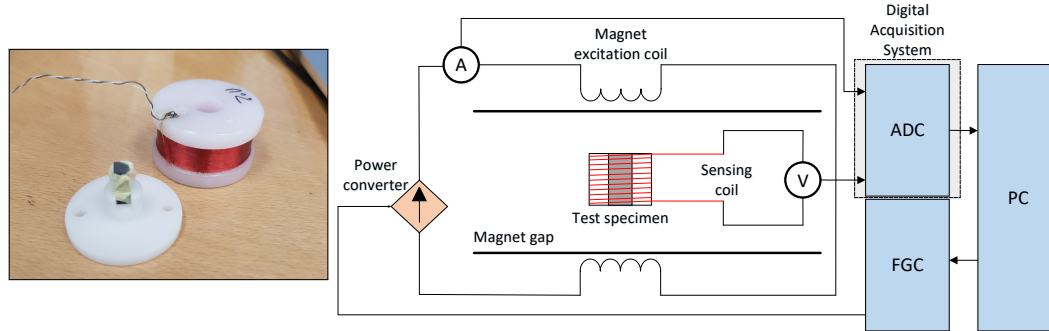
Fig. 6.2 (Left) Mini-permeameter and; (right) Layout of the measurement system

The field is applied by controlling the current in the magnet's excitation coil, and the characterization is performed by using the point-by-point method. The total magnetic field B in both measurements is obtained by integrating the induced voltage v at the sensing coil terminals

$$B = \frac{1}{A_t} \int_0^t v(\tau)d\tau, \tag{6.1}$$

where A_t is the area of the coil.

Indicating with B_s and B_a the total magnetic field values measured with and without the specimen respectively, and with A_s the cross-section area of the specimen, the relative permeability is evaluated in correspondence of each field level as

$$\mu_r = \frac{B_s A_t - B_b(A_t - A_s)}{B_b As}. \tag{6.2}$$

Fig. 6.3 shows an example of measurement results obtained on a test specimen of AISI type 316L. The repeatability of each point, represented by the error bars, is greater than 10^{-3}, and is inadequate for the applications of interest.
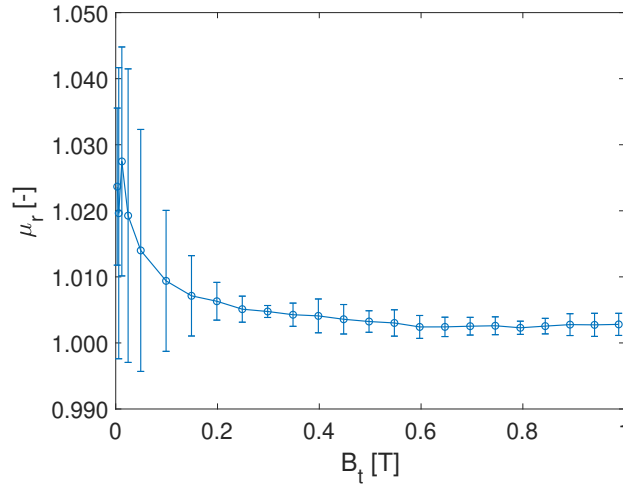
Fig. 6.3 Example of measurement results on a test specimen made of AISI type 316L measured by flux-metric method.

For such small geometries, the VSM is generally preferred due to its very high accuracy (10^{-5}), and is often available in national metrology laboratories. However, the VSM also presents some limitations from a technical point of view. It is limited to specimens having a size of few mm^3, which requires the test of multiple specimens sampled from different points in the main material slab to evaluate an average permeability, which can be considered a representative value of the material under test. Moreover, particular attention has to be dedicated to specimen cut from the main material slab with specimens of such small size because the machining can significantly impact the magnetic properties. For instance, this problem was mentioned for stainless steels in Sec. 1.4.4.

Flux-distortion detection techniques have never been fully exploited in the literature so far, and the only available example in the literature is the commercial Foerster Magnetoscop® [126], already presented in Sec. 2.3. However, it presents several limitations. A first constraint is the excitation field, generated by a small PM block, which limits the characterization at only one permeability value, measured at 80 kA/m. Moreover, being the field generated by a PM block placed in contact with the specimen, the magnetization is not uniform. Other constraints are that a minimum thickness of 30 mm in the direction of the field is required to avoid underestimating the permeability, and that there is no guarantee on the long-term stability of the calibration standards.

In this part of the dissertation, a Static-Sample Magnetometer (SSM) is proposed

to characterize feebly magnetic materials. The system aims at overcoming the limitations of state-of-the-art solutions to meet the typical requirements for particle accelerator applications. The system was developed using already available instrumentation, and works on bulky test specimens having a size of hundreds of cm^3.

6.2 Proposal

Flux-distortion detection techniques, as mentioned in Sec. 6.1, have never been fully exploited in the literature, and the Foerster Magnetoscop® do not reach the required level of accuracy. In this Section, the concept of the SSM is presented, with the aim of characterizing materials having susceptibility ranging between 10^{-5} and 10^{-2}. The proposal is to fully exploit the principle of the Magnetoscop® by scaling it up and realizing a fixed test bench consisting of a much stronger field source, up to 1 T field, and achieving high accuracy levels with the adoption of suitable magnetic sensor technology, such as the Nuclear Magnetic Resonance (NMR). The measured data is post-processed by solving an inverse problem to calculate the relative permeability.

The inverse-problem approach has been recently investigated in the broader framework of magnetic measurements to merge simulations and measurements to obtain a generalized field description. Magnetic measurements suffer from ignorance from model reduction (*i.e.*, neglecting mechanical or thermal effects), approximations deriving from assumptions and ignorance (*i.e.*, linearity of the sensor, non-orthogonal sensors, projection of measurement data onto Fourier polynomials). These problems were addressed in different ways in the literature, by estimating the state of the system through Bayesian inversion [173] or by using hybrid models where the parameters are data-driven updated [174, 175, 176]. Other examples of increasing use of inverse-problem techniques are reported in [177, 178, 179, 180, 181, 182]. In magnetic materials' characterization, this approach has been used in circuit breakers [183], electrical machines [184] or magneto-rheological elastomers [185].

The tool chosen to implement the technique is FE Analysis running on a commercial software tool, COMSOL®. This choice allowed the possibility to import Computer-Aided Design (CAD) drawings and therefore not limit the measurable objects to specimens having regular shapes and easily parametrizable (*i.e.*, cubes, cylinders,

or toroids), but also to exploit the possibility of measuring geometries with more complex shapes, such as finished parts. Moreover, it significantly simplified the implementation of the technique.

6.2.1 Measurement principle

The SSM consists of inserting the test specimen in a highly uniform dipolar magnetic field and mapping the field lines in the proximity of the test specimen, where the field generated by the magnet is perturbed by the stray-field lines generated by the specimen's magnetization. The relative permeability of the test specimen is computed by setting up an inverse problem. The test bench setup is shown in Fig. 6.4.

The magnetic field is mapped twice in the mid-plane of the magnet gap by a local field sensor moved by a linear motor. The first scan is necessary to map the excitation field generated by the magnet, namely the *background field*. The second scan is necessary to map *the perturbed field* in the presence of the test specimen. A second magnetic field sensor is kept in a fixed position and used to monitor and compensate undesired field perturbations related to oscillations in the excitation current.

6.2.2 Mathematical modeling

The geometry and the measured values of the background field are provided as input to a FE model. A magnetostatic model written in terms of reduced magnetic scalar potential formulation [186] is used to perform the simulations. The magnetic field $\mathbf{H}$ is defined as

$$\mathbf{H} = \mathbf{H}_b - \nabla \psi_p, \tag{6.3}$$

where $\mathbf{H}_b = \mathbf{B}_b/\mu_0$, with $\mathbf{B}_b$ the measured background field. ψ_p is the reduced magnetic scalar potential. The total magnetic flux density $\mathbf{B} = \mu_r \mu_0 \mathbf{H}$ must respect Maxwell's equations and be divergence-free. Hence, this yields
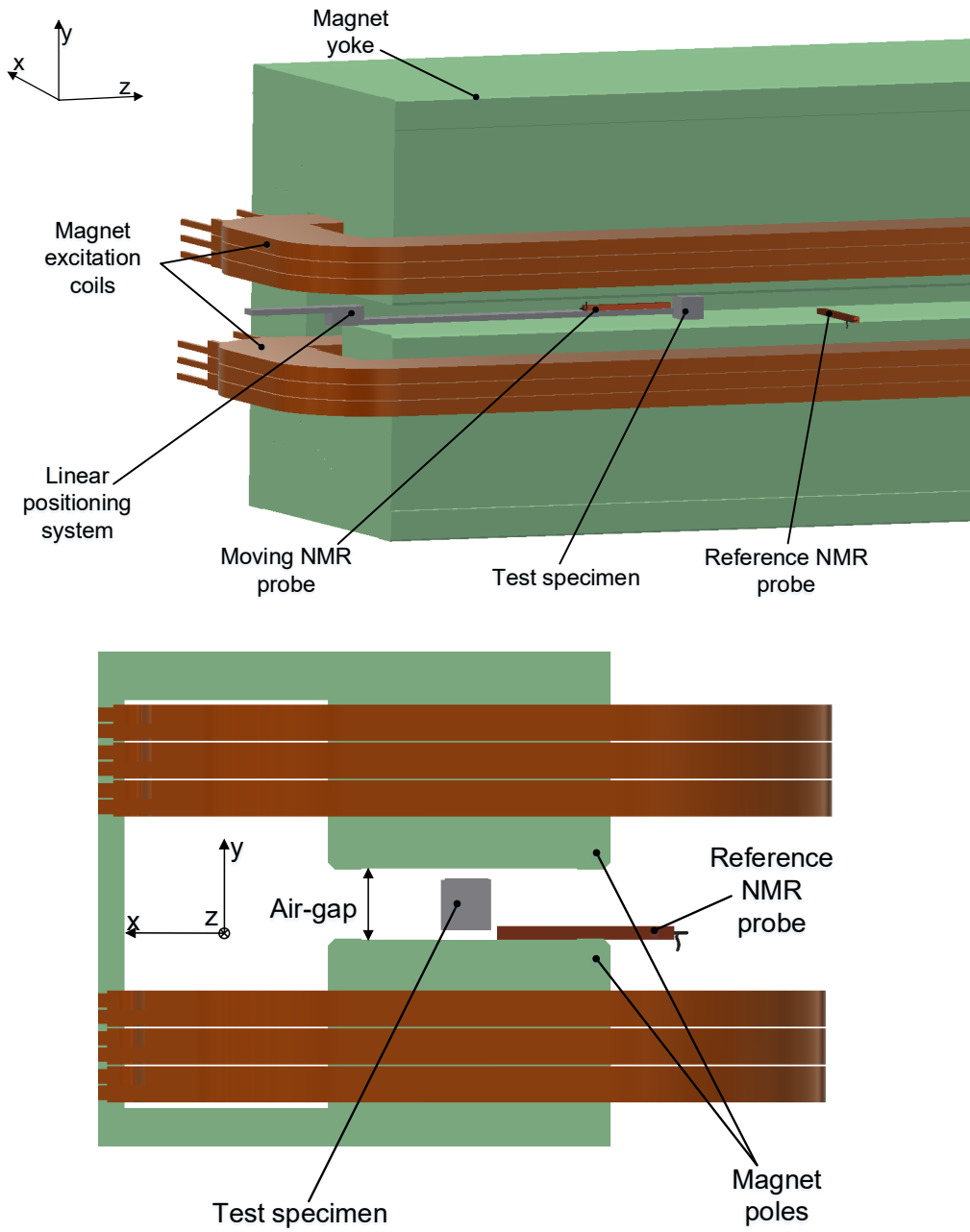
Fig. 6.4 (Top) Layout of the test bench; (bottom) Detail of the magnet gap.

$$\begin{cases} \nabla \cdot [\mu_r \mu_0 (-\nabla \psi_p + \mathbf{H}_b)] = 0 \\ \psi_p = 0|_{S_1} \\ \psi_p = 0|_{S_2} \\ \nabla \psi_p \cdot \mathbf{n} = 0|_{S_{3..6}}, \end{cases} \tag{6.4}$$

where μ_r is the relative magnetic permeability, assumed to be uniform within the specimen. If the test specimen is axisymmetric - *i.e.*, cylinders, toroids, *et similia* - the measurement is done by placing it with its axis perpendicularly to the magnet poles, and a 2D-axisymmetric problem is set up to reduce the simulation time. The background field is assumed to have only the *y*-component and be dependent only on the *z*-coordinate. The other two probe coordinates, (x, y), are measured separately. The geometry elements of the problem are represented in Fig. 6.5.
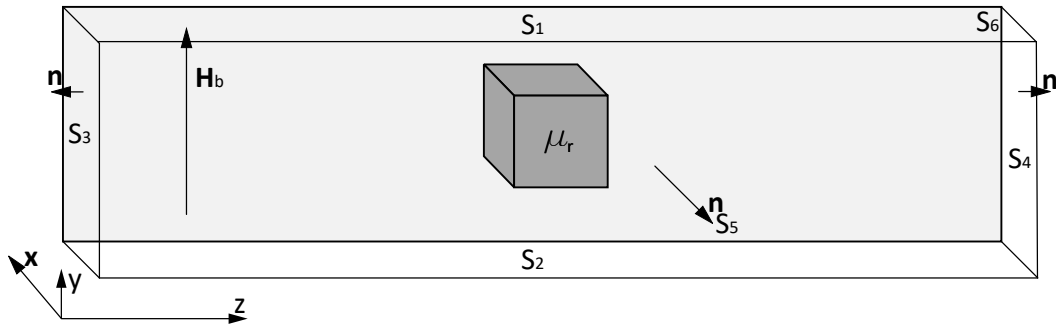
Fig. 6.5 Graphical representation of the domain used for the FE model.

The inverse problem consists of an optimization routine set up to calculate the relative permeability μ_r that minimizes the cost function

$$f(\mu_r) = \sum_{k=1}^{N} |B_m(z_k) - B_s(\mu_r, z_k)|^2, \tag{6.5}$$

where $B_m(z_k)$ are the values of the perturbed field map measured at the positions z_k. The optimization is performed by Levenberg-Marquardt algorithm [187, 188]. The inverse problem algorithm is summarized in the flowchart shown in Fig. 6.6. The problem can be seen as a fitting algorithm of the perturbed field distribution, using the geometry, the background field, and the permeability as input parameters.

The termination criteria of the iterative optimization routine are: $\sqrt{f} \leq 10\ \mu$T or minimum step size $\Delta\mu_r \leq 10^{-6}$. The initial value for the routine does not critically influence the result, and a value of 1, numerically close to typical values of paramagnetic materials, can be chosen. Nonetheless, if a typical value of the material's permeability is known, this can increase the algorithm's convergence rate. Fig. 6.7 provides a visual example of output of the problem. The perturbed field has a non-monotonic profile because the stray field has opposite sign with respect to the background field. After a certain distance, depending on the specimen geometry,
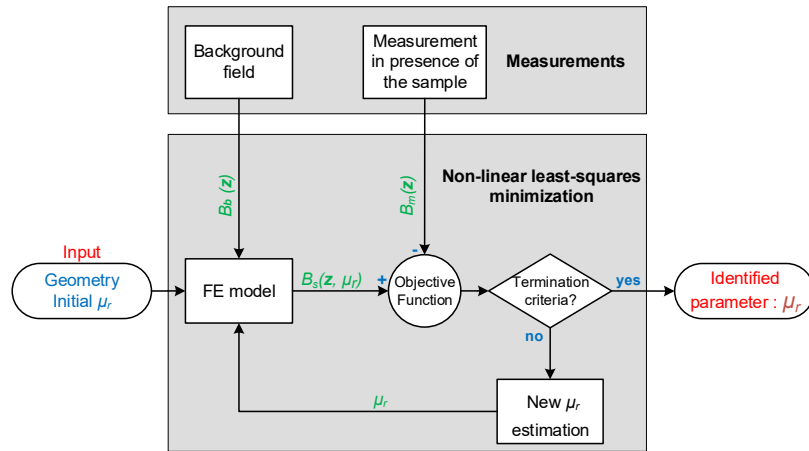
Fig. 6.6 Flowchart of the optimization problem.

the stray field becomes negligible, and the perturbed field becomes parallel to the background field. Different specimen geometries determine different perturbation, or stray field, profiles. For smaller specimen sizes, the slope of the perturbed field is initially higher, but the stray field decays at a shorter distance. Moreover, the relative permeability also influences this profile and increases the distance between the background and perturbed field as its value increases. Different examples of profiles are shown in Chap. 8.

6.3 Hardware and sensor technology

A photograph highlighting the elements in the test bench is shown in Fig. 6.8.

6.3.1 Sensor technology

The implementation of the method relied on the choice of a sensor technology capable of measuring static magnetic fields in the 1 T range with accuracy better than 100 μT. Owing to these requirements, the adopted sensor technology was the NMR, as also shown in Fig. 6.4 and Fig. 6.8. In particular, a commercial sensor, the NMR Pt2025 from Metrolab [189] was used. The sensor has a declared accuracy of 5 ppm and a resolution of 0.1 μT, allowing accurate detection of the field perturbation. Two types of probe are used for the measurements: a 1080-probe type 4 and type 2,
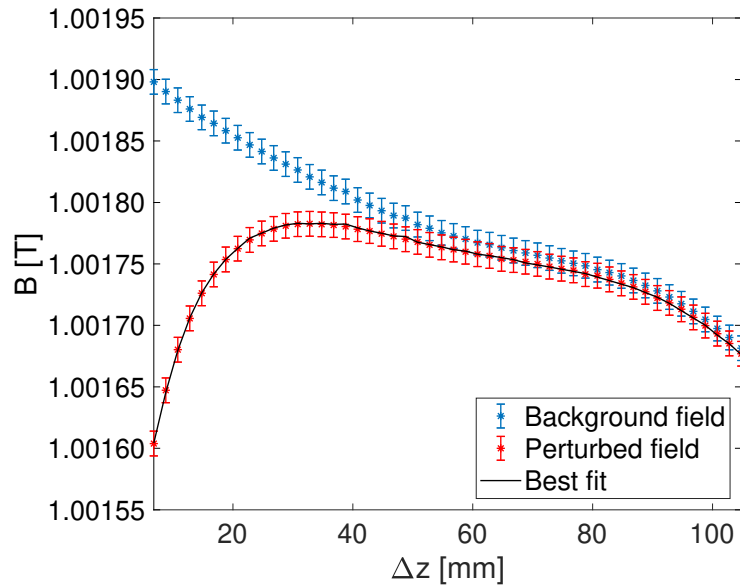
Fig. 6.7 An example of the two field scans performed for the characterization of AISI 310S at a test field of 1 T, the background field (blue) and the perturbed field (red) respectively. The computed relative permeability is μ_r=1.00283. In black, the simulated field calculated using the computed permeability, which best fits the perturbed field.
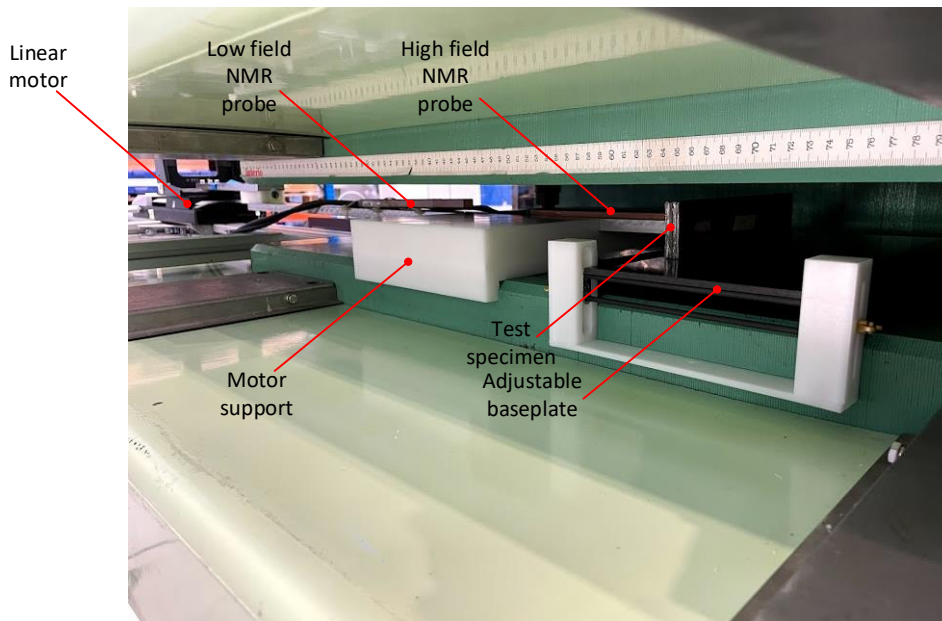
Fig. 6.8 A detail photograph of the elements of the test bench.

having respectively range of [0.35 1] T and [0.09 0.26] T, to cover the field ranges [0.1 1] T.

Fig. 6.9 A photograph of the NMR Metrolab Pt2025 from [189].

Other sensor technologies would have presented poor performance for this application. Although having a good range of operation, Hall probes present poor accuracy for this kind of applications, generally higher than 10^{-5} [190]. Magnetoresistive sensors (*e.g.*, Anisotropic Magneto-Resistance (AMR), Giant Magneto-Resistance (GMR)) are non-linear, display hysteresis, and they typically saturate at fields of a few tens of mT [191]. Fluxgate sensors have a limited range of operation (1 mT) [192]. Sensing coils are a good alternative and can reach 10 μT of accuracy when combined with high-quality electronics and properly calibrated, but they would require a more complex layout to measure the field map (*i.e.*, translating fluxmeter [193]).

6.3.2 Linear positioning system

A linear positioning system PI M-511.DG [194] was used to move the NMR probe and map the field over a length of 100 mm. The positioning of the probe and the correct movement along the magnet profile, parallel to the pole, was verified by using a Leica Absolute Tracker AT930 [195].

6.3.3 Field source

The field source was a normal-conducting dipole magnet having a linear transfer function of about 316 A/T in the 0-1.2 T range and homogeneity in the order of 10^{-5} T. The magnet length is 2.5 m, the air-gap is 80 mm, and the pole width is

Fig. 6.10 A photograph of the PI linear positioning system from [194].

240 mm. The magnet is degaussed and pre-cycled ten times between 0 and 320 A to bring it on a stable hysteresis loop, and obtain a repeatable response, within 8 ppm. Finally, the field amplitude is decreased in a step-like fashion, and the two field scans are performed in correspondence with each step. A Keithley 2700/7700/E Digital Multimeter [196] was used to monitor the magnet current.

Fig. 6.11 A photograph of the dipole magnet used as a field source.

A field map of the magnet measured by NMR sensor at the nominal current of 316 A is shown in Fig. 6.12. The probe spans a total length included in a region between z=600 mm and z=700 mm.
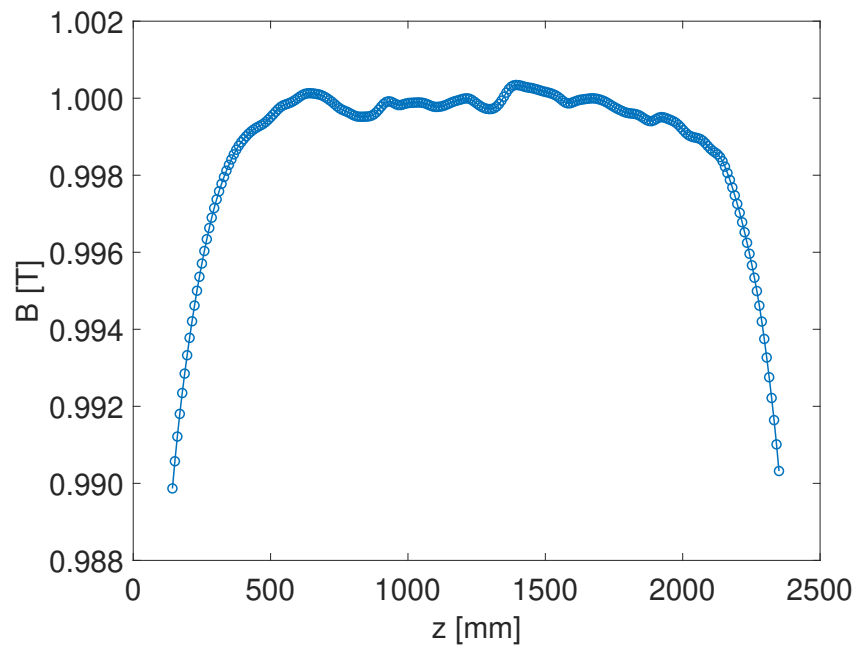
Fig. 6.12 Field map of the dipole magnet measured by NMR sensor.

Chapter 7

Metrological characterization

This Chapter presents the metrological characterization of the SSM and summarizes the uncertainty sources. Some of these uncertainty sources originate from simplifications and model-order reduction resulting from *a priori* assumptions, constituting a source of deterministic errors. Some were verified and considered negligible, while others were taken into account and compensated. All of these uncertainty sources are then propagated throughout the model by using the Monte Carlo analysis [197], the results of which are presented in Chap. 8 for the first two case studies. Part of the content presented in this Chapter was also previously published in [P5].

7.1 Summary of the uncertainty sources

The uncertainty sources are summarized in Fig. 7.1 and can be classified in:

- Measurement uncertainties

- Modeling uncertainties

The measurement uncertainties originate from the measurement process, and they arise from the field map measurements, the test specimen and the probe positioning, and the test specimen dimensions. The modeling uncertainties depend on the model's accuracy used to fit the measurements. The accuracy of the model described by Eq.(6.4) depends on three main contributions: geometrical uncertainties, field description assumptions, and neglecting the background field variations. An
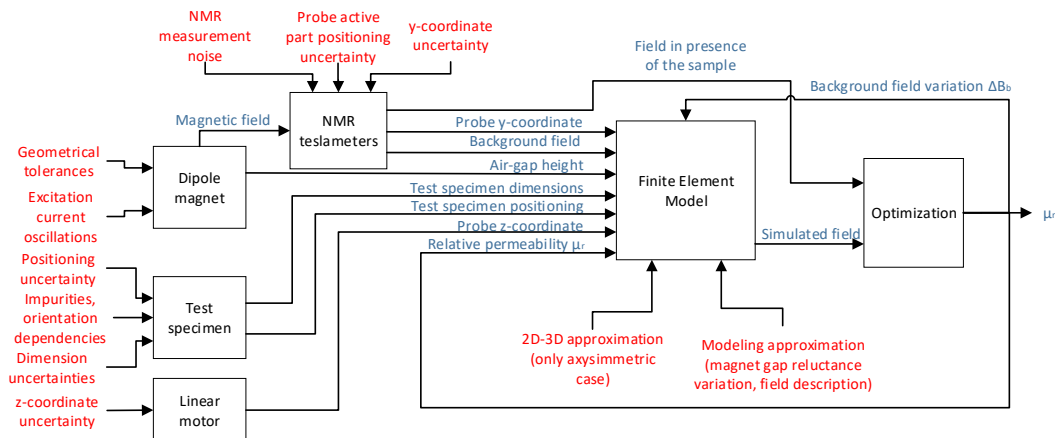
Fig. 7.1 Summary of the uncertainty sources of the static-sample magnetometer. In blue, the measurement parameters with their uncertainty and; in red, the uncertainty sources.

additional contribution is modeling the specimen under test as isotropic and with uniform permeability distribution within its volume.

7.2   Measurement uncertainties

As specified in Sec. 6.3.1 the field map is measured with an accuracy of 5 ppm using the NMR sensor. The uncertainty of the probe positioning is the uncertainty of the positions (z, y) where the field values are measured. This uncertainty originates from multiple contributions:

- Position of the active element within the NMR probe, known from the datasheet and having a declared accuracy of 0.5 mm.

- Linear motor positioning uncertainty, influencing only the z-coordinate, and having an accuracy of 10 μm. Nevertheless, given the position uncertainty of the active element within the probe, the accuracy of the z-coordinate is 0.5 mm. Systematic contributions along the other two axes were made negligible by verifying the motor alignment with the magnet poles with a laser tracker.

- Distance between the probe and magnet lower pole, measured with an accuracy of 20 μm, influencing only the y-coordinate. Similarly to the z-coordinate, given the position uncertainty of the active element within the probe, the accuracy of the y-coordinate is 0.5 mm.

The specimen distance from the lower pole is measured with an accuracy of 20 μm by measuring the height of the specimen's baseplate with a digital caliper. The specimen's dimensions are modeled with an accuracy of 20 μm, if regular shapes such as cubes and cylinders are adopted, measured using a digital caliper.

7.3 Modeling uncertainties

7.3.1 Geometry

The geometrical uncertainties are the uncertainties of the domain geometry used for the FE analysis. The length of the domain (z-axis) is equal to the scan length and, therefore, has the same uncertainty of the linear motor position. The height of the domain along (y-axis) is equal to the air-gap length, known with an accuracy of 0.1 mm. Finally, the depth of the domain (x-axis) is equal to the pole width, known with an accuracy of 0.1 mm.

The other three sources of modeling uncertainties are respectively described in Sec. 7.3.2, Sec. 7.3.3 and Sec. 7.3.4.

7.3.2 Field description approximation

The measurement principle relies on scanning the field along the z-axis and assuming the field as constant along with the other two directions, x and y. However, the dipole field can be considered homogeneous only to a certain extent in the gap volume. Hence, the validity of the approximation needs to be verified. Fig. 7.2 shows a representation of the field distribution in the transverse plane of the magnet, (x, y). The field quality is represented by the parameter Q, defined as

$$Q = \log_{10} \left| \frac{\bar{B}_y(x, y) - \bar{B}_y(0, 0)}{\bar{B}_y(0, 0)} \right|, \tag{7.1}$$

where $\bar{B}_y$ is the vertical component of the integrated field. The field was reconstructed by boundary element methods from measurements performed by single-stretched wire [193].
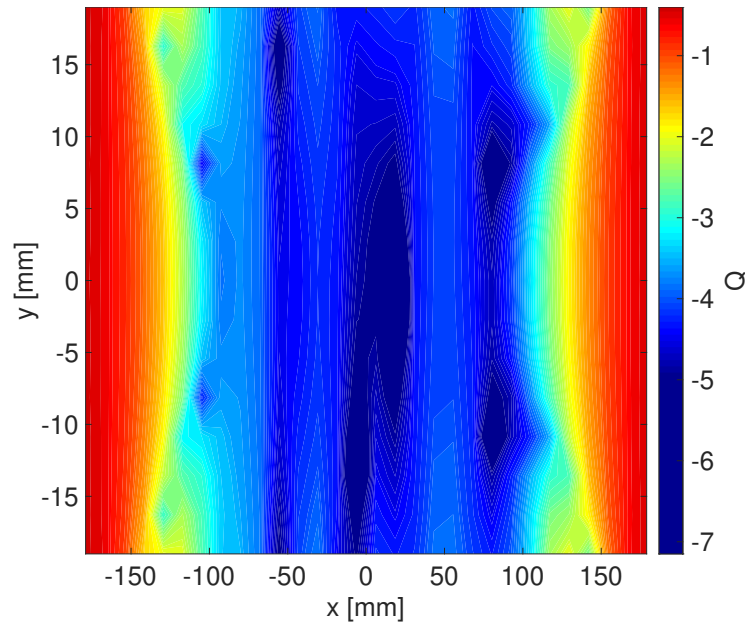
Fig. 7.2 Integrated field quality in the dipole magnet used for the experimental setup [193].

From Fig. 7.2, it results that the test specimen dimensions shall not exceed 200 mm along the *x*-axis. Along the *y*-axis, data are limited to an interval of ± 20 mm, corresponding to a half gap length. However, it was experimentally verified that the height of the specimen should not exceed 60 mm. Moreover, attention shall be paid to carefully placing the specimen in the magnet center within a few mm.

7.3.3   Background field variations

Background field variations are a source of systematic uncertainties that shall be compensated and have origin in two different causes. The main one is the air-gap reluctance variation due to the insertion of the specimen in the magnet gap. This variation is physically caused by a change in the saturation state of the magnet yoke, made of a ferromagnetic material and not modeled because only the air-gap region is taken into account. This variation can be measured at the maximum distance from the specimen reachable by the motor, where the perturbation is expected to be zero if calculated using the model. At distances higher than twice the scan length (200 mm), this effect is not detectable and cannot be measured by the reference NMR. This deterministic error is not *a priori* known because it depends on the relative permeability and the specimen dimensions, and if not compensated, it would lead

to an overestimation of the permeability and poor convergence of the optimization algorithm. A visual example is shown in Fig. 7.3.
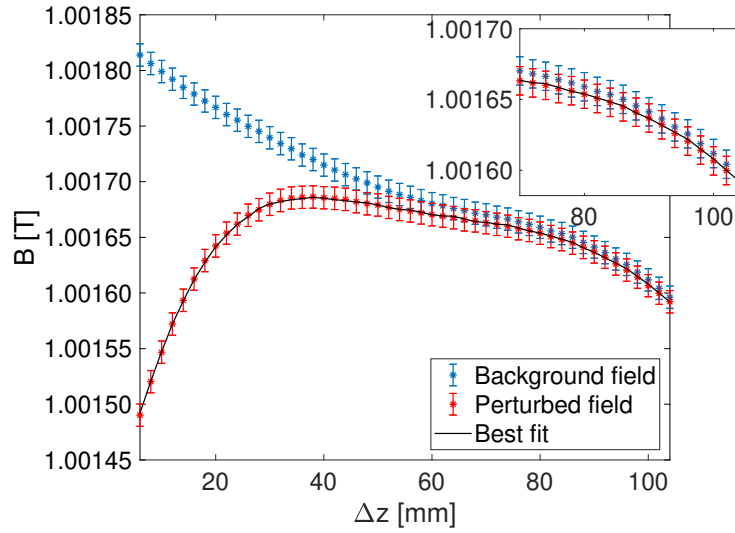
Fig. 7.3 Field profiles for a bulk cube made of AISI type 316, having 50 mm side. Computed permeability $\mu_r =$1.00304. The zoom highlights a background field variation of 4.1 μT in the far-field region.

The total background field variation ΔB_b is therefore corrected by introducing a second optimization variable to be used as a correction term, having an initial value of

$$\Delta B_b = B_b(\Delta z_{max}) - B_m(\Delta z_{max}). \tag{7.2}$$

This initial value is chosen because ΔB_b should be ideally zero. The modified cost function becomes

$$f(\mu_r, \Delta B_b) = \sum_{k=1}^{N} |B_m(z_k) - B_s(\mu_r, \Delta B_b, z_k)|^2. \tag{7.3}$$

Although much less important, the other contribution is due to low-frequency current oscillations arising from the power converter instabilities. These current oscillations determine field oscillations in the order of a few ppm. These small field variations can be measured by the reference NMR sensor and linearly compensated.

7.3.4 Impurities and orientation dependencies

A simplification introduced in the model used to compute the relative permeability from the field scans is the assumption that the specimen under test is isotropic and with uniform permeability distribution within its volume.

Neglecting the orientation dependencies may be seen as a consequence of the approximation introduced in the field description, where the field is assumed to have direction only along the y-axis because the output of the NMR sensor provides only the field module, and the measurement is performed in a dipole magnet, where the B_y component prevails over the other two. Therefore, if the relative permeability is represented by the tensor

$$\mu_r = \begin{bmatrix} \mu_{rxx} & \mu_{rxy} & \mu_{rxz} \\ \mu_{ryx} & \mu_{ryy} & \mu_{ryz} \\ \mu_{rzx} & \mu_{rzy} & \mu_{rzz} \end{bmatrix}, \tag{7.4}$$

the terms outside the second column cannot be evaluated from a single measurement. Moreover, the terms μ_{rxy} and μ_{rzy} cannot also be evaluated for the same reason. The approximation can be considered as valid because the material is isotropic in most cases. If three measurements are performed, the relative permeability tensor can be written as

$$\mu_r = \begin{bmatrix} \mu_{rxx} & 0 & 0 \\ 0 & \mu_{ryy} & 0 \\ 0 & 0 & \mu_{rzz} \end{bmatrix}, \tag{7.5}$$

and the three single components on the diagonal can be evaluated separately by rotating the specimen three times accordingly. If the test specimen is isotropic

$$\mu_{rxx} = \mu_{ryy} = \mu_{rzz} = \mu_r. \tag{7.6}$$

However, a bulk specimen cannot be provided in most cases because the main material batch generally consists of a coil with a few mm of thickness or lower. The test specimen is assembled in this condition by cutting multiple strips from the coil, stacking them, and gluing them with Epoxy resin. This process inevitably creates air gaps between the strips and determines an intrinsic anisotropy. The overall effect

of the air gaps determines an underestimation of the relative permeability that can be compensated by simply taking into account the stacking factor or canceled by placing the test specimen accordingly in the magnet gap as shown in Fig. 7.4.
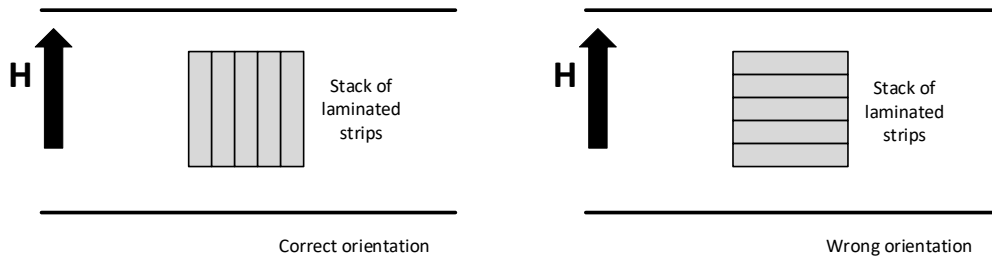
Fig. 7.4 (Left) Correct specimen orientation when using stacks of laminated strips and; (right) Wrong orientation

The spatial distribution of the permeability within the specimen's volume is considered uniform, and no alternative assumptions can be made, because it would require the knowledge of how the impurities are distributed within the material volume. This information can only be assessed by cutting different specimens of smaller size and measuring them by VSM.

7.3.5   Specimen preparation

The specimen preparation might impact the measured permeability if not done properly, especially if this is austenitic stainless steel. As seen in Sec. 1.4.4, austenite is a non-ferromagnetic phase, which determines the typical low permeability of these stainless steels. The specimen cut from the main material slab can introduce a content of ferromagnetic phase. If the machining is performed at cold, martensite precipitations can occur. For precise specimen cut, Electrical Discharge Machining (EDM), also called *spark erosion*, is used to have a precision better than 0.1 mm. However, the cut is performed at temperatures much higher than 1000 °C, and degrades the surface leaving traces of δ-ferrite and oxides. The resulting effect is similar to welding, and leads to an increase of permeability.
Fig. 7.5 shows an example of analysis carried out on a specimen of AISI type 316, having 2 mm diameter and 6 mm height, to be measured by VSM. The analysis was carried out by Focused Ion Beam (FIB) combined with Scanning Electron Microscope (SEM) (FIB-SEM).

(a) Scheme of the FIB cross-section location

(b) 200 μm view

(c) 20 μm view and estimation of the affected layer

(d) 10 μm view
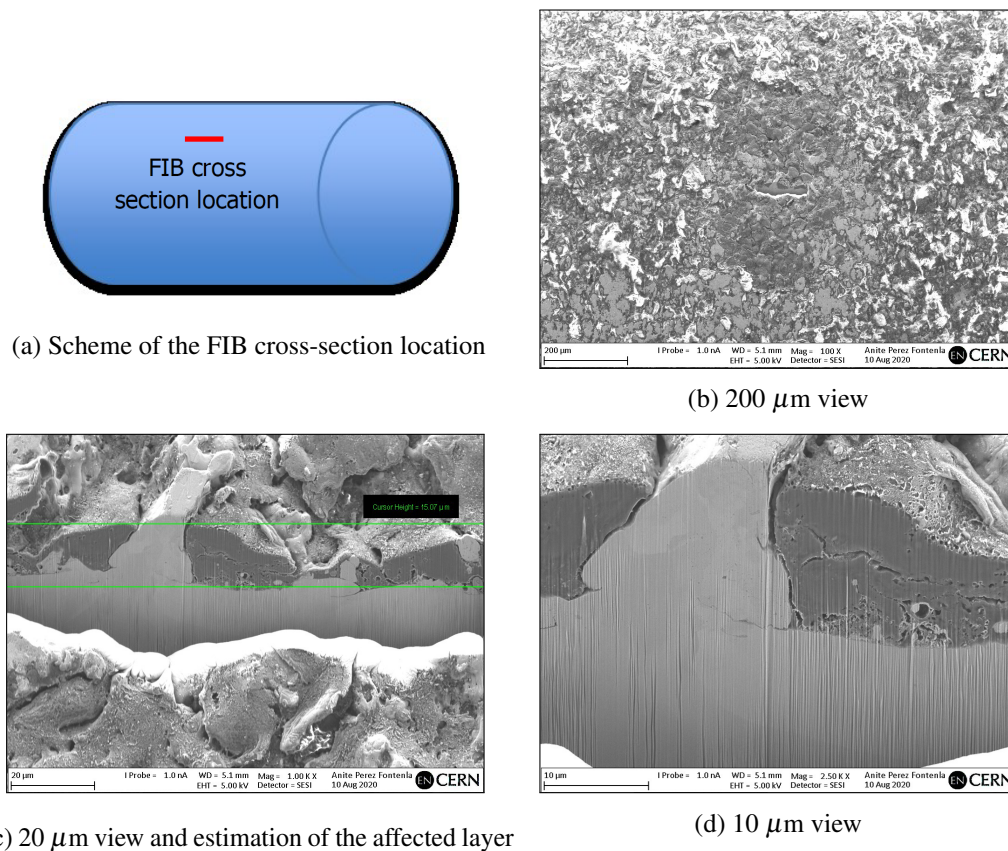
Fig. 7.5 SEM images on representative EDM surface of the cylinder [courtesy of A. Perez Fontenla [198]].

This layer having 15 μm thickness, made principally of C, Fe, Mo, and O, greatly affected the relative permeability given the low surface-to-volume ratio. Fig. 7.6 shows how the degraded layer impacts the magnetic permeability, which increases significantly. The same test specimen was measured as cut (blue), after partial polishing and removing a mass of 3 mg of material (red) and after completely removing the 15μm layer (yellow). Performing this operation determines a decrease of magnetic susceptibility of about 10 %. The impact can be considered negligible for the bulky test specimens typically used in the SSM. For comparison, the permeability measured on a fourth specimen, a cube having a 50 mm side obtained from the same material slab and cut by EDM was plotted. This specimen does not show the same permeability increment because it has a higher surface-to-volume ratio, which makes negligible the impact of the degraded layer.

In conclusion, the specimen's preparation shall be carried out carefully to avoid biasing the measurement results. In particular, if the specimen is cut by EDM, careful

attention shall be paid to the surface finishing. Water-jet cutting is an excellent alternative to EDM and does not present these side effects.
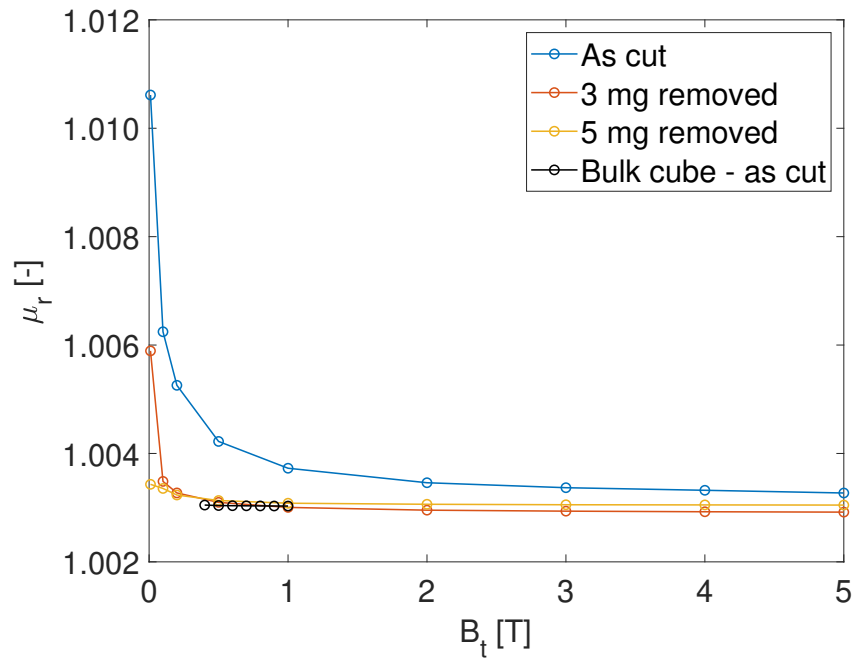
Fig. 7.6 Comparison of relative permeabilities as a function of the test field measured on an AISI type 316 specimen before (blue), after removal of 3 mg of material (red), after removal of 5 mg of material, corresponding to the 15 μm layer (yellow). In black, the results obtained by SSM without surface finishing.

Chapter 8

Experimental results

In this Chapter, three case studies are presented to showcase the performance of the proposed method. The first one consists of the magnetic characterization of 10RM18, an austenitic stainless steel alloy with permeability lower than conventional stainless steel (*i.e.*, AISI 300 series) and used to realize the magnet collars to be installed in the new HL-LHC magnets. The uncertainty was assessed by Monte Carlo analysis, and the results were validated by comparison with the VSM.

The second case study consists of the magnetic characterization of twelve specimens of Pure tungsten Heavy Alloy (WHA) ASTM B-777 class 3, used in radiation shielding applications. The goal of this case study is to show the performance of the method on extremely low permeability materials, having $\chi_m \approx 10^{-5}$. Also, in this case, the uncertainty analysis was carried out by Monte Carlo simulations, and the results were validated by comparison with the VSM.

Finally, the third case study consists of the magnetic characterization of two steel grades of AISI type 316L, used for the bellows to be installed in the HL-LHC cryomodules to manage the transition between regions at two different temperatures. This case study shows how the method can be used to measure finished parts. The results were validated by comparison with the relative permeability of the raw material, measured separately. Part of the results presented in this Chapter was also previously published in [P5].

8.1 Characterization of an austenitic stainless steel for the HL-LHC superconducting magnets' collars

8.1.1 Context

In the superconducting magnets installed in the LHC, the coils are held in place by mechanical force-restraining structures called collars, made of stainless steel. Such force-restraining structures are installed to minimize conductor movements during the powering of the magnet [9], preserve the exact location of the cables, which strongly influences the field quality [199], and avoid events of superconductor quench triggered by movements [200]. A photograph of a collar lamination used for the LHC magnets is shown in Fig. 8.1.

Fig. 8.1 A photograph of a collar lamination used in the LHC superconducting magnets.

The selection of the collars' steel is crucial because its magnetic permeability can influence the field quality of the magnet. The LHC collars were made of a material known under the trade name YUS 130S, from Nippon Steel & Sumikin Stainless Steel Corporation (NSSC). The permeability was measured in [59] by VSM at 4.2 K, obtaining a relative permeability lower than 1.003 for fields greater than 0.1 T. At room temperature, the permeability was assessed using the Foerster Magnetoscop®, obtaining a value in the range 1.0015-1.0020. In [9], the effect of the collars' permeability was assessed on the large aperture quadrupole magnets for the LHC (MQY), and the results showed that the impact is significant at room temperature and low currents, where the collars' permeability value can increase up to 1.04, and thus not strictly respect the specification of $\mu_r < 1.005$. However, the impact of the collars' permeability on the field quality is negligible at high fields because the relative permeability decreases to 1.003.

For the high luminosity upgrade of the LHC, the new collars will be realized with a
new advanced stainless steel, 10RM18, developed from Sandvik AB. The goal of this
case study is to assess if the permeability values respect the requirement $\mu_r < 1.003$.
To this aim, two different test specimens were realized:

- A cube of 60 mm side built by stacking 20 laminations of 3 mm thickness
  each.

- A stack of 6 toroids having 114 mm of outer diameter, 105 mm of inner
  diameter and 3 mm thickness each. The toroids were initially intended to be
  measured using the flux-metric method for cross-comparison.

The laminations were cut from the main material slab by EDM and glued with
epoxy resin. The two specimens are shown in Fig. 8.2, and the results are reported in
Sec. 8.1.2.

Fig. 8.2 10RM18 test specimens.

8.1.2 Results and discussion

Fig. 8.3 shows the background and the perturbed field profiles for the two specimens,
evaluated at a test field of 1 T.

As previously mentioned in the example of Sec. 6.2.2, the perturbed field has
a non-monotonic profile because the stray field - or equivalently the perturbation -
generated by the specimen magnetization points against the background field. The
perturbation decays at a distance of about 60 mm and becomes negligible. The
background field variation resulting from the change of the air-gap reluctance is
3.9 μT for the cube case and 0.2 μT for the toroids. These two values are different
because the cube volume is two orders of magnitude higher than the toroids'. The
perturbed field values are similar near the air-specimen interface because they are

(a) Cube, $\mu_r = 1.00187$ (b) Toroids, $\mu_r = 1.00185$
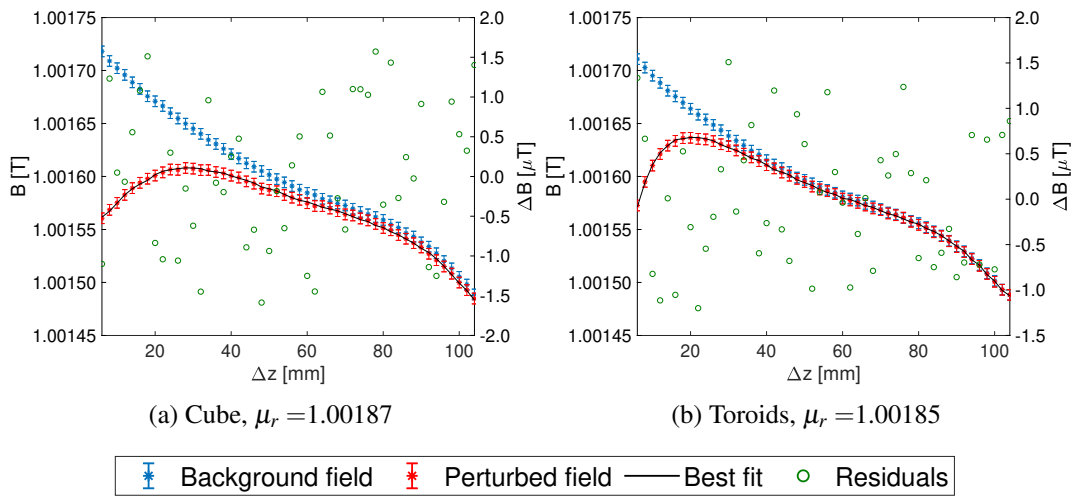
Fig. 8.3 Field profiles for the two 10RM18 test specimens at the test field B_t=1 T as a function of the distance from the specimen Δz. In blue, the measured background field; in red, the perturbed field; in black, the simulated field; and in green, the fit residuals, displayed on the right vertical axes.

dependent mainly on the specimen permeability. However, the two perturbations decay differently: the slope is higher initially for the smaller specimen size, but the perturbation damps on a shorter distance (40 mm for the toroids, 60 mm for the cube). The distribution of the residuals is approximately gaussian and has an RMS value of 0.8 μT and 0.7 μT, respectively, for the two cases. Compared with the 5 ppm accuracy of the field measurements, these values indicate a suitable fit quality. Fig. 8.4 shows the measurement results consisting of the measured relative permeability values as a function of the applied magnetic field. The results obtained by measuring the material by VSM are plotted for comparison.

The reported values are obtained by averaging four consecutive measurements. The toroid stack presents a lower permeability value at 1 T than the cubic specimens. On the other hand, its sensitivity on the applied field is higher due to a higher percentage of ferromagnetic phase in the material volume: in fact, no surface finishing was performed, and being the specimen volume two orders of magnitude lower than the cube, the impact of the EDM cut was more significant. The measured values are in agreement with the VSM values. In particular, the permeability profile in the cube case is practically identical to the VSM measurement. Their difference in permeability can be explained by a non-uniform distribution of permeabilities in the main material slab.
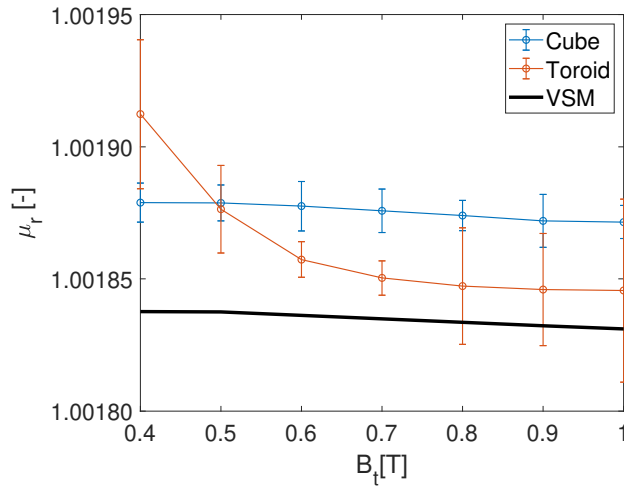
Fig. 8.4 Measured relative permeability values for the 10RM18 specimens as a function of the magnetic field, with their repeatability bars, compared with the VSM measurement.

Fig. 8.5 shows the results of the Monte Carlo simulations performed for a test field of 1 T. The analysis was performed by running 3000 simulations. The numerical results are also reported in Table 8.1.

(a) Cube, $p = 30.6\ \%$ (b) Toroids, $p = 73.9\ \%$

Fig. 8.5 Results of the Monte Carlo simulation for the two cases corresponding to the curves shown in Fig. 8.3. (Thick dashed line) Average value and; (thin dashed lines) Interval corresponding to a 95 % level of confidence

The two distributions are approximately gaussian. The hypothesis of gaussian distribution was verified through a χ^2-test at a 5 % significance threshold. The p-values are reported in the captions of Fig. 8.5. The standard deviation values are 2 % and 4 % of the measured susceptibility. The standard deviation is higher in the

Table 8.1 Monte Carlo simulation results for the estimation of the relative permeability of the two stainless steel specimens and the intervals for a 95 % of level of confidence.

Sample	Average value	Std. Deviation	Coverage interval (95 %)
Cube	1.001873	0.000043	[1.001788 1.001952]
Toroids	1.001847	0.000067	[1.001719 1.001975]

case of the toroids because the probe and the specimen positioning uncertainties impact more in terms of sensitivity, given the lower dimensions. Fig. 8.6 shows the compatibility between the measured VSM value and the SSM values at 1 T, including their 95 % confidence interval.
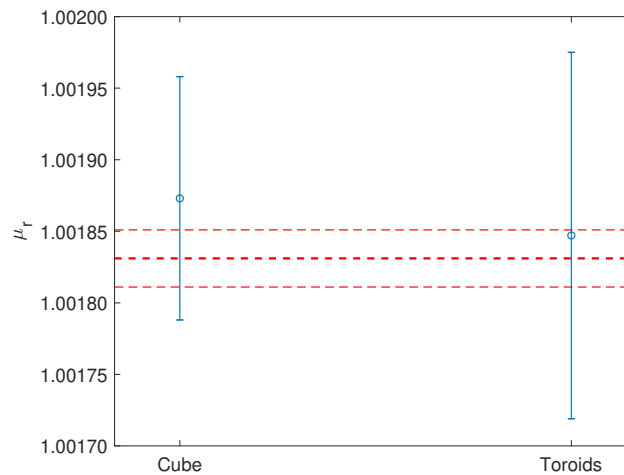
Fig. 8.6 Comparison of the measurement results for the two stainless steel specimens at a test field of 1 T. In blue, the values and coverage intervals obtained by SSM as a result of the Monte Carlo simulations. In red, the reference value measured by VSM (thick dashed line) and the coverage interval (thin dashed line), corresponding to a 95 % of level of confidence.

The compatibility between the SSM measured values, and the VSM proves that the method has similar performance to the state-of-the-art, although the SSM shows a higher uncertainty. This higher uncertainty might indicate an overestimation because the Monte Carlo simulations were performed in a worst-case scenario adopting type-B uncertainty sources, with values from the instrumentation datasheet, and characterized as uniform distributions following the GUM guidelines. The source of uncertainty that impacts the most on the final result is the probe positioning. This parameter was set with an accuracy of 0.5 mm from the NMR datasheet, and it could not be measured with higher accuracy because the active element within the probe cannot be accessed without compromising the probe integrity.

8.2 Characterization of a heavy tungsten alloy for radiation shielding from collision debris

8.2.1 Context

Heavy tungsten alloys are commonly used in radiation shielding applications [201, 202, 203], especially when the lead is not a feasible option and size reduction needs to be achieved. Their density is about 18 g/cm^3 against the about 11 g/cm^3 of lead. In particle accelerators, tungsten alloys are generally used to shield elements of the machine to prevent the synchrotron radiation from damaging them. Examples are beam screens, in order to protect the superconducting magnets, operating around the intersection points, from collision debris and minimizing the synchrotron radiation [204, 205].

Fig. 8.7 A photograph of a beam screen for HL-LHC (© 2018 CERN). The tungsten insert is highlighted in red.

The case study presented in this subsection is dedicated to the measurement of a heavy tungsten alloy, WHA ASTM B-777 class 3 [206], used for the realization of radiation protection elements to prevent debris from the collimators to cause long-term radiation damage to the warm magnets of the LHC Betatron Cleaning Insertion [207, 208]. As these elements should be ideally non-magnetic, the requirement was to verify that $\mu_r < 1.005$.

To this aim, 12 cylinders of 35 mm diameter and 25 mm high, shown in Fig. 8.8, were provided. The measurement results are reported in Sec. 8.2.2
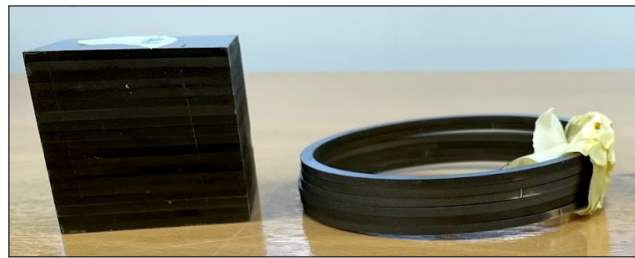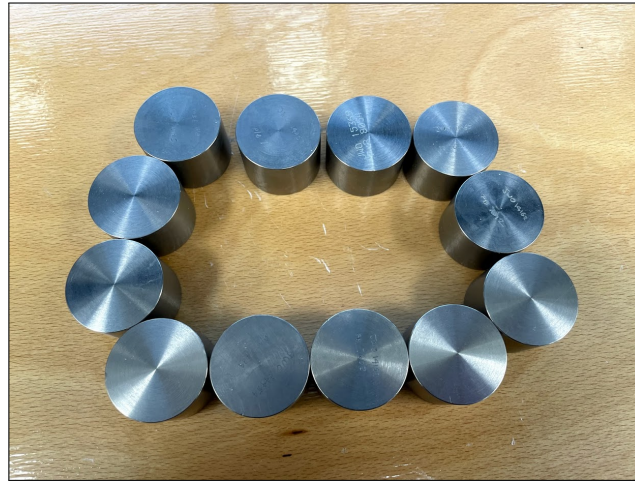
Fig. 8.8 Heavy tungsten alloy test specimens.

8.2.2   Results and discussion

Fig. 8.9 reports the background and the perturbed field profiles for the first two specimens, evaluated at a test field of 1 T. The computed permeability value is 1.00009 for both cases.
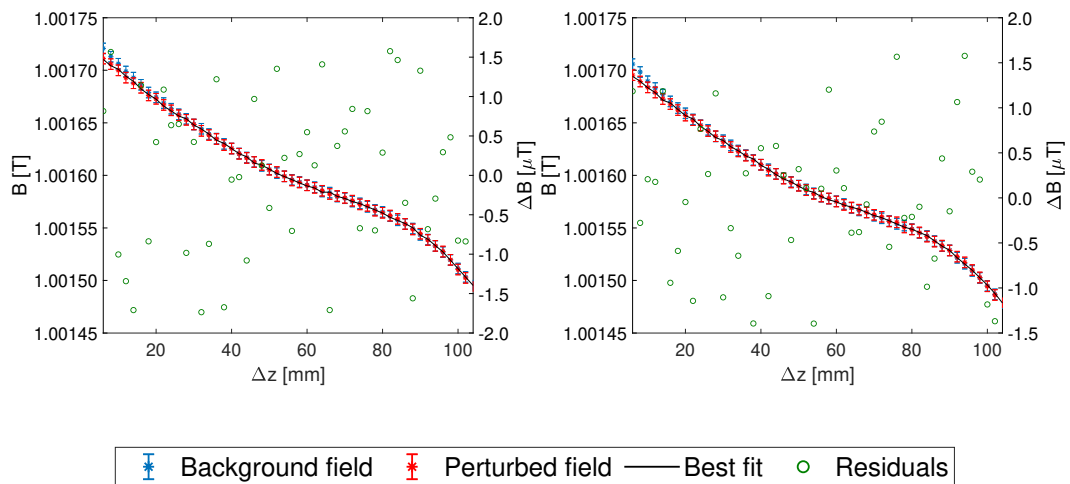
Fig. 8.9 Field profiles for the specimens JWO14159 (left) and JWO15369 (right) at the test field B_t=1 T as a function of the distance from the specimen Δz. In blue, the measured background field; in red, the perturbed field; in black, the simulated field; and in green, the residuals, displayed on the right vertical axes.

In contrast with what was shown for the 10RM18 alloy in Sec. 8.1.2, the perturbed field profiles when measuring a specimen with such a low permeability do not

change significantly from the background field, which means that lower permeability materials (*i.e.*, aluminum) would need to be measured on a specimen with higher volume to increase the Signal-to-Noise Ratio (SNR). For the same reason, no significant variation of background field due to the change of air-gap reluctance was detected. The distribution of the residuals is approximately gaussian and has an RMS value of 1.0 μT and 0.8 μT, respectively. Fig. 8.10 shows the measurement results consisting of the measured relative permeability values as a function of the applied magnetic field. The results obtained by measuring the material by VSM are plotted for comparison.
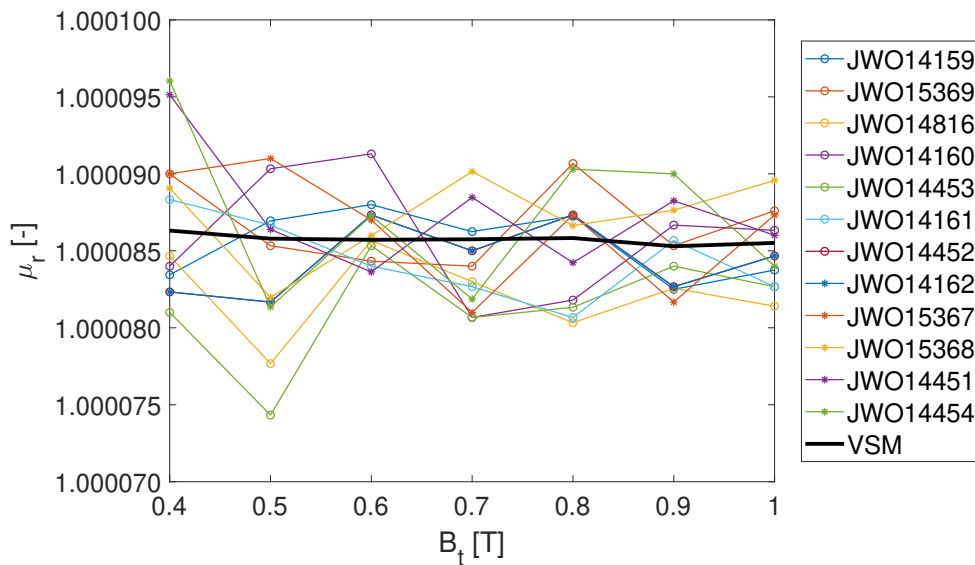
Fig. 8.10 Measured relative permeability values for the tungsten alloy specimens as a function of the magnetic field.

Being the alloy nominally made of 95 wt.% of tungsten [206], the relative permeability was expected to have little dependency on the applied field and the measurement results confirm this. The reported values are obtained by averaging three consecutive measurements. The standard deviation of these measurements $\sigma \leq 10^{-5}$ for $B_t >$0.5 T and $\sigma \leq 2 \times 10^{-5}$ for $B_t \leq$0.5 T. The VSM values have a standard deviation $\sigma \approx 10^{-6}$.

Fig. 8.11 shows the results of the Monte Carlo simulations performed for the first two test specimens at a test field of 1 T. The analysis was performed by running 3000 simulations. The numerical results are reported in Table 8.2.

(a) JWO14159, $p = 4.5\,\%$ (b) JWO15369, $p = 3.4\,\%$
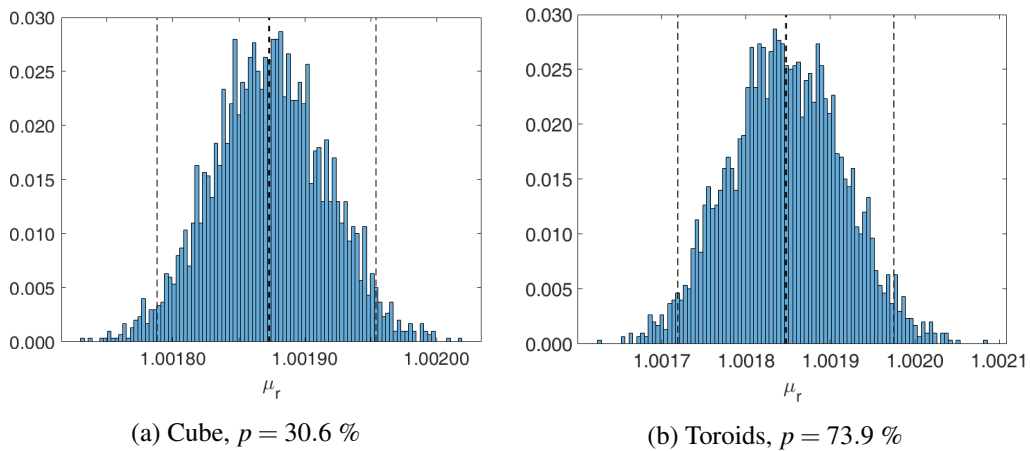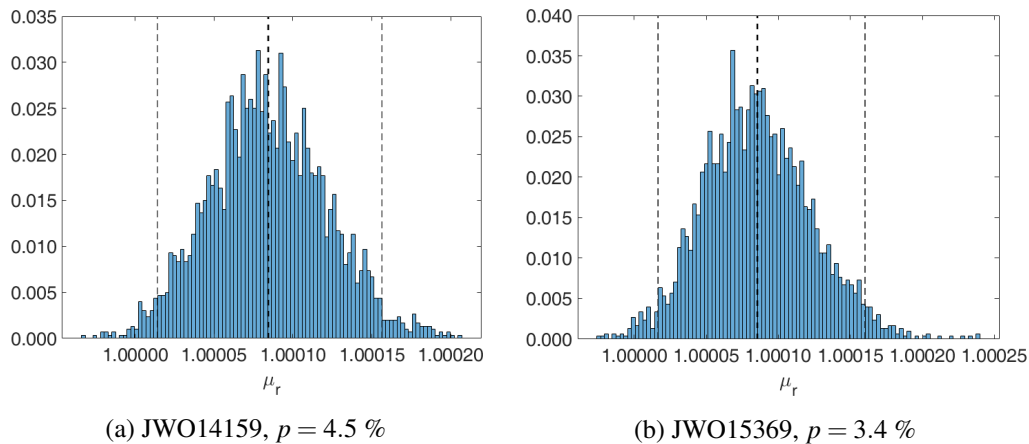
Fig. 8.11 Results of the Monte Carlo simulation for the two cases corresponding to the curves shown in Fig. 8.9. (Thick dashed line) Average value and; (thin dashed line) Interval corresponding to a 95 % level of confidence

Table 8.2 Monte Carlo simulation results for the estimation of the relative permeability of the two tungsten alloy specimens and the intervals for a 95 % of level of confidence.

Sample	Average value	Std. Deviation	Coverage interval (95 %)
JWO14159	1.000084	0.000037	[1.000014 1.000156]
JWO15369	1.000085	0.000037	[1.000016 1.000160]

The results of the χ^2-test at a 5 % significance level led to the conclusion that the distributions are not gaussian. The p-values are reported in the captions of Fig. 8.11. This outcome is also clearly visible from the right-skewed histograms. This asymmetry may be explained by a permeability value extremely close to 1. In fact, from the experimental data shown in Fig. 8.9, $B_m \leq B_b$ and therefore it must be $\mu_r \geq 1$. Therefore, the permeability values converge to 1 rather than to values lower than 1.

Fig. 8.12 shows the compatibility between the measured VSM value and the SSM values at 1 T, including their 95 % confidence interval.

The relative uncertainty is higher (44 % of the measured susceptibility) than in the previous case study. However, in contrast with the previous case study of Sec. 8.1.2, the SSM measurements are in better agreement with the VSM results. This counterintuitive outcome may result from different factors. A first justification is that the alloy is more chemically pure and uniform, and therefore specimen-to-specimen repeatability is better guaranteed. Moreover, given the low permeability,
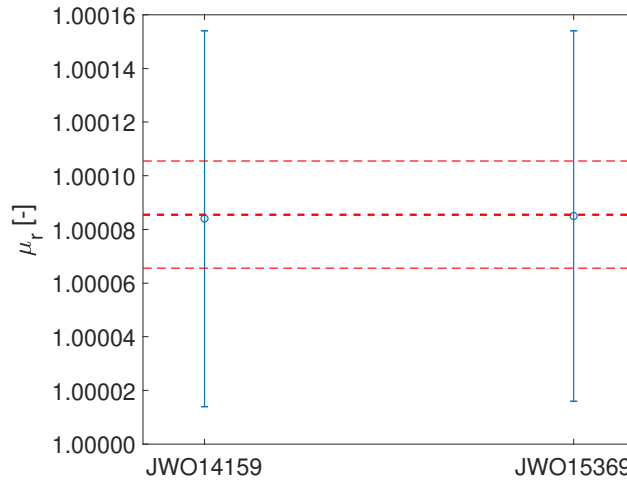
Fig. 8.12 Comparison of the measurement results for the two tungsten alloy specimens at a
test field of 1 T. In blue, the values and coverage intervals obtained by SSM as a result of the
Monte Carlo simulations. In red, the reference value measured by VSM (thick dashed line)
and the coverage interval (thin dashed line), corresponding to a 95 % of level of confidence.

the perturbed field does not change significantly with respect to the background
field, and therefore the modeling assumptions have a negligible impact on the
results. Another factor is that the uncertainty value resulting from the Monte Carlo
simulations has been overestimated, as mentioned in Sec. 8.1.2.

8.3   Characterization of two stainless steel bellows for the warm-cold transitions in the HL-LHC cryomodules

8.3.1   Context

The installation of RF crab cavities is one of the key upgrades in the framework
of the HL-LHC project [8, 209, 210, 211]. These elements, to be installed in
correspondence with the intersection points, will help increase the luminosity by
tilting the proton bunches in each of the two beams to maximize their overlap at the
collision point [212] and increase the probability of collision.

Two concepts were proposed: Double Quarter Wave (DQW) and RF Dipole
(RFD) cryomodules, designed and prototyped initially for cold tests in the Super
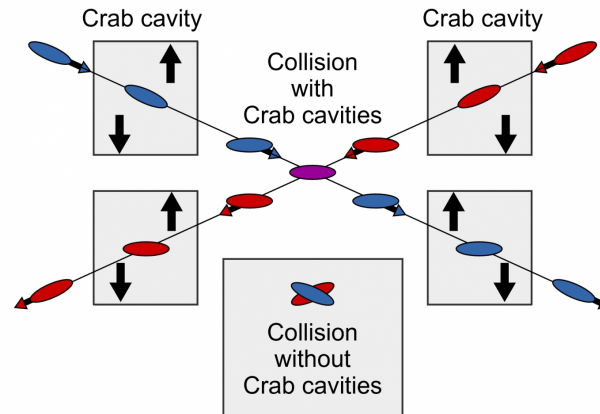
Fig. 8.13 Effect of the crab cavities on the proton bunches (© 2017-2022 CERN).

Proton Synchrotron (SPS) prior to the final application in the LHC. Fig. 8.14 shows the layout of the DQW cryomodule.
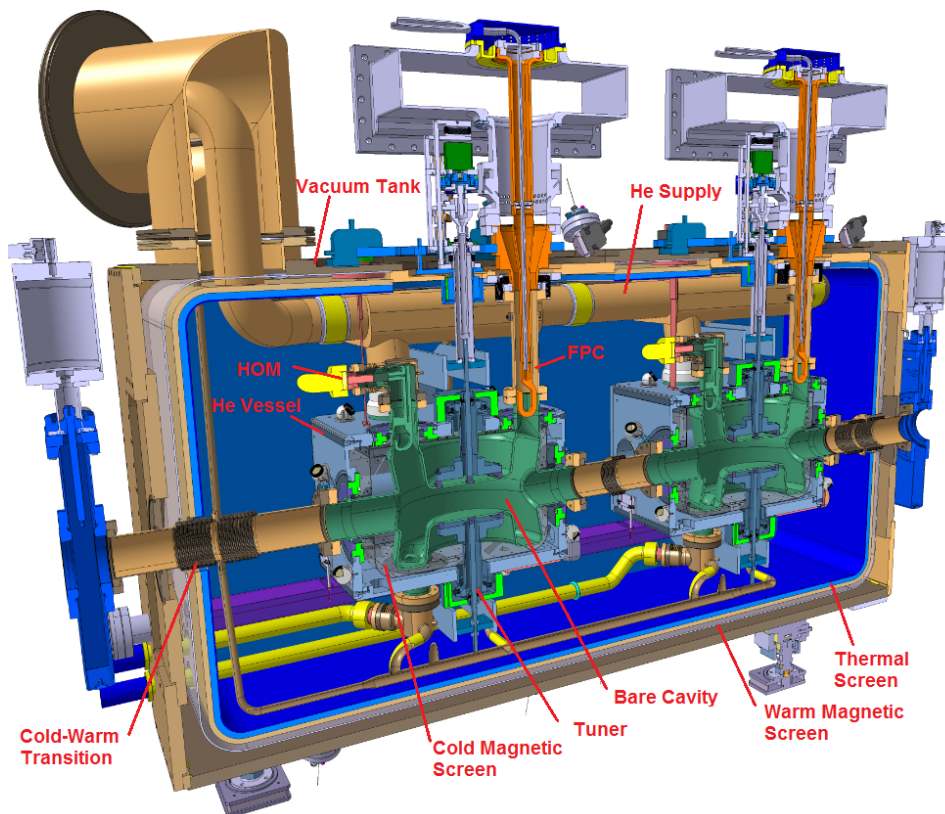
Fig. 8.14 DQW cryomodule layout [8].

Each cryomodule contains two cavities made of bulk niobium and operated at 1.9 K, called *bared cavities*. The assembly of the bare cavity with couplers and

auxiliary systems is called *dressed cavity* [8]. Each dressed cavity contains a cold magnetic shield made of a 1 mm thick layer of CRYOPHY [69] to shield DC stray fields down to the nT level. The entire cryomodule assembly will be shielded with a second warm, magnetic shield that will be realized in Mumetal® [213, 214].

The cold-warm transitions are bellows made of stainless steel AISI type 316L. The steel grade specified by the requirements is 1.4441, a high-quality grade that is less sensitive to martensite precipitation when cold worked and, therefore, is less likely that its magnetic permeability increases. However, the properties of another general-purpose steel grade, 1.4404, were investigated as an alternative to 1.4441. This solution would allow budget saving and solve availability problems.

This case study aims at presenting the magnetic characterization of two bellows, showcasing how the SSM can be used to measure finished parts. The two bellows were realized respectively in 1.4404 and 1.4441. Moreover, four test specimens, three made of 1.4404 and one made 1.4441, were realized to measure the magnetic properties of the two raw materials and compare them with the finished parts.

The two bellows are shown in Fig. 8.15, and they have approximately a radius of 115 mm and a height of 35 mm. A CAD drawing was imported into the FE model and used for the simulations. The number of convolutions is lower for the bellows made of 1.4404, but it has a flange made of AISI type 316LN, grade 1.4429, welded on it. The thickness in correspondence of the bellows' convolutions is 0.1 mm.

(a) Grade 1.4404   (b) Grade 1.4441
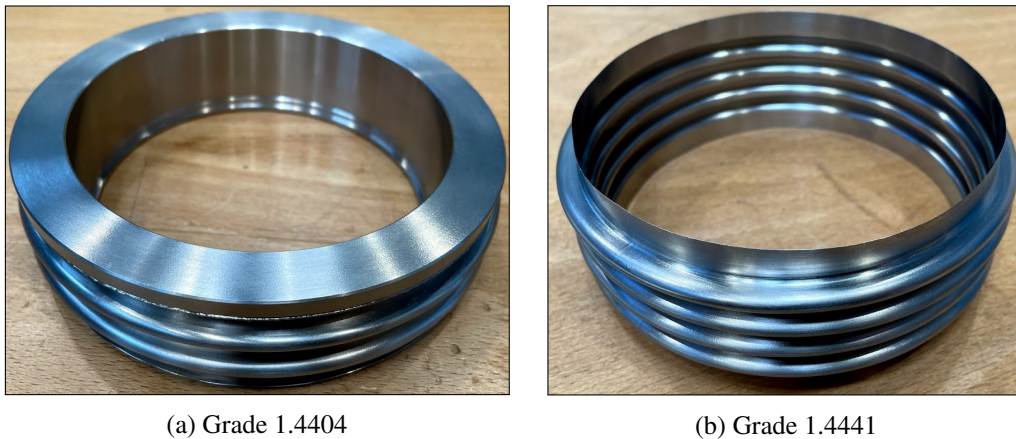
Fig. 8.15 Bellows for the HL-LHC cryomodules to be tested.

Fig. 8.16 shows the test specimens realized to test the raw materials. For the 1.4404, three stacks of 100 0.1-mm-thick laminations, each having size 41.8×200 mm^2, were measured. The 1.4441 test specimen is a stack of 63 0.2-mm-thick laminations,

having dimensions 40.7×100 mm^2. All the stacks were cut by guillotine and glued with epoxy resin.

(a) Grade 1.4404

(b) Grade 1.4441
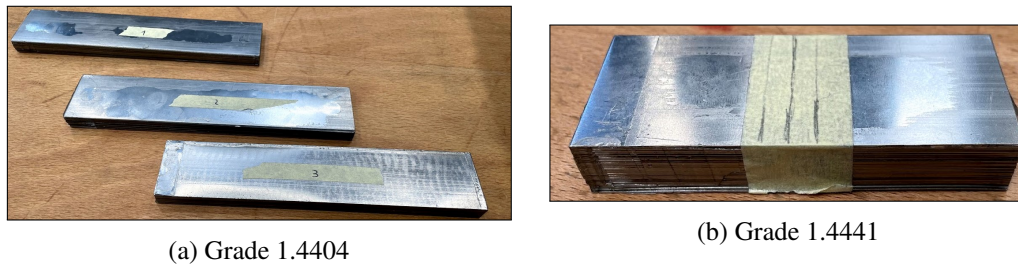
Fig. 8.16 Test specimens of the raw materials used for the bellows in Fig. 8.15.

8.3.2   Results and discussion

Fig. 8.17 shows the background and the perturbed field profiles for the raw material and the finished bellows, evaluated at a test field of 1 T. The background field profiles differ from case to case, because the measurements were performed in about six months, where the linear motor was re-installed in a different position, thus mapping a different portion of the map shown in Fig. 6.12.

The perturbed field profiles for the raw material measurements - cases (a) and (b) - are different due to a combination of different specimen sizes and background field profiles. The distribution of the residuals is not random but presents a trend deriving from a geometry approximation. The specimens were modeled as perfect parallelepipeds, but they are slightly bent due to technical difficulties that occurred during the gluing of the stacks caused by their very low thickness. Therefore, the specimen's shape was not perfectly regular. However, the root mean square error in both cases has a value of about 2 μT, which is still comparable with the measurement accuracy.

The perturbed field profiles for the bellows measurements - cases (c) and (d) - are also different. The bellows made of 1.4404 was measured in correspondence of the flange, where the thickness is an order of magnitude higher than in the convolutions. Therefore, the field perturbation is higher. The measurement performed in correspondence of the convolutions would have been as in case (d), where the extremely low thickness (0.1 mm) determines a perturbed field profile closely comparable with the background field. The distribution of the residual in case (c) is not random because

(a) Raw - s1, 1.4404, $\mu_r =$1.00269

(b) Raw, 1.4441, $\mu_r =$1.00254

(c) Bellows, 1.4404, $\mu_r =$1.00279

(d) Bellows, 1.4441, $\mu_r =$1.00255
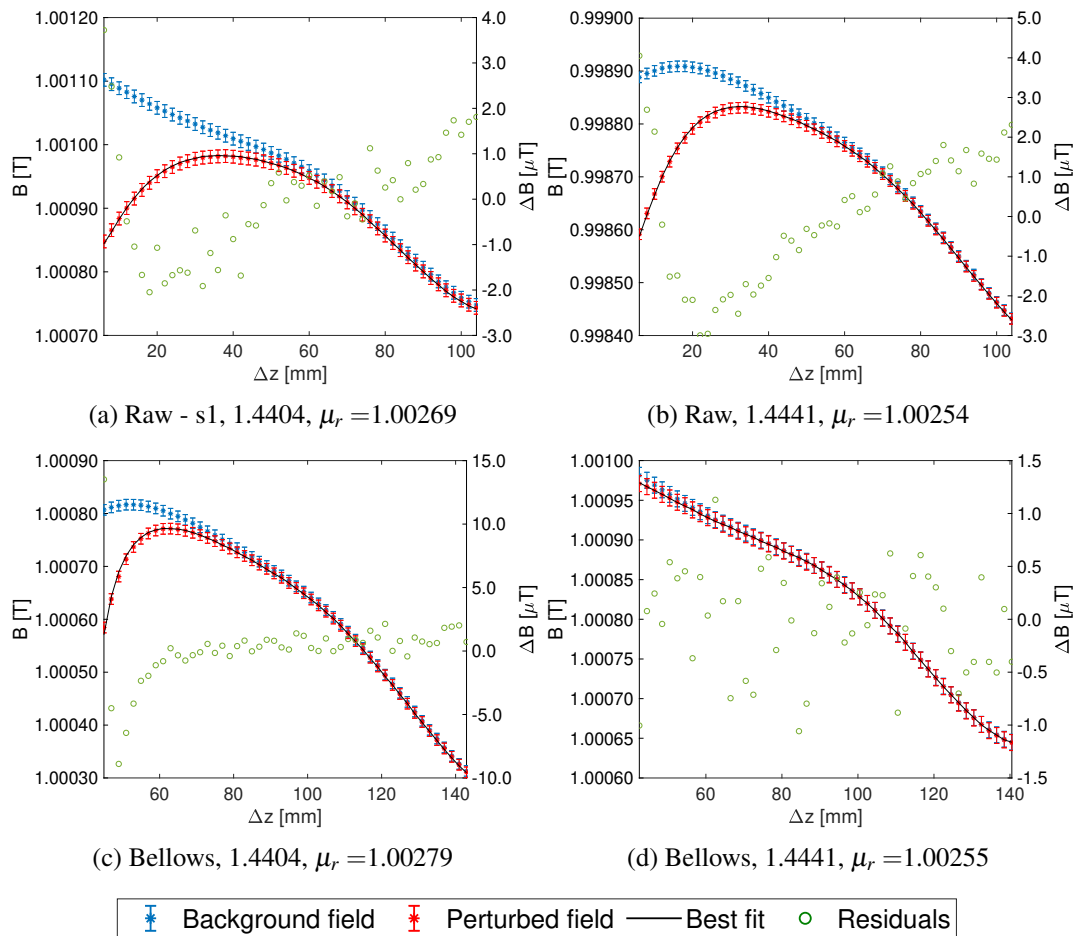
Fig. 8.17 Field profiles for the raw material measurement and the finished bellows at a test field of B_t=1 T as a function of the distance from the specimen Δz. In blue, the measured background field; in red, the perturbed field; in black, the simulated field; and in green, the residuals, displayed on the right vertical axes.

of inaccuracies deriving from the CAD drawing.

Fig. 8.18 shows the measurement results, consisting of the measured relative permeability values as a function of the applied magnetic field. The values were obtained by averaging five consecutive measurements.

The measured values are closely comparable in both cases. In particular, the three stacks of 1.4404 match among them at a 10^{-5} level. The measured permeability values in the 1.4441 case are slightly lower than the 1.4404, at a 10^{-4} level. The bellows have a permeability higher than their respective raw materials. This outcome arises from the martensite precipitation resulting from the machining of the finished part, corresponding to a 30 % of pulling deformation of the material sheet to form a

(a) 1.4404   (b) 1.4441
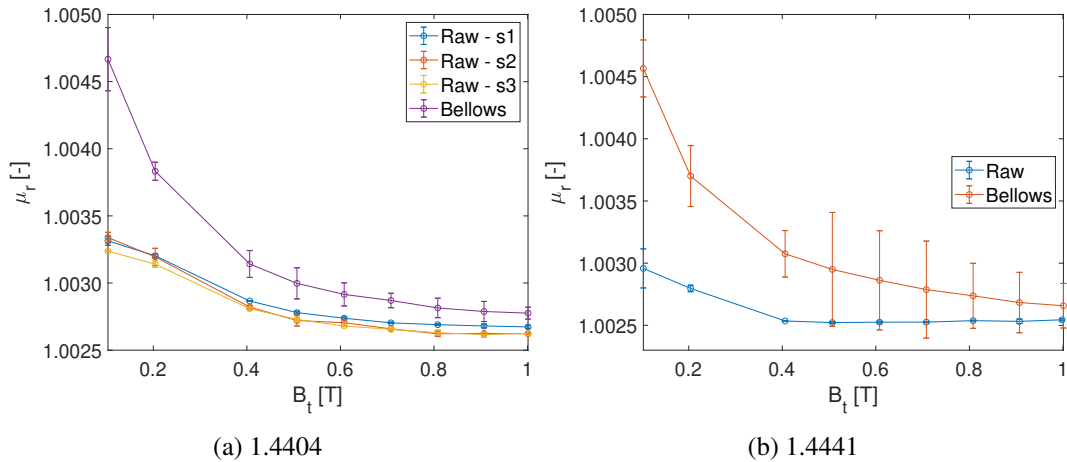
Fig. 8.18 Measured relative permeability values for the raw material and the finished bellows as a function of the applied test field, with their repeatability bars.

closed shape. The permeability values of the bellows made of 1.4441 have a lower permeability in comparison with the 1.4404; this behavior results from the much lower SNR of the measurement and the much lower material cross-section in the field direction.

8.4 Final comments and concept for a cryogenic version.

The static-sample magnetometry was validated by presenting three case studies to assess the performance of the method in different operating conditions. The method was proven to be comparable to the VSM, the most used state-of-the-art solution in metrology laboratories. The standard uncertainty corresponding to a 95 % level of confidence is in the order of 10^{-4}. This uncertainty, calculated from type B sources of uncertainty sources and therefore in a worst-case scenario, was slightly overestimated and is higher than the reported standard deviation values of the repeated measurements. This situation can be improved by better improving the determination of the probe positioning. The method was proved to be general and applicable to specimens having various size and shape, as long they fit in the magnet air gap, and a CAD drawing of the object to be tested is available. Given the higher repeatability values, the method is less accurate when measuring finished parts than

regular geometries because the geometrical uncertainties and the positioning have a higher impact.

On the other hand, the possibility of measuring finished parts is an advantage and paves the way for many applications. For instance, magnetic permeability plays a key role in Magnetic Resonance Imaging (MRI) compatibility [215] of instrumentation and prosthesis. On one hand, forces and torques have to be avoided for safety reasons. This condition is generally satisfied if $\chi_m < 10^{-2}$. However, as also seen in this dissertation, distortion of the field lines still persist. This distortion in MRI applications is equivalent in degraded image quality in the proximity of the imaging region, and can be avoided if $\chi_m - \chi_{mH_2O} < 10^{-5}$. In this context, the potential of the SSM to be used to test finished parts, whose magnetic permeability can differ from the raw material. An example is shown in Fig. 8.19, reporting the measurement results of a hip prosthesis made of F-75, a cobalt-titanium alloy. In the absence of a 3D drawing, the object was scanned in 3D and imported in the FE software.

The probe positioning constitutes the bottleneck of the method because it is the most significant uncertainty source. The positioning is the issue to be solved when applying the method at cryogenic temperatures. A concept is presented in Fig. 8.20. The concept consists of cooling only the test specimen while leaving the rest at room temperature.

The cooling will be realized employing a double-wall dewar, and therefore the probe cannot be in contact with the specimen's surface. This leads to a higher measurement uncertainty because the probe-specimen distance cannot be deduced anymore only from the datasheet of the probe. Moreover, materials having very low permeability, such as tungsten alloys, cannot be measured because the perturbation occurs in the first 10-20 mm from the specimen, not physically accessible. The thickness of the cryostat's walls, commonly in the order of 20 mm, can be reduced by adopting other materials (i.e. glass) in combination with optical measurements to monitor the probe-specimen distance. Other alternatives can include an NMR probe operated at cryogenic temperature, but realizing a system capable of moving at cold presents technical difficulties that need to be solved.

(a) A photograph of the prosthesis

(b) Background and perturbed field maps at a test field of 1 T.

(c) Finite Element simulation
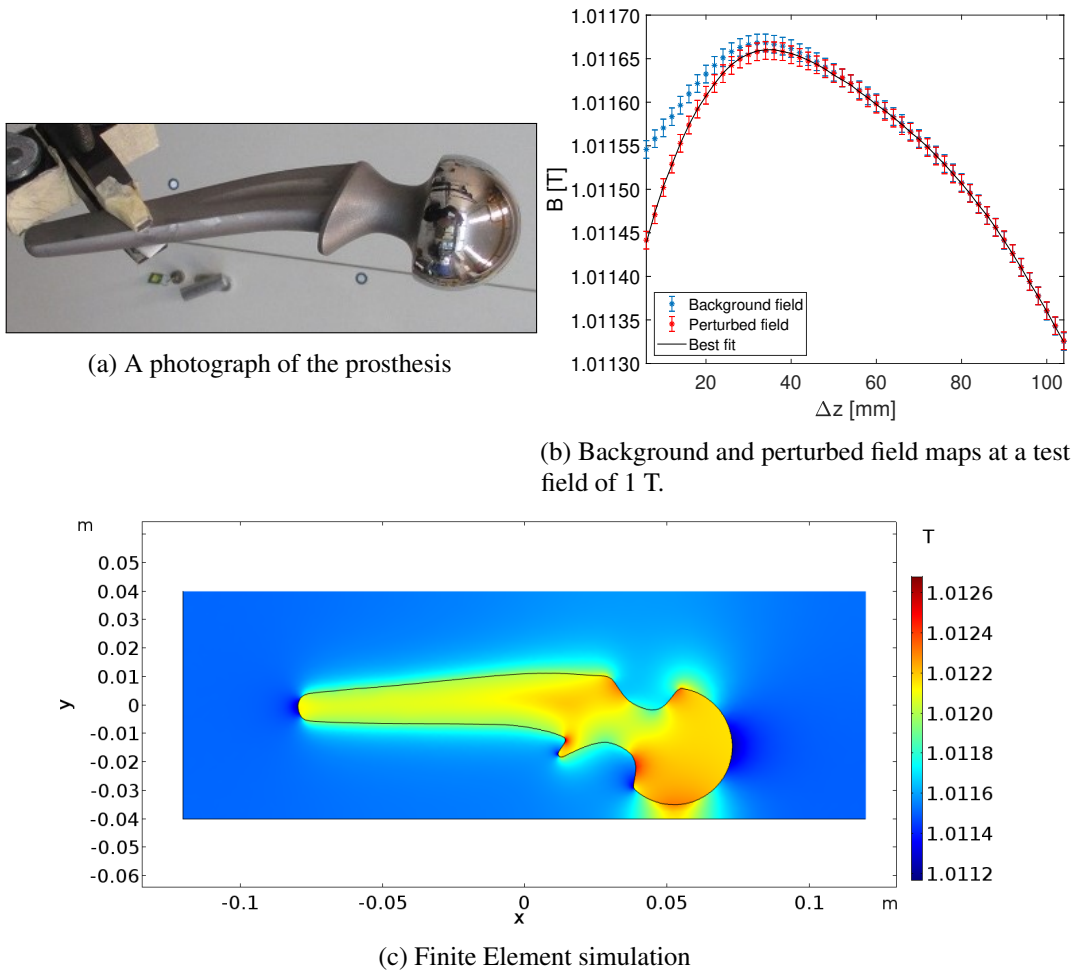
Fig. 8.19 Measurement results of a hip prosthesis made of F-75, at a test field of 1 T. Computed magnetic permeability $\mu_r = 1.00093 \pm 0.00003$.
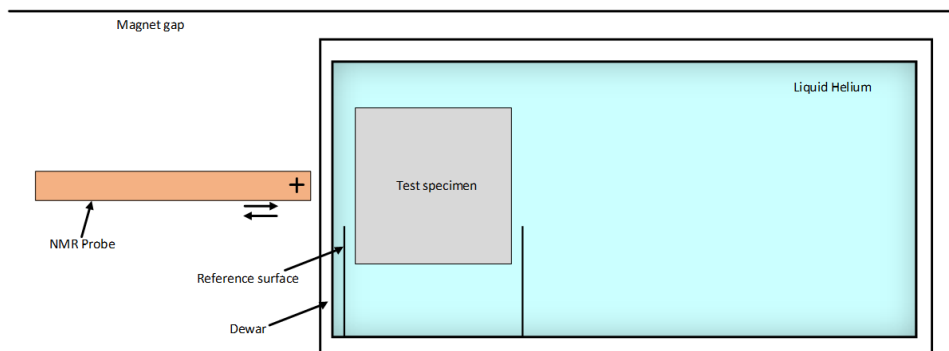
Fig. 8.20 Concept layout of a cryogenic SSM.

Conclusions

The work presented in this dissertation showed that the characterization of magnetic materials at extreme ranges of field, temperature, and permeability is relevant for particle accelerator applications. In particular, the characterization of soft ferromagnetic steels at very high fields and cryogenic temperatures is relevant for accelerators using superconducting magnet technology.

From an operative point of view, characterizing a material means accurately measuring how the material responds to an externally applied field. In some cases, the material responds with a magnetization much higher than the external field; this is the case of soft ferromagnetic alloys, where relative permeabilities higher than 1000 can be characterized by applying a few mT of excitation field or, equivalently, a field in the order of a few tens of kA/m. Such low field values simplify the layout of the measurement system, which can be used in a closed-circuit configuration utilizing a transformer-based system. When the permeability is comparable to the vacuum, excitation fields in the order of 1 T or higher, combined with a high-resolution detection system, are required; in such cases, external field sources and stray-field methods are required. In conclusion, the nominal material properties play a crucial role in choosing a suitable measurement system.

According to the principle mentioned above, the characterization of soft ferromagnetic steels at fields comparable with their magnetization saturation ideally would have required a stray-field method. In this dissertation, the problem was tackled by developing a superconducting permeameter, thus exploiting an already existing method, the ring method, and extending the operating range. The main feature is the adoption of NbTi superconducting coil technology, which was possible because the system is operated at 4.2 K and, therefore, without thermal and resistance concerns arising from the use of copper coils. Moreover, the use of the superconductor allowed to keep the resistance close to zero and re-use the existing hardware. The system

was verified to be self-protected against quench events, and therefore no additional protection elements in the excitation circuit were necessary. Moreover, the superconductor magnetization due to the persistent currents was proved to have a negligible impact on the measurement results. The system was used to characterize ARMCO® Pure Iron, to be used as the iron yoke for the upgrade of the LHC superconducting magnets. Given the lack of detail in the literature, guidelines were proposed for the magnetic characterization of soft ferromagnetic materials at cryogenic temperatures, including the only use of the point-by-point method given the higher eddy currents and a new calibration procedure. The system proved to not be optimized for low fields. The increased number of excitation turns determines two main problems on the H-field. A first problem is that the uncertainty values of the H-field increase up to one order of magnitude, because they scale with the number of excitation turns N_e. On the other hand, power supply inaccuracies at low currents have a greater impact on the degaussing procedure, which can leave a high residual of degaussing. This residual is corrected during the post-processing, but lower B-field values could not be measured because the iron magnetization remains confined on a minor asymmetric hysteresis loop, shifted on the B-axis. Data in the saturation region are accurate because the uncertainty of H is below 0.05 %. As explained in Sec. 5.3, this behavior was expected since the system is conceived to work at high-fields. Nevertheless, the range can be extended by winding an auxiliary excitation coil with fewer turns to perform measurements at low fields. The uncertainty of the B values, on the other hand, are comparable with room temperature measurements because the number of sensing turns is the same. Nevertheless, it is dependent on the specimen cross-section and increases as the cross-section area decreases.

The measured values were validated in both case studies by comparison with measurements performed on a similar test specimen and with values from the literature. Further increasing the excitation field is unnecessary for future applications of this work because data can be extrapolated once the material has fully saturated.

One technical issue remains open: the mechanical stress applied to the specimen when cooled down to cryogenic temperatures. This problem needs further investigation, and the starting point will be to investigate the impact of the cooling rate of the test specimen.

For low-permeability materials, a change of paradigm was necessary, and a new measurement system, the static-sample magnetometer, was developed. The system works on the flux-distortion detection principle and consists of a dipole magnet de-

livering up to a 1-T field in the gap combined with an NMR teslameter as a detection system. The measurement principle consists of a two-step measurement, where the background field and the field perturbed by the presence of the specimen are scanned. The post-processing is performed by FE analysis to compute the permeability. The system was proved to have uncertainty comparable with the VSM, the reference state-of-the-art solution. The uncertainty value can be further improved by accurately calibrating the NMR teslameter position, known only within 0.5 mm of accuracy from the datasheet. The system works with specimens having whichever shape and dimensions, at the condition that they fit within the magnet gap, and therefore it can also be used to characterize finished parts once provided a CAD drawing, which is an advantage and paves the way for many applications, as shown in Sec. 8.4. The next step is the development of a cryogenic version, having a cold specimen in a warm magnet bore, which is currently under study.

Bibliography

[1] Oliver Sim Brüning, P Collier, P Lebrun, S Myers, R Ostojic, J Poole, and P Proudlock. *LHC Design Report. CERN Yellow Reports: Monographs. Geneva: CERN, 2004. doi: 10.5170.* Tech. rep. CERN-2004-003-V-1.

[2] Lucio Rossi, O Brüning, et al. "High luminosity large hadron collider". In: *European Strategy Preparatory Group-Open Symposium, Krakow.* 2012.

[3] Lorenzo Bortot, Bernhard Auchmann, I Cortes Garcia, AM Fernandez Navarro, Michał Maciejewski, Matthias Mentink, Marco Prioli, Emmanuele Ravaioli, S Schps, and AP Verweij. "STEAM: A hierarchical cosimulation framework for superconducting accelerator magnet circuits". In: *IEEE Transactions on applied superconductivity* 28.3 (2017), pp. 1–6.

[4] Enrico Carraro, Michele Degano, Mattia Morandin, and Nicola Bianchi. "Formula SAE electric competition: Electrical motor design". In: *2013 International Electric Machines & Drives Conference.* IEEE. 2013, pp. 1142–1148.

[5] Thang Pham, Patrick Kwon, and Shanelle Foster. "Additive manufacturing and topology optimization of magnetic materials for electrical machines—A review". In: *Energies* 14.2 (2021), p. 283.

[6] Malika Meddahi, Julie Coupard, Heiko Damerau, Anne Funken, Simone Gilardoni, Brennan Goddard, Klaus Hanke, Lelyzaveta Kobzeva, Alessandra Lombardi, Django Manglunki, et al. "Status of the LHC Injectors Upgrade (LIU) Project at CERN". In: *6th Int. Particle Accelerator Conf.(IPAC'15), Richmond, VA, USA, May 3-8, 2015.* JACOW, Geneva, Switzerland. 2015, pp. 3915–3918.

[7] S Redaelli et al. "Collimation upgrades for HL-LHC". In: *CERN Yellow Reports* 2 (2015), pp. 225–225.

[8]   Federico Carra, A Amorim Carvalho, K Artoos, S Atieh, I Aviles Santillana, S Belomestnykh, A Boucherie, JP Brachet, K Brodzinski, G Burt, et al. "Crab cavity and cryomodule development for HL-LHC". In: *17th Int. Conf. on RF Superconductivity (SRF'15), Vancouver BC, Canada, September 13-18, 2015*. 2015, pp. 1460–1466.

[9]   N Catalan Lasheras, B Auchmann, G Kirby, K-H Mess, R Ostojic, and S Russenschuck. "Effects of collar permeability on the field quality of the large aperture quadrupoles for the LHC". In: *IEEE transactions on applied superconductivity* 18.2 (2008), pp. 104–107.

[10]   Simon Foner. "Vibrating sample magnetometer". In: *Review of Scientific Instruments* 27.7 (1956), pp. 548–548.

[11]   Fausto Fiorillo. "Measurements of magnetic materials". In: *Metrologia* 47.2 (2010), S114.

[12]   Stephen Blundell. *Magnetism in condensed matter*. American Association of Physics Teachers, 2003.

[13]   Carl L Nave. *Magnetic Properties of Solids*. HyperPhysics, 2008.

[14]   RE Glick. "On the diamagnetic susceptibility of gases". In: *The Journal of Physical Chemistry* 65.9 (1961), pp. 1552–1555.

[15]   Richard M Bozorth. "Magnetism". In: *Reviews of Modern Physics* 19.1 (1947), p. 29.

[16]   Stephan Russenschuck. *Field computation for accelerator magnets: analytical and numerical methods for electromagnetic design and optimization*. John Wiley & Sons, 2011.

[17]   Giorgio Bertotti. *Hysteresis in magnetism: for physicists, materials scientists, and engineers*. Gulf Professional Publishing, 1998.

[18]   Zdzislaw Wlodarski. "Analytical description of magnetization curves". In: *Physica B: Condensed Matter* 373.2 (2006), pp. 323–327.

[19]   David C Jiles and David L Atherton. "Theory of ferromagnetic hysteresis". In: *Journal of applied physics* 55.6 (1984), pp. 2115–2120.

[20]   DC Jiles, A Ramesh, Y Shi, and X Fang. "Application of the anisotropic extension of the theory of hysteresis to the magnetization curves of crystalline and textured magnetic materials". In: *IEEE Transactions on Magnetics* 33.5 (1997), pp. 3961–3963.

[21] Alessandro Salvini and Francesco Riganti Fulginei. "Genetic algorithms and neural networks generalizing the Jiles-Atherton model of static hysteresis for dynamic loops". In: *IEEE Transactions on Magnetics* 38.2 (2002), pp. 873–876.

[22] Krzysztof Chwastek. "Modelling of dynamic hysteresis loops using the Jiles–Atherton approach". In: *Mathematical and computer modelling of dynamical systems* 15.1 (2009), pp. 95–105.

[23] ID Mayergoyz. "Dynamic Preisach models of hysteresis". In: *IEEE Transactions on Magnetics* 24.6 (1988), pp. 2925–2927.

[24] R Ben Mrad and H Hu. "Dynamic modeling of hysteresis in piezoceramics". In: *2001 IEEE/ASME International Conference on Advanced Intelligent Mechatronics. Proceedings (Cat. No. 01TH8556)*. Vol. 1. IEEE. 2001, pp. 510–515.

[25] Maria Amodeo, Pasquale Arpaia, Marco Buzio, Vincenzo Di Capua, and Francesco Donnarumma. "Hysteresis Modeling in Iron-Dominated Magnets Based on a Multi-Layered NARX Neural Network Approach". In: *International journal of neural systems* 31.09 (2021), p. 2150033.

[26] AA Adly and SK Abd-El-Hafiz. "Using neural networks in the identification of Preisach-type hysteresis models". In: *IEEE Transactions on Magnetics* 34.3 (1998), pp. 629–635.

[27] Claudio Serpico and Ciro Visone. "Magnetic hysteresis modeling via feedforward neural networks". In: *IEEE Transactions on Magnetics* 34.3 (1998), pp. 623–628.

[28] John MD Coey. *Magnetism and magnetic materials*. Cambridge university press, 2010.

[29] CERN PS Division. *The CERN Proton Synchrotron magnet*. Technical Report EDMS 1262033. European Organization for Nuclear Research (CERN), 1972.

[30] K Steffen. "Basic course on accelerator optics". In: *CAS - CERN Accelerator School : General Accelerator Physics* (1985).

[31] Bernhard J Holzer. "Beam optics and lattice design for particle accelerators". In: *arXiv preprint arXiv:1303.6514* (2013).

[32] E Métral, T Argyropoulos, H Bartosik, N Biancacci, Xavier Buffat, JF Este-ban Muller, W Herr, G Iadarola, A Lasheen, K Li, et al. "Beam instabilities in hadron synchrotrons". In: *IEEE Transactions on Nuclear Science* 63.2 (2016), pp. 1001–1050.

[33] Carlo Petrone. "Wire methods for measuring field harmonics, gradients and magnetic axes in accelerator magnets". PhD thesis. Università degli Studi del Sannio, 2013.

[34] Stephan Russenschuck. "Rotating-and translating-coil magnetometers for extracting pseudo-multipoles in accelerator magnets". In: *COMPEL-The international journal for computation and mathematics in electrical and electronic engineering* (2017).

[35] Pasquale Arpaia, Marco Buzio, Lucio Fiscarelli, Giuseppe Montenero, and Louis Walckiers. "High-performance permeability measurements: A case study at CERN". In: *2010 IEEE Instrumentation & Measurement Technology Conference Proceedings*. IEEE. 2010, pp. 58–61.

[36] Oliver Köster, Lucio Fiscarelli, and Stephan Russenschuck. "A procedure for combining rotating-coil measurements of large-aperture accelerator mag-nets". In: *Nuclear Instruments and Methods in Physics Research Section A: Accelerators, Spectrometers, Detectors and Associated Equipment* 818 (2016), pp. 20–25.

[37] Luca Bottura and Bernardo Bordini. "$J_C(B,T,\varepsilon)$ Parametrization for the ITER Nb$_3$Sn Production". In: *IEEE transactions on applied superconductiv-ity* 19.3 (2009), pp. 1521–1524.

[38] Christine Völlinger. "Superconductor magnetization modeling for the numer-ical calculation of field errors in accelerator magnets". PhD thesis. Berlin, Tech. U., 2002.

[39] C Vollinger, Martin Aleksa, and Stephan Russenschuck. "Compensation of magnetization effects in superconducting accelerator magnets". In: *IEEE transactions on applied superconductivity* 12.1 (2002), pp. 1492–1495.

[40] PA Thonet. "Use of permanent magnets in multiple projects at CERN". In: *IEEE Transactions on Applied Superconductivity* 26.4 (2016), pp. 1–4.

[41]   Klaus Halbach. "Design of permanent multipole magnets with oriented rare earth cobalt material". In: *Nuclear instruments and methods* 169.1 (1980), pp. 1–10.

[42]   Lorenzo Resegotti. "The LEP magnet system". In: *Le Journal de Physique Colloques* 45.C1 (1984), pp. C1–233.

[43]   Daniel Schoerling. "Case study of a magnetic system for low-energy machines". In: *Physical Review Accelerators and Beams* 19.8 (2016), p. 082401.

[44]   Attilio Milanese, Jeremie Bauche, and Carlo Petrone. "Magnetic Measurements of the First Short Models of Twin Aperture Magnets for FCC-ee". In: *IEEE Transactions on Applied Superconductivity* 30.4 (2020), pp. 1–5.

[45]   D Einfeld. "Specifications, quality control, manufacturing, and testing of accelerator magnets". In: *arXiv preprint arXiv:1103.1815* (2011).

[46]   V Lopez-Dominguez, Adrián Quesada, JC Guzmán-Mìnguez, L Moreno, M Lere, J Spottorno, F Giacomone, JF Fernández, Antonio Hernando, and MA Garcìa. "A simple vibrating sample magnetometer for macroscopic samples". In: *Review of Scientific Instruments* 89.3 (2018), p. 034707.

[47]   Christopher P Riley. "Enhancements to the OPERA-3D suite". In: *AIP Conference Proceedings*. Vol. 391. 1. American Institute of Physics. 1997, pp. 101–106.

[48]   Stephano Sgobba and Cécile Boudot. "Soudabilité laser d'aciers inoxydables austénitiques pour l'écran de faisceau du grand collisionneur protonique". In: *Matériaux & Techniques* 85.11-12 (1997), pp. 23–27.

[49]   M Masuzawa, K Tsuchiya, and A Terashima. "Study of magnetic shielding materials and fabrication of magnetic shield for superconducting cavities". In: *IEEE transactions on applied superconductivity* 24.3 (2013), pp. 1–4.

[50]   Sergei Nagaitsev, Consolato Gattuso, Stanley Pruss, and James Volk. "Experience with magnetic shielding of a large scale accelerator". In: *PACS2001. Proceedings of the 2001 Particle Accelerator Conference (Cat. No. 01CH37268)*. Vol. 5. IEEE. 2001, pp. 3371–3373.

[51]   S Sgobba. "Physics and measurements of magnetic materials". In: *arXiv preprint arXiv:1103.1069* (2011).

[52] E Ferrara, E Olivetti, F Fiorillo, E Forton, L Martino, and L Rocchino. "Microstructure and magnetic properties of pure iron for cyclotron electromagnets". In: *Journal of alloys and compounds* 615 (2014), S291–S295.

[53] Fausto Fiorillo. *Characterization and measurement of magnetic materials*. Academic Press, 2004.

[54] P Tiberto, V Basso, C Beatrice, and G Bertotti. "Hysteresis properties of conventionally annealed and Joule-heated nanocrystalline Fe735Cu1Nb3Si135B9 alloys". In: *Journal of magnetism and magnetic materials* 160 (1996), pp. 271–272.

[55] V Basso, G Bertotti, F Fiorillo, and M Pasquale. "Dynamic Preisach model interpretation of power losses in rapidly quenched 6.5% SiFe". In: *IEEE Transactions on Magnetics* 30.6 (1994), pp. 4893–4895.

[56] H Shokrollahi and K Janghorban. "Different annealing treatments for improvement of magnetic and electrical properties of soft magnetic composites". In: *Journal of magnetism and magnetic materials* 317.1-2 (2007), pp. 61–67.

[57] Michaela Küpferling, Carlo Appino, Vittorio Basso, G Bertotti, F Fiorillo, and P Meilland. "Magnetic hysteresis in plastically deformed low-carbon steel laminations". In: *Journal of Magnetism and Magnetic Materials* 316.2 (2007), e854–e857.

[58] EW Collins. "Influence of process parameters on the magnetic proprties of LTV-processed steel". In: *Report to the Fermi National Accelerator Laboratory* (1995).

[59] F Bertinelli, S Comel, P Harlet, G Peiro, A Russo, and A Taquet. "Production of low-carbon magnetic steel for the LHC superconducting dipole and quadrupole magnets". In: *IEEE transactions on applied superconductivity* 16.2 (2006), pp. 1777–1781.

[60] O Kester, T Sieber, S Emhofer, F Ames, K Reisinger, P Reiter, PG Thirolf, R Lutter, D Habs, BH Wolf, et al. "Accelerated radioactive beams from REX-ISOLDE". In: *Nuclear Instruments and Methods in Physics Research Section B: Beam Interactions with Materials and Atoms* 204 (2003), pp. 20–30.

[61]   Christian G Schroer, Ilya Agapov, Werner Brefeld, Reinhard Brinkmann, Y-C Chae, H-C Chao, Mikael Eriksson, Joachim Keil, Xavier Nuel Gavaldà, Ralf Röhlsberger, et al. "PETRA IV: the ultralow-emittance source project at DESY". In: *Journal of synchrotron radiation* 25.5 (2018), pp. 1277–1290.

[62]   A Newborough, M Buzio, and R Chritin. "Upgrade of the CERN proton synchrotron booster bending magnets for 2 GeV operation". In: *IEEE transactions on applied superconductivity* 24.3 (2013), pp. 1–4.

[63]   Wim Weterings, Chiara Bracco, Louise Olivia Jorat, Malika Meddahi, Remy Noulibos, Pieter Van Trappen, et al. "The New Injection Region of the CERN PS Booster". In: *10th Int. Particle Accelerator Conf.(IPAC'19), Melbourne, Australia, May 19-24, 2019*. JACOW Publishing, Geneva, Switzerland. 2019, pp. 2414–2417.

[64]   Valentin Pricop. "Hysteresis effects in the cores of particle accelerator magnets". PhD thesis. Transilvania U., Brasov, 2016.

[65]   Daniel Schoerling. *Design Study: ELENA bending magnet prototype*. Tech. rep. 2013.

[66]   Attilio Milanese, M Shehab, and E Huttel. "Design of the main magnets of the SESAME Storage Ring". In: *5th Int. Particle Accelerator Conf.(IPAC'14), Richmond, VA, USA, May 3-8, 2015*. JACOW, Geneva, Switzerland. 2014, pp. 1292–1294.

[67]   Celozzi, Salvatore and Araneo, Rodolfo. "Electromagnetic shielding". In: *Encyclopedia of RF and Microwave Engineering* (2005).

[68]   Chetan Gohil, Neven Blaskovic Kraljevic, D Schulte, and P Burrows. "Mitigation of stray magnetic field effects in CLIC with passive shielding". In: (2018).

[69]   P Arpaia, M Buzio, O Capatina, K Eiler, SAE Langeslag, A Parrella, and NJ Templeton. "Effects of temperature and mechanical strain on Ni-Fe alloy CRYOPHY for magnetic shields". In: *Journal of Magnetism and Magnetic Materials* 475 (2019), pp. 514–523.

[70]   Stefano Sgobba and G Hochoertler. "A new non-magnetic stainless steel for very low temperature applications". In: (1999).

[71]   Stefano Sgobba. "Materials for high vacuum technology, an overview". In: (2006).

[72]   Metals Handbook. "Metallography, Structures and Phase Diagrams, Vol. 8". In: *ASM International, Materials Park, OH* (1973).

[73]   Woong Sup Park, Seong Won Yoo, Myung Hyun Kim, and Jae Myung Lee. "Strain-rate effects on the mechanical behavior of the AISI 300 series of austenitic stainless steel under cryogenic environments". In: *Materials & Design* 31.8 (2010), pp. 3630–3640.

[74]   K Couturier and Stefano Sgobba. "Phase stability of high manganese austenitic steels for cryogenic applications". In: *Materials Week, Munich, Germany, 25 - 28 Sep 2000*. 2000.

[75]   Helene Felice, Michel Segreti, Damien Simon, Jean Michel Rifflet, Jean Marc Gheller, Denis Bouziat, Arnaud Madur, Patrick Graffin, Henri Salvador, Jean François Millot, et al. "Development of MQYY: A 90-mm NbTi double aperture quadrupole magnet for HL-LHC". In: *IEEE Transactions on Applied Superconductivity* 28.3 (2018), pp. 1–5.

[76]   Pragasan Pillay and Ramu Krishnan. "Modeling of permanent magnet motor drives". In: *IEEE Transactions on industrial electronics* 35.4 (1988), pp. 537–541.

[77]   Davide Tommasini, Marco Buzio, Pierre-Alexandre Thonet, and Alexey Vorozhtsov. "Design, manufacture and measurements of permanent quadrupole magnets for Linac4". In: *IEEE transactions on applied superconductivity* 22.3 (2011), pp. 4000704–4000704.

[78]   Frank Gunsing, O Aberle, and Józef Andrzejewski. "Nuclear data measurements at the upgraded neutron time-of-flight facility n-TOF at CERN". In: *Proceedings of the 14th International Conference on Nuclear Reaction Mechanisms: Varenna, Italy: June 15-19, 2015*. 2015, pp. 323–330.

[79]   Akitaka Ariga, Tomoko Ariga, Jamie Boyd, Franck Cadoux, David W Casper, Francesco Cerutti, Salvatore Danzeca, Liam Dougherty, Yannick Favre, Jonathan L Feng, et al. "Technical proposal for FASER: forward search experiment at the LHC". In: *arXiv preprint arXiv:1812.09139* (2018).

[80]   JA Osborn. "Demagnetizing factors of the general ellipsoid". In: *Physical review* 67.11-12 (1945), p. 351.

[81]   Richard I Joseph. "Ballistic demagnetizing factor in uniformly magnetized cylinders". In: *Journal of applied physics* 37.13 (1966), pp. 4639–4643.

[82] Amikam Aharoni. "Demagnetizing factors for rectangular ferromagnetic prisms". In: *Journal of applied physics* 83.6 (1998), pp. 3432–3434.

[83] David Richter. *Measuring ferromagnetic with Vibrating Sample Magnetometer*. Oct. 2013. URL: https://indico.cern.ch/event/275911/contributions/621001/attachments/500281/691044/DR_2013_10_03.pdf.

[84] J Kerr and Edinburgh London. "Dublin philos. mag". In: *J. Sci* 5.30 (1878), pp. 161–177.

[85] DA Allwood, Gang Xiong, MD Cooke, and RP Cowburn. "Magneto-optical Kerr effect analysis of magnetic nanostructures". In: *Journal of Physics D: Applied Physics* 36.18 (2003), p. 2175.

[86] JM Florczak and E Dan Dahlberg. "Detecting two magnetization components by the magneto-optical Kerr effect". In: *Journal of applied physics* 67.12 (1990), pp. 7520–7525.

[87] Erik Klokholm. "The measurement of magnetostriction in ferromagnetic thin films". In: *IEEE Transactions on Magnetics* 12.6 (1976), pp. 819–821.

[88] A Moses. "Measurement of magnetostriction and vibration with regard to transformer noise". In: *IEEE Transactions on Magnetics* 10.2 (1974), pp. 154–156.

[89] DW Carnegie and J Timpf. "Characterizing permanent magnet blocks with Helmholtz coils". In: *Nuclear Instruments and Methods in Physics Research Section A: Accelerators, Spectrometers, Detectors and Associated Equipment* 319.1-3 (1992), pp. 97–99.

[90] Joseph J Stupak Jr. "A Method of Calibrating Helmholtz Coils for the Measurement of Permanent Magnets". In: *24th Annual Symposium, IMCSD*. 1995.

[91] Dunkel Olaf, Vittorio Remondino, and David Giloteaux. *Design, Calibration and Qualification of the CERN Helmholtz coils system*. Technical Report EDMS 1762799. European Organization for Nuclear Research (CERN), 2017.

[92] *Magnetic materials - Part 2: Methods of measurement of magnetic properties of electrical steel strip and sheet by means of an Epstein frame*. Standard IEC 60404–2. Geneva, CH: International Electrotechnical Commission, Mar. 1996.

[93]   *Magnetic materials - Part 3: Methods of measurement of the magnetic properties of magnetic sheet and strip by means of a single sheet tester.* Standard IEC 60404–3. Geneva, CH: International Electrotechnical Commission, Mar. 1992.

[94]   *Magnetic materials - Part 4: Methods of measurement of dc magnetic properties of magnetically soft materials.* Standard IEC 60404–4. Geneva, CH: International Electrotechnical Commission, Feb. 2000.

[95]   KV Namjoshi, J Douglas Lavers, and PP Biringer. "Eddy-current power loss in toroidal cores with rectangular cross section". In: *IEEE transactions on magnetics* 34.3 (1998), pp. 636–641.

[96]   Miroslav Markovic and Yves Perriard. "Eddy current power losses in a toroidal laminated core with rectangular cross section". In: *2009 International Conference on Electrical Machines and Systems*. IEEE. 2009, pp. 1–4.

[97]   Norio Takahashi, Masayuki Morishita, Daisuke Miyagi, and Masanori Nakano. "Examination of magnetic properties of magnetic materials at high temperature using a ring specimen". In: *IEEE Transactions on Magnetics* 46.2 (2010), pp. 548–551.

[98]   KN Henrichsen. "PERMEAMETER." In: *pp 735-9 of Proceedings of the Second International Conference on Magnet Technology, Oxford, England, 1967. Hadley, H.(ed.). Chilton, Eng., Rutherford Laboratory, 1967*. CERN, Geneva. 1968.

[99]   Alessandro Parrella. "Magnetic material characterization and magnet axis displacement measurement for particle accelerators". PhD thesis. University of Naples Federico II and University of Lisbon IST, 2018.

[100] R Kaczmarek, M Amar, and F Protat. "Iron loss under PWM voltage supply on Epstein frame and in induction motor core". In: *IEEE Transactions on Magnetics* 32.1 (1996), pp. 189–194.

[101] Yanxing Xing, Shaoxiong Zhou, Wenzhi Chen, Bangshao Dong, Yaqiang Dong, and Jian Wang. "Epstein frame investigation on soft magnetic properties of Fe-based amorphous strips". In: *Insight-Non-Destructive Testing and Condition Monitoring* 63.10 (2021), pp. 604–609.

[102]   John W Wilson, Lei Zhou, Claire L Davis, and Anthony J Peyton. "High temperature magnetic characterisation of structural steels using Epstein frame". In: *Measurement Science and Technology* 32.12 (2021), p. 125601.

[103]   Wei Wang, Arne Nysveen, and Niklas Magnusson. "Apparatus for loss measurements under multidirectional and dc-bias flux in electrical steel laminations". In: *Review of Scientific Instruments* 91.8 (2020), p. 084705.

[104]   Philip Marketos, Stan Zurek, and Anthony J Moses. "A method for defining the mean path length of the Epstein frame". In: *IEEE Transactions on magnetics* 43.6 (2007), pp. 2755–2757.

[105]   J Sievert, H Yang, P Zhang, and H Ge. "Studies on the systematic error of Epstein measurements". In: *International Journal of Applied Electromagnetics and Mechanics* 44.3-4 (2014), pp. 253–258.

[106]   Helmut Pfützner, Georgi Shilyashki, and Emanuel Huber. "Physical Assessment of the Magnetic Path Length of Energy Loss Testers". In: *IEEE Transactions on Magnetics* 56.12 (2020), pp. 1–7.

[107]   Markus Hofmann, Deniz Kahraman, Hans-Georg Herzog, and Michael J Hoffmann. "Numerical determination of the effective magnetic path length of a single-sheet tester". In: *IEEE transactions on magnetics* 50.2 (2014), pp. 929–932.

[108]   JP Gourber, J Billan, H Laeger, A Perrot, and L Resegotti. "LEP Division CERN". In: *IEEE Transactions on Nuclear Science* 30.4 (1983).

[109]   JP Gourber, J Billan, H Laeger, A Perrot, and Lorenzo Resegotti. "On the way to the series production of steel-concrete cores for the LEP dipole magnets". In: *IEEE Transactions on Nuclear Science* 30.4 (1983), pp. 3614–3616.

[110]   H Laeger, F Beco, S Comel, J Hostettler, R Luthi, and L Vuffray. "Production of the soft magnetic steel laminations for the LEP dipole magnets". In: *IEEE Transactions on Magnetics* 24.2 (1988), pp. 835–838.

[111]   M Buchner, K Höfler, B Henne, V Ney, and A Ney. "Tutorial: Basic principles, limits of detection, and pitfalls of highly sensitive SQUID magnetometry for nanomagnetism and spintronics". In: *Journal of Applied Physics* 124.16 (2018), p. 161101.

[112] Daniel Hurt, Shi Li, and Andreas Amann. "Versatile SQUID susceptometer with multiple measurement modes". In: *IEEE Transactions on Magnetics* 49.7 (2013), pp. 3541–3544.

[113] Robert L Fagaly. "Superconducting quantum interference device instruments and applications". In: *Review of scientific instruments* 77.10 (2006), p. 101101.

[114] Robert L Fagaly. "The Commercialization of SQUIDs". In: *IEEE Transactions on Applied Superconductivity* 25.3 (2014), pp. 1–7.

[115] Quantum Design. *Quantum Design MPMS3 Product Description*. Dec. 2021. URL: https://www.qdusa.com/siteDocs/productBrochures/1500-102.pdf.

[116] B Bordini, D Richter, P Alknes, A Ballarino, L Bottura, and L Oberli. "Magnetization Measurements of High-Jrm Nb3Sn Strands". In: *IEEE transactions on applied superconductivity* 23.3 (2013), pp. 7100806–7100806.

[117] B Bordini, Luca Bottura, Giorgio Mondonico, L Oberli, D Richter, Bernd Seeber, Carmine Senatore, E Takala, and D Valentinis. "Extensive Characterization of the 1 mm PIT Nb3Sn Strand for the 13-T FRESCA2 Magnet". In: *IEEE transactions on applied superconductivity* 22.3 (2011), pp. 6000304–6000304.

[118] Amalia Ballarino, Simon C Hopkins, Bernardo Bordini, David Richter, Davide Tommasini, Luca Bottura, Michael Benedikt, Michinaka Sugano, Toru Ogitsu, Shinya Kawashima, et al. "The CERN FCC conductor development program: a worldwide effort for the future generation of high-field magnets". In: *IEEE Transactions on Applied Superconductivity* 29.5 (2019), pp. 1–9.

[119] Tanjina Nasreen Ahmed, Maria Camila Belduque, DC Binod, Jitendra S Tate, and Wilhelmus J Geerts. "Time dependence of magnetic moment of strontium-ferrite powder measured with a biaxial vibrating sample magnetometer (VSM)". In: *AIP Advances* 11.1 (2021), p. 015048.

[120] Hind W Abdullah, Zena M Ali, Nada S Ahmade, and Zainab S Mahdi. "Preparation iron oxide nano powder in 20 minute". In: *AIP Conference Proceedings*. Vol. 2213. 1. AIP Publishing LLC. 2020, p. 020140.

[121] Taro Komori, Akihito Anzai, Toshiki Gushi, Kaoru Toko, and Takashi Sue-masu. "Molecular beam epitaxy growth of Mn4- xNixN thin films on MgO (0 0 1) substrates and their magnetic properties". In: *Journal of Crystal Growth* 507 (2019), pp. 163–167.

[122] D Jordán, D González-Chávez, D Laura, LM León Hilario, E Monteblanco, A Gutarra, and L Avilés-Félix. "Detection of magnetic moment in thin films with a home-made vibrating sample magnetometer". In: *Journal of Magnetism and Magnetic Materials* 456 (2018), pp. 56–61.

[123] Umar Saeed Khan, Abdur Rahim, Nasrullah Khan, Nawshad Muhammad, Fozia Rehman, Khalid Ahmad, and Jibran Iqbal. "Aging study of the pow-dered magnetite nanoparticles". In: *Materials Chemistry and Physics* 189 (2017), pp. 86–89.

[124] *A342/A342M-14 - Standard Test Methods for Permeability of Weakly Mag-netic Materials*. Standard A342/A342M-14. American Society for Testing and Materials, 2012.

[125] *Magnetic materials - Part 15: Methods for the determination of the relative magnetic permeability of feebly magnetic materials*. Standard IEC 60404–15. Geneva, CH: International Electrotechnical Commission, Mar. 2012.

[126] Institut Dr. Foerster GmbH & Co. *Foerster Magnetoscop 1.070 datasheet*. 2019. URL: http://www.foerstergroup.com/en/usa/products/magnetoscop-1070/.

[127] A Saunderson. "A permanent magnet Gouy balance". In: *Physics Education* 3.5 (1968), p. 272.

[128] Bernard L Morris and Aaron Wold. "Faraday balance for measuring magnetic susceptibility". In: *Review of Scientific Instruments* 39.12 (1968), pp. 1937–1941.

[129] Leonard F Lindoy, Vladimir Katovic, and Daryle H Busch. "A variable-temperature Faraday magnetic balance". In: *Journal of Chemical Education* 49.2 (1972), p. 117.

[130] DF Evans. "A new type of magnetic balance". In: *Journal of Physics E: Scientific Instruments* 7.4 (1974), p. 247.

[131] Lewis J Brubacher and Fred E Stafford. "Magnetic susceptibility: A physical chemistry laboratory experiment". In: *Journal of Chemical Education* 39.11 (1962), p. 574.

[132] Puligandla Viswanadham. "Inexpensive gouy balance for magnetic susceptibility determination". In: *Journal of Chemical Education* 55.1 (1978), p. 54.

[133] Daniel Laumann and Stefan Heusler. "Determining magnetic susceptibilities of everyday materials using an electronic balance". In: *American Journal of Physics* 85.5 (2017), pp. 327–332.

[134] MI Darby. "Tables of the Brillouin function and of the related function for the spontaneous magnetization". In: *British Journal of Applied Physics* 18.10 (1967), p. 1415.

[135] BE Argyle, SH Charap, and EW Pugh. "Deviations from T 3 2 Law for Magnetization of Ferrometals: Ni, Fe, and Fe+ 3% Si". In: *Physical Review* 132.5 (1963), p. 2051.

[136] JJ Gniewek and E Ploge. "Cryogenic behavior of selected magnetic materials". In: *Journal of research of the NBS-Engineering and Instrumentation* 69.3 (1965), pp. 225–236.

[137] Ming Yang, Yongjian Li, Qingxin Yang, Zhiwei Lin, Shuaichao Yue, Haoming Wang, and Chengcheng Liu. "Magnetic properties measurement and analysis of high frequency core materials considering temperature effect". In: *IEEE Transactions on Applied Superconductivity* 30.4 (2020), pp. 1–5.

[138] Masayoshi Nakaoka, Atsushi Fukuma, Hiroyuki Nakaya, Daisuke Miyagi, Masanori Nakano, and Norio Takahashi. "Examination of temperature characteristics of magnetic properties using a single sheet tester". In: *IEEJ Transactions on Fundamentals and Materials* 125.1 (2005), pp. 63–68.

[139] M Mikhov. "Sample holder for high-temperature vibrating sample magnetometer". In: *Review of Scientific Instruments* 72.9 (2001), pp. 3721–3722.

[140] Paul Oxley, Jennifer Goodell, and Robert Molt. "Magnetic properties of stainless steels at room and cryogenic temperatures". In: *Journal of Magnetism and Magnetic Materials* 321.14 (2009), pp. 2107–2114.

[141] RJ Commander and CBP Finn. "The magnetic susceptibilities of weakly magnetic materials used in cryogenic apparatus". In: *Journal of Physics E: Scientific Instruments* 3.1 (1970), p. 78.

[142] Xiaoze Pei, Alexander C Smith, Lode Vandenbossche, and Jan Rens. "Magnetic characterization of soft magnetic cores at cryogenic temperatures". In: *IEEE Transactions on Applied Superconductivity* 29.5 (2019), pp. 1–6.

[143] Eric Cabot Hannah. "Low temperature magnetic cores and a preamp for low impedance cryogenic sources". In: *Review of Scientific Instruments* 52.7 (1981), pp. 1087–1091.

[144] Shiyuan Yin, Mahmoud Mehrabankhomartash, Alfonso J Cruz, Lukas Graber, Maryam Saeedifard, Simon Evans, Florian Kapaun, Ivan Revel, Gerhard Steiner, Ludovic Ybanez, et al. "Characterization of Inductor Magnetic Cores for Cryogenic Applications". In: *2021 IEEE Energy Conversion Congress and Exposition (ECCE)*. IEEE. 2021, pp. 5327–5333.

[145] P. Harlet, F. Beco, and L. Renard. "Procédé de production d'acier doux". European Patent EP 0681031A1. Nov. 8, 1995.

[146] Simon Babic, Santo Comel, Francis Beckers, Francis Brixhe, Giuseppe Peiro, and Theodore Verbeeck. "Toward the production of 50 000 tonnes of low-carbon steel sheet for the LHC superconducting dipole and quadrupole magnets". In: *IEEE transactions on applied superconductivity* 12.1 (2002), pp. 1219–1222.

[147] Rosario Principe. *Technical Specification for the Supply of Low Carbon Steel Sheets for the Superconducting Magnets of the HL-LHC*. Engineering Specification EDMS 1498836. European Organization for Nuclear Research (CERN), 2015.

[148] AK Steel Co. *ARMCO product description*. 2016. URL: https://www.aksteel. eu/products/armco-pure-iron/#chemical-composition.

[149] S Kawabata. "Magnetic permeability of the iron yoke in high field superconducting magnets". In: *Nuclear Instruments and Methods in Physics Research Section A: Accelerators, Spectrometers, Detectors and Associated Equipment* 329.1-2 (1993), pp. 1–8.

[150] Andrea Apollonio, R Schmidt, A Verweij, M Solfaroli, and M Koratzinos. *Measurement of the Residual Resistivity Ratio of the busbars copper stabilizer of the 13kA circuits of the LHC*. Tech. rep. 2012.

[151] P. Fessia. *The new rapid prototyping machine at the CERN polymer lab: capabilities and limits*. Sep. 2013. URL: https://indico.cern.ch/event/271447/attachments/487943/674535/3D2.pdf.

[152] Furukawa Co. Ltd. *Specifications for NbTi round wire - F830/2.0 series*. Nov. 2014.

[153] Luca Bottura. "A practical fit for the critical surface of NbTi". In: *IEEE transactions on applied superconductivity* 10.1 (2000), pp. 1054–1057.

[154] Lucio Rossi and Massimo Sorbi. "QLASA: A computer code for quench simulation in adiabatic multicoil superconducting windings". In: *Nat. Inst. of Nucl. Phys.(INFN), Rome, Italy, Tech. Rep. TC-04-13* (2004).

[155] G Manfreda, L Rossi, and M Sorbi. "MATPRO upgraded version 2012: a computer library of material property at cryogenic temperature". In: *Tech. Rep. INFN-12-04/MI* (2012).

[156] AI Schindler and BC La Roy. "Residual Resistance Ratio of Pure Iron". In: *Journal of Applied Physics* 37.9 (1966), pp. 3610–3612.

[157] NI. *NI 4461/4462 specifications*. URL: https://www.ni.com/pdf/manuals/373770k.pdf.

[158] NI. *NI M-series 6281 specifications*. URL: https://www.ni.com/pdf/manuals/375218c.pdf.

[159] STMicroelectronics. *STTH200W06TV1 Turbo 2 ultrafast high voltage rectifier*. URL: https://eu.mouser.com/datasheet/2/389/stth200w06tv1-974384.pdf.

[160] Pasquale Arpaia, Marco Buzio, Lucio Fiscarelli, and Vitaliano Inglese. "A software framework for developing measurement applications under variable requirements". In: *Review of Scientific Instruments* 83.11 (2012), p. 115103.

[161] BIPM, IEC and IFCC, ILAC and ISO, IUPAC, IUPAP, and OIML. *Evaluation of Measurement Data, Guide to the Expression of Uncertainty in Measurement*. Tech. rep. Joint Committee for Guides in Metrology, 2008.

[162] Donglai Zhang, Xiaolan Yan, Enchao Zhang, and Shimin Pan. "A long time low drift integrator with temperature control". In: *Review of Scientific Instruments* 87.10 (2016), p. 105119.

[163] P Arpaia, P Cimmino, L De Vito, and L Fiscarelli. "Offset correction in a digital integrator for rotating coil measurements". In: *IMEKO World Congress" Metrology for green growth"*. 2012.

[164] Yanli Yang, Yanfei Zhao, and Dali Kang. "Integration on acceleration signals by adjusting with envelopes". In: *Journal of Measurements in Engineering* 4.2 (2016), pp. 117–121.

[165] JA Garcia and M Rivas. "A quasi-static magnetic hysteresis loop measurement system with drift correction". In: *IEEE transactions on magnetics* 42.1 (2005), pp. 15–17.

[166] Sebastien Amet, Luca Bottura, Valeria Granata, Sandrine Le Naour, RK Mishra, L Oberli, David Richter, Stephane Sanfilippo, Arjan Verweij, Louis Walckiers, et al. "Persistent and coupling current effects in the LHC superconducting dipoles". In: *IEEE transactions on applied superconductivity* 13.2 (2003), pp. 1239–1242.

[167] Rainer Meinke. "Superconducting magnet system for HERA". In: *IEEE transactions on magnetics* 27.2 (1991), pp. 1728–1734.

[168] Chuyu Liu, Donald Bruno, Al Marusic, Michiko Minty, Peter Thieberger, and Xiaorong Wang. "Mitigation of persistent current effects in the RHIC superconducting magnets". In: *Physical Review Accelerators and Beams* 22.11 (2019), p. 111003.

[169] L Bottura, L Rossi, L Serio, G de Rijk, V Parma, C Maglioni, Walter Scandale, R MacCaferri, and D Tommasini. *Conceptual design of superferric magnets for PS2*. Tech. rep. 2007.

[170] I Shilon, A Dudarev, H Silva, and HHJ Ten Kate. "Conceptual design of a new large superconducting toroid for IAXO, the new International AXion Observatory". In: *IEEE transactions on applied superconductivity* 23.3 (2013), pp. 4500604–4500604.

[171] Dan Green. *At the leading edge: the ATLAS and CMS LHC experiments*. World Scientific, 2010.

[172] Pasquale Arpaia, Annalisa Liccardo, Marco Buzio, and Alessandro Parrella. "On the use of fluxmetric methods for characterizing feebly magnetic materials". In: *2017 IEEE International Instrumentation and Measurement Technology Conference (I2MTC)*. IEEE. 2017, pp. 1–6.

[173] Ion Gabriel Ion, Melvin Liebsch, Abele Simona, Dimitrios Loukrezis, Carlo Petrone, Stephan Russenschuck, Herbert De Gersem, and Sebastian Schöps. "Local field reconstruction from rotating coil measurements in particle accelerator magnets". In: *Nuclear Instruments and Methods in Physics Research Section A: Accelerators, Spectrometers, Detectors and Associated Equipment* 1011 (2021), p. 165580.

[174] Herbert De Gersem, Armin Galetzka, Ion Gabriel Ion, Dimitrios Loukrezis, and Ulrich Römer. "Magnetic field simulation with data-driven material modeling". In: *IEEE Transactions on Magnetics* 56.8 (2020), pp. 1–6.

[175] Armin Galetzka, Dimitrios Loukrezis, and Herbert De Gersem. "Data-driven solvers for strongly nonlinear material response". In: *International Journal for Numerical Methods in Engineering* 122.6 (2021), pp. 1538–1562.

[176] Stefano Sorti, Carlo Petrone, Stephan Russenschuck, and Francesco Braghin. "Data-driven simulation of transient fields in air-coil magnets for accelerators". In: *Nuclear Instruments and Methods in Physics Research Section A: Accelerators, Spectrometers, Detectors and Associated Equipment* (2021), p. 165571.

[177] Amir Borna, Tony R Carter, Paul DeRego, Conrad D James, and Peter DD Schwindt. "Magnetic Source Imaging Using a Pulsed Optically Pumped Magnetometer Array". In: *IEEE Transactions on Instrumentation and Measurement* 99 (2018), pp. 1–9.

[178] James E Green, David A Stone, Martin P Foster, and Alan Tennant. "Spatially resolved measurements of magnetic fields applied to current distribution problems in batteries". In: *IEEE Transactions on Instrumentation and Measurement* 64.4 (2014), pp. 951–958.

[179] Liming Fan, Xiyuan Kang, Quan Zheng, Xiaojun Zhang, Xuejun Liu, Chunlei Chen, and Chong Kang. "A fast linear algorithm for magnetic dipole localization using total magnetic field gradient". In: *IEEE Sensors Journal* 18.3 (2017), pp. 1032–1038.

[180] Daniel Cichon, Rafael Psiuk, Hartmut Brauer, and Hannes Töpfer. "A Hall-Sensor-Based Localization Method With Six Degrees of Freedom Using Unscented Kalman Filter". In: *IEEE Sensors Journal* 19.7 (2019), pp. 2509–2516.

[181] Thomas Schlegl, Markus Neumayer, Stephan Mühlbacher-Karrer, and Hubert Zangl. "A pretouch sensing system for a robot grasper using magnetic and capacitive sensors". In: *IEEE Transactions on Instrumentation and Measurement* 62.5 (2013), pp. 1299–1307.

[182] Ming Yin, Xiaoning Liu, Yu Liu, and Xun Chen. "Medical image fusion with parameter-adaptive pulse coupled neural network in nonsubsampled shearlet transform domain". In: *IEEE Transactions on Instrumentation and Measurement* 99 (2018), pp. 1–16.

[183] Jinlong Dong, Guogang Zhang, Yingsan Geng, and Jianhua Wang. "Current Distribution Reconstruction in Low-Voltage Circuit Breakers Based on Magnetic Inverse Problem Solution Considering Ferromagnetic Splitters". In: *IEEE Transactions on Magnetics* 99 (2018), pp. 1–9.

[184] Ahmed Abou-Elyazied Abdallh and Luc Dupré. "A unified electromagnetic inverse problem algorithm for the identification of the magnetic material characteristics of electromagnetic devices including uncertainty analysis: A review and application". In: *IEEE Transactions on Magnetics* 51.1 (2014), pp. 1–10.

[185] Gerlind Schubert and Philip Harrison. "Magnetic induction measurements and identification of the permeability of Magneto-Rheological Elastomers using finite element simulations". In: *Journal of Magnetism and Magnetic Materials* 404 (2016), pp. 205–214.

[186] Oszkár Birò, C Paul, and K Preis. *The use of a reduced vector potential $A\_\{r\}$ formulation for the calculation of iron induced field errors*. Tech. rep. CERN, 1999.

[187] Kenneth Levenberg. "A method for the solution of certain non-linear problems in least squares". In: *Quarterly of applied mathematics* 2.2 (1944), pp. 164–168.

[188] Donald W Marquardt. "An algorithm for least-squares estimation of non-linear parameters". In: *Journal of the society for Industrial and Applied Mathematics* 11.2 (1963), pp. 431–441.

[189] Metrolab Technology SA. *PT2025 NMR Precision Teslameter specifications*. Nov. 2019. URL: https://www.metrolab.com/products/pt2025/.

[190]   Dragana Popovic Renella, Sasa Spasic, Sasa Dimitrijevic, Marjan Blagojevic, and Radivoje S Popovic. "An overview of commercially available teslameters for applications in modern science and industry". In: *Acta Imeko* 6.1 (2017), pp. 43–49.

[191]   DJ Mapps. "Magnetoresistive sensors". In: *Sensors and Actuators A: Physical* 59.1-3 (1997), pp. 9–19.

[192]   Fritz Primdahl. "The fluxgate magnetometer". In: *Journal of Physics E: Scientific Instruments* 12.4 (1979), p. 241.

[193]   Melvin Liebsch, Stephan Russenschuck, and Stefan Kurz. "Boundary-Element Methods for Field Reconstruction in Accelerator Magnets". In: *IEEE Transactions on Magnetics* 56.3 (2020), pp. 1–4.

[194]   Physik Instrumente. *M-511, M-521, M-531 High-Precision Linear Stage*. Sep. 2020. URL: https://static.physikinstrumente.com/fileadmin/user_upload/physik_instrumente/files/datasheets/M-511-Datasheet.pdf.

[195]   Leica Geosystems. *Leica Absolute Tracker AT930*. Sep. 2020. URL: https://www.hexagonmi.com/products/laser-tracker-systems/leica-absolute-tracker-at930.

[196]   Tektronix Inc. *Keithley 2700, 2701, and 2750 Multimeter*. Sep. 2020. URL: https://www.tek.com/keithley-switching-and-data-acquisition-systems/keithley-2700-multimeter-data-acquisition-switch-sys.

[197]   BIPM, IEC and IFCC, ILAC and ISO, IUPAC, IUPAP, and OIML. *Evaluation of measurement data, Supplement 1 to the GUM: propagation of distributions using a Monte Carlo method*. Tech. rep. Joint Committee for Guides in Metrology, 2008.

[198]   A. Perez Fontenla. *Microscope inspection of stainless steel AISI 316 cylinder surface after Electrical Discharge Machining (EDM)*. Technical Note EDMS 2405262. Geneva, CH: European Organization for Nuclear Research (CERN), 2020. URL: https://edms.cern.ch/document/2405262/0.

[199]   Boris Bellesia, F Bertinelli, C Santoni, and E Todesco. "Dependence of magnetic field quality on collar supplier and dimensions in the main LHC dipole". In: *IEEE transactions on applied superconductivity* 16.2 (2006), pp. 196–199.

[200]   A Siemko. "Magnet quench process". In: *Chamonic XI* (2001).

[201] S Kobayashi, N Hosoda, and R Takashima. "Tungsten alloys as radiation protection materials". In: *Nuclear Instruments and Methods in Physics Research Section A: Accelerators, Spectrometers, Detectors and Associated Equipment* 390.3 (1997), pp. 426–430.

[202] Diana Adlienė, Laurynas Gilys, and Egidijus Griškonis. "Development and characterization of new tungsten and tantalum containing composites for radiation shielding in medicine". In: *Nuclear Instruments and Methods in Physics Research Section B: Beam Interactions with Materials and Atoms* 467 (2020), pp. 21–26.

[203] G De Temmerman, T Hirai, and RA Pitts. "The influence of plasma-surface interaction on the performance of tungsten at the ITER divertor vertical targets". In: *Plasma Physics and Controlled Fusion* 60.4 (2018), p. 044018.

[204] P Borges de Sousa, M Morrone, N Hovenga, C Garion, R van Weelderen, T Koettig, and J Bremer. "Parametric study on the thermal performance of beam screen samples of the High-Luminosity LHC upgrade". In: *IOP Conference Series: Materials Science and Engineering*. Vol. 278. 1. IOP Publishing. 2017, p. 012053.

[205] Marco Morrone, Cedric Garion, Paolo Chiggiato, Oscar Sacristan De Frutos, Michael Guinchard, and Lucio Fiscarelli. "Mechanical Behavior of the shielded HL-LHC Beam Screen during a Magnet Quench". In: *IEEE Transactions on Applied Superconductivity* (2021).

[206] *ASTM B777-15 - Standard Specification for Tungsten Base, High-Density Metal*. Standard ASTM B777-15. American Society for Testing and Materials, 2020.

[207] Cristina Bahamonde Castro, Francesco Cerutti, Paolo Fessia, Anton Lechner, Alessio Mereghetti, Daniele Mirarchi, Stefano Redaelli, and Eleftherios Skordis. "Improved Protection of the Warm Magnets of the LHC Betatron Cleaning Insertion". In: *8th Int. Particle Accelerator Conf.(IPAC'17), Copenhagen, Denmark, May 14-19, 2017*. JACOW, Geneva, Switzerland. 2017, pp. 72–75.

[208] Eleftherios Skordis. "Radiation impact of collimation beam losses in the LHC and HL-LHC". PhD thesis. The University of Liverpool (United Kingdom), 2019.

[209] Niklas Templeton, Alessandro Ratti, Shrikant Pattalwar, Andrew May, Thomas Jones, Ofelia Capatina, Teddy Capelli, Carlo Zanoni, Federico Carra, Graeme Burt, et al. "Design of the thermal and magnetic shielding for the LHC High Luminosity Crab-Cavity upgrade". In: *17th Int. Conf. on RF Superconductivity (SRF'15), Vancouver BC, Canada, September 13-18, 2015*. 2015.

[210] Rama Calaga, Ofelia Capatina, Giovanna Vandoni, et al. "The SPS tests of the HL-LHC crab cavities". In: *9th Int. Particle Accelerator Conf.(IPAC'18), Vancouver BC, Canada, Apr 29 - May 4, 2018*. 2018, pp. 846–849.

[211] Carlo Zanoni, K Artoos, S Atieh, I Aviles-Santillana, S Belomestnykh, I Ben-Zvi, JP Brachet, G Burt, R Calaga, O Captina, et al. "Design of dressed crab cavities for the HL-LHC upgrade". In: *17th Int. Conf. on RF Superconductivity (SRF'15), Vancouver BC, Canada, September 13-18, 2015*. 2015.

[212] Yi-Peng Sun, Ralph Assmann, Javier Barranco, Rogelio Tomás, Thomas Weiler, Frank Zimmermann, Rama Calaga, Akio Morita, et al. "Beam dynamics aspects of crab cavities in the CERN Large Hadron Collider". In: *Physical Review Special Topics-Accelerators and Beams* 12.10 (2009), p. 101002.

[213] Sotirios Papadopoulos, Luca Dassa, JP Dequaire, Frank Gerigk, Francois Pillon, Suitbert Ramberger, Pinar Yilmazer, et al. "Sub-micro-Tesla Magnetic Shielding Design for Cryomodules in the High-gradient Program at CERN". In: *18th Int. Conf. on RF Superconductivity (SRF'17), Lanzhou, China, July 17-21, 2017*. JACOW, Geneva, Switzerland. 2018, pp. 278–282.

[214] Marco Garlasché, Kurt Artoos, Rama Calaga, Ofelia Capatina, Teddy Capelli, D Lombard, P Minginette, M Narduzzi, J Swieszek, PF Marcillac, et al. "Assembly of the DQW Crab Cavity Cryomodule for SPS test". In: *9th Int. Particle Accelerator Conf.(IPAC'18), Vancouver BC, Canada, Apr 29 - May 4, 2018*. 2018.

[215] John F Schenck. "The role of magnetic susceptibility in magnetic resonance imaging: MRI magnetic compatibility of the first and second kinds". In: *Medical physics* 23.6 (1996), pp. 815–850.